

NASA Contractor Report 4581

Numerical Simulation of the Edge Tone Phenomenon

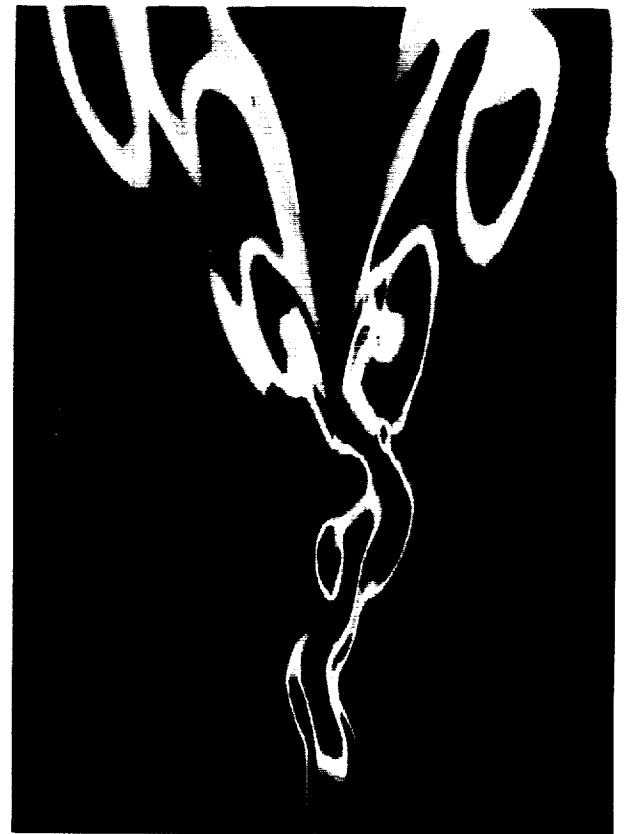
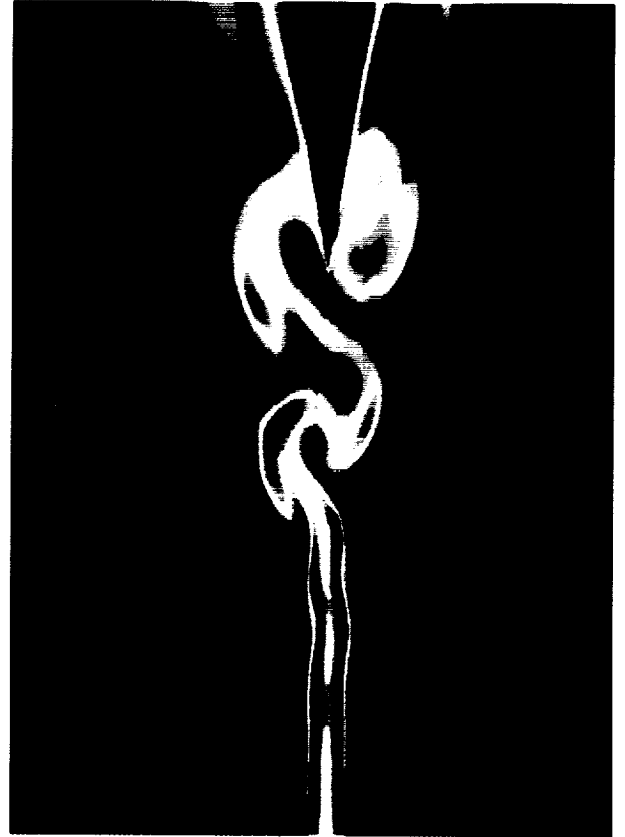
N.S. Dougherty, B.L. Liu, and J.M. O'Farrell
Rockwell International
Huntsville, Alabama

Prepared for
George C. Marshall Space Flight Center
under Contract NAS8-38550



National Aeronautics and
Space Administration
Office of Management
Scientific and Technical
Information Program

1994



CFD Simulations of Brown's Four Distinct Edge Topologies

Table of Contents

| | |
|---|-----|
| Foreword | i |
| Abstract | ii |
| Table of Contents | iii |
| 1.0 Introduction | 1 |
| Acoustic Sources | 1 |
| Acoustic Resonators | 2 |
| Class I Whistles | 2 |
| Class II Whistles | 2 |
| Class III Whistles | 3 |
| G.B. Brown's Edge Tone Experiment | 3 |
| 2.0 Edge Tones Studies in the Literature | 6 |
| 3.0 Methodology | 9 |
| The Unified Solutions Algorithm (USA) Computer Code | 9 |
| Boundary Conditions | 10 |
| Flow Conditions | 12 |
| Grid Systems | 13 |
| 4.0 Results | 15 |
| Pre-Edge Tone (0.30cm) | 16 |
| Stage I Edge Tone (0.33 cm) | 21 |
| Stage I Edge Tone (0.40 cm) | 27 |
| Stage II Edge Tone (0.56 cm) | 32 |
| Stage III Edge Tone (0.82 cm, Vibrating) | 37 |
| Stage III Edge Tone (0.86 cm, Stationary) | 41 |
| Stage IV Edge Tone (1.60 cm) | 46 |
| Post-Edge Tone (4.0 cm) | 51 |
| 5.0 Discussion and Interpretation of Results | 55 |
| Pressure Differential at the Wedge Apex | 55 |
| Pressure Differential at the Orifice | 56 |
| Amplitude Decrease from the Wedge Apex | 57 |
| Pressure Differential Between the Wedge Tip and the Orifice | 58 |
| Formation, Growth, Transport and Dissipation of Vortices | 59 |
| Vortex Shedding Flow Patterns | 60 |
| Farfield Acoustic Wave Patterns | 62 |
| Farfield Sound Pressure Levels | 63 |
| Density Pulsations in the Channel to the Orifice | 63 |
| Appendix A - Acoustic Point Sources | 64 |
| Monopoles | 64 |
| Dipoles | 64 |
| References | 65 |



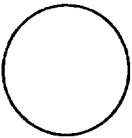
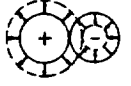
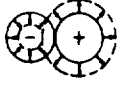

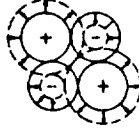
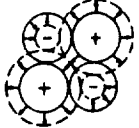
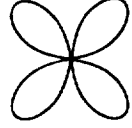
1. Introduction

In the following, "pressure waves" traveling in a medium at the speed of sound, $a_s = \text{Mach } 1.0$, will be referred to as acoustic impulses. The definition of sound generally covers acoustic phenomena in air in the range of 30 to 15,000 Hertz. Wave-like periodicity of sound is a function of periodically generated acoustic impulses or a feedback system operating on acoustic impulses. Although the periodic impulse generation and feedback system are part of sound production, it is a separate process from the production of the acoustic impulse and is treated separately. The basic element of sound is an impulse. Periodic acoustic impulse production and/or amplification is known as sound. The production of the acoustic impulse is a microscopic phenomenon, treated by statistical quantum mechanics, while the production of sound is a macroscopic system phenomenon addressed by control theory.

Most aerodynamic sound producing systems are composed of two closely integrated interacting systems: the primary resonant system and the aerodynamic generator which excites the primary resonator. The primary resonant system usually consists of a fluid confined by rigid boundaries having one or more openings. The aerodynamic acoustic generator, or acoustic source, is the system element which delivers the driving force for the resonator. Sound waves are generated by the transfer of mechanical or thermal vibrational energy from a source to the fluid. The source may also be the fluid motion itself as in the generation of sound from the turbulent motion of a jet.

Acoustic Sources

Acoustic sources may be categorized as monopole, dipole, quadrupole or higher multipole sources. These sources are considered as forcing mechanisms for a fluid in periodic motion. Simple monopole sources resemble a sphere with an expanding and contracting radius. The simple monopole source model requires forcing a volume of fluid away from the source in all directions and then back again. Two monopoles acting in concert, with one acting in the opposite sense as the other, maintain a relationship that is referred to as a dipole source. The dipole is represented using a model in which a volume of fluid is forced back and forth along an axis. More complex point sources are composed of assemblages of dipoles. These sources represent opposed motions of a volume of fluid along several axes, as shown in Figure 1-1 from Beranek².

| Source type | Radiation characteristic | | Directivity pattern | Radiated power is proportional to |
|-------------|---|---|---|-----------------------------------|
| | 180° phase difference | | | |
| Monopole |  |  |  | $\rho L^2 \frac{U^4}{a}$ |
| Dipole |  |  |  | $\rho L^2 \frac{U^6}{a^3}$ |
| Quadrupole |  |  |  | $\rho L^2 \frac{U^8}{a^5}$ |

where

ρ = Density

L = Length

U = Jet Velocity

a = Speed of Sound

Figure 1-1 Aerodynamic Acoustic Sources

A jet impinging on a wedge is a dipole acoustic generator, since flow impingement is forced alternately on each side of the wedge. Fluid compression, resulting from the pressure/density buildup at the site of the flow impingement, represents the movement of fluid onto a particular side of an axis in the dipole model. Details of sound pressure calculations for monopole and dipole sources may be found in Appendix A.

Acoustic Resonators

The resonant system matching the edge tone generation is classified as an aerodynamic whistle. Aerodynamic whistles are fluid oscillators which are self-sustained by feedback processes generated by instability in the fluid flow. The frequency of these oscillations is governed by the periodicity of the feedback cycle. R. Chanaud³, in an article written for Scientific American magazine, categorized aerodynamic whistles into three classes. Class I whistles are those whose feedback consists primarily of hydrodynamic oscillations. Examples of these whistles are the aeolian tone generators, such as aeolian harps, telephone wires, and circular cylinders in a flow. Sound from these particular whistles is generated from the instability created by vortices formed and released into a flow. Class II whistles exhibit feedback from acoustic waves generated by the whistle and fed directly back to the region of instability. Examples of this type of whistle are the edge tone, hole tone, and ring tone, where sound is generated from flow interaction with an edge and fed back upstream destabilizing the jet. Class III whistles have acoustic feedback which is reflected back to the region of instability by some ancillary structure. These whistles generate sound by resonance effects from a structure. The organ pipe tones are the best known examples of this phenomena.

Class I Whistles

Aeolian tone generators are essentially long thin objects in a fluid flow. At certain velocities, unsteady fluid flow around the object creates a pattern of alternate vortex shedding from opposing sides of the object, with each vortex influencing the formation and growth of the succeeding vortex. The vortices formed in this manner develop a wake flow pattern downstream of the object known as the Karman Vortex Street. The oscillations produced in the wake by these vortices generate a sound pressure field with a maximum amplitude at right angles to the vortex street. The frequencies developed by the aeolian tone generators are directly related to the speed of the fluid and the characteristic length, usually the diameter, of the object. The relationship between object characteristic length, L , fluid velocity, U , and frequency, f , may be described for this class of whistle by a constant known as the Strouhal number, S .

$$S = \frac{fL}{U}$$

The experimentally gathered acoustic data for flow past particular geometric structures provides an accurate assessment of the Strouhal number of these flow/structural interaction acoustic systems over a wide range of flow regimes. This accumulated data coupled with the above relationship makes the Class I whistles useful for practical applications such as flow meters.

Class II Whistles

Observed by Sondhaus⁴ in 1854, the edge tone is one of the basic high frequency whistle phenomena which today still challenges both theoretical and experimental fluid dynamicists for a full understanding. However, many attributes related to the nature of the edge tone have been analyzed and much more is presently known concerning these phenomena. The typical edge tone configuration is a jet issuing from a slit and impinging against a sharp edge, as shown in Figure 1-2, the jet velocity, U , the orifice width, d , the distance from the orifice to the wedge, h , and the wedge angle, α , are the defining parameters of this system. At the jet orifice, a shear layer defining the jet is developed. From the instability of this shear layer at the corners of the jet orifice, vortices are generated and released to be convected downstream. With certain edge tone configurations, depending on the flow velocity and wedge distance from the orifice, the developed jet instability causes alternate vortex shedding at the corners of the jet orifice. Vortex

formation may also develop in the shear layer of the jet away from the orifice at higher frequency stages. Downstream, the alternating impingement of the vortices on the wedge creates a flow/structural system acting as an acoustic dipole. This acoustic energy propagates back upstream to organize and enhance flow instability at the jet orifice, further strengthening the alternate vortex shedding pattern developing at the orifice. As the vortex shedding frequency matches phase with the acoustic frequency of the wedge dipole, an audible edge tone develops. This vortex-acoustic interaction is the basic mechanism of the edge tone phenomenon. The closed-loop feedback cycle of regular vortex shedding and jet disturbances generated by acoustic feedback controls the edge tone phenomenon. These jet flow oscillations occur at predictable frequencies for a particular range of jet velocities and edge distances from the jet orifice. The frequency is limited by the acoustic and vortex transport (convection) times and the process of vortex formation. Curiously, it has also been shown in experiments that the simplest of interference (i.e., an object placed in the jet or a second wedge moved into proximity of and transverse to the jet) can cause tone cessation. Interference and disruption of the in-phase vortex-acoustic interaction can very effectively eliminate edge tones. The sound pressure field exerted on the fluid medium exhibits a maximum in the vicinity of the wedge tip indicating the source or generator of the acoustic field, to be located at the wedge apex.

Class III Whistles

Class III whistles require a resonant or reflecting structure to perpetuate the acoustic feedback. The frequency of the tone is governed principally by the resonant modes of the reflecting geometry and not the speed of the flow. The flow speed can be varied over a wide range without affecting the pitch of the whistle. When the speed of the flow increases to a point where the first resonance of the reflecting structure is no longer amplifying the oscillations, the frequency jumps from the first frequency stage to a second stage.

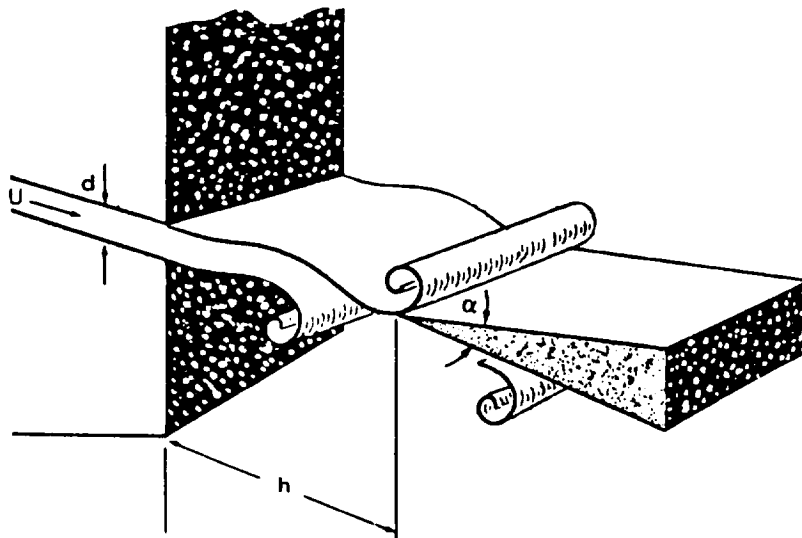


Figure 1-2 Edgetone Configuration of a Jet Impinging on a Wedge

G. B. Brown's Edge Tone Experiment

For simplicity, this classical fluid dynamic problem was selected for demonstration of analytical simulation of acoustic mechanisms by solving the Navier-Stokes equations in low speed flows. The experiment had easily reproducible boundary conditions and was well documented. The apparatus, Figure 1-3, consisted mainly of a wooden box into which air mixed with cigarette smoke was pumped. The horizontal top face of the box had a brass slit of width 1.0 mm, depth of 10.0 mm, and length of 23.0 mm. Air was allowed to exit through this slit and impinge on a brass wedge of angle 20.0 degrees and width 50.0 mm, and having height 75.0 mm. Acoustic dampers were placed around the box and the experimental area. For a particular wedge-to-orifice distance,

the velocity of the air exiting the slit was adjusted to a given value and allowed to come to a steady state. Measurements of frequency were made with a stroboscopic counter.

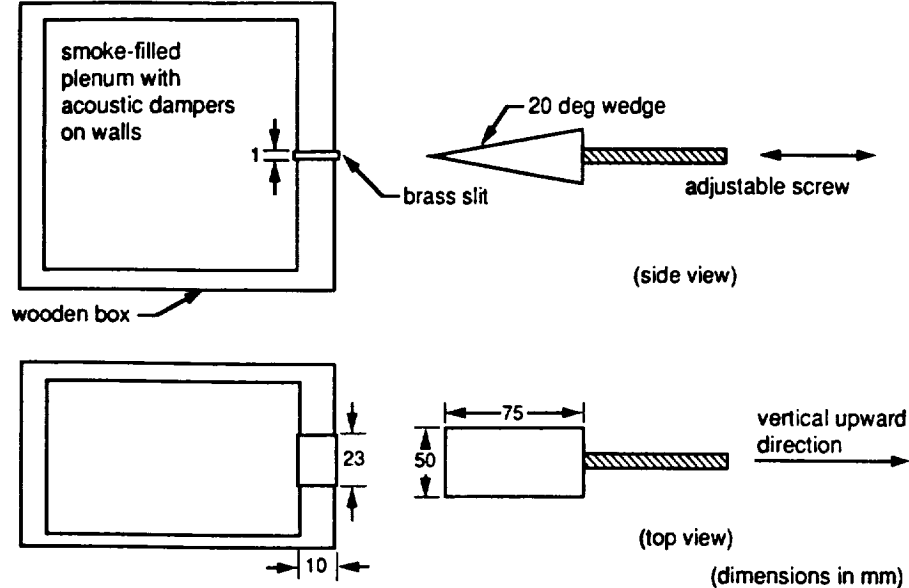


Figure 1-3 Experimental Set-up of G.B. Brown's Edge Tone Experiment

When the wedge was close to the orifice, no tone was detected. At a particular point, as the distance between the wedge and orifice increased, a "clear bright" tone was established, referred to by Brown as Stage I. The frequency then decreased as the distance increased until a jump to a higher frequency, Stage II, occurred. These jumps in frequency, distinct stages, occurred for four particular wedge-to-orifice distances, before the tone became confused and irregular at large wedge distances. Brown¹ experimentally demonstrated four stable edge tone stages for each velocity. An edge tone onset distance and a distance where the edge tone phenomenon had disappeared were also determined. Results for this experiment with a jet velocity of 1750 cm/sec are illustrated in Figure 1-4. The dependence of the frequency, f , on the distance of the wedge to the orifice, h , and the mean velocity, U , was represented for the 1.0 mm slit width by the formula:

$$f = 0.466k (U - 40.0) \left(\frac{1}{h} - 0.07 \right)$$

where $k = 1, 2.3, 3.8,$ and 5.4 for the four stages respectively.

Important flow features for a numerical simulation to establish, in order to validate computations of acoustic phenomena in low speed flows[†], were clearly defined in the experiment by Brown. Brown's results include the edge tone frequencies for specific wedge-to-orifice distances, hysteresis effects and tonal jumps at specific wedge-to-orifice distances, and the interaction between acoustic and vortex transport phenomena associated with obtained frequencies, all of which were reported and discussed in the paper of Brown¹. The frequency results which were to be replicated are summarized in Figure 1-4.

[†] Rockwell's Unified Solutions Algorithm (USA) Computational Fluid Dynamics (CFD) code was selected for this numerical simulation.

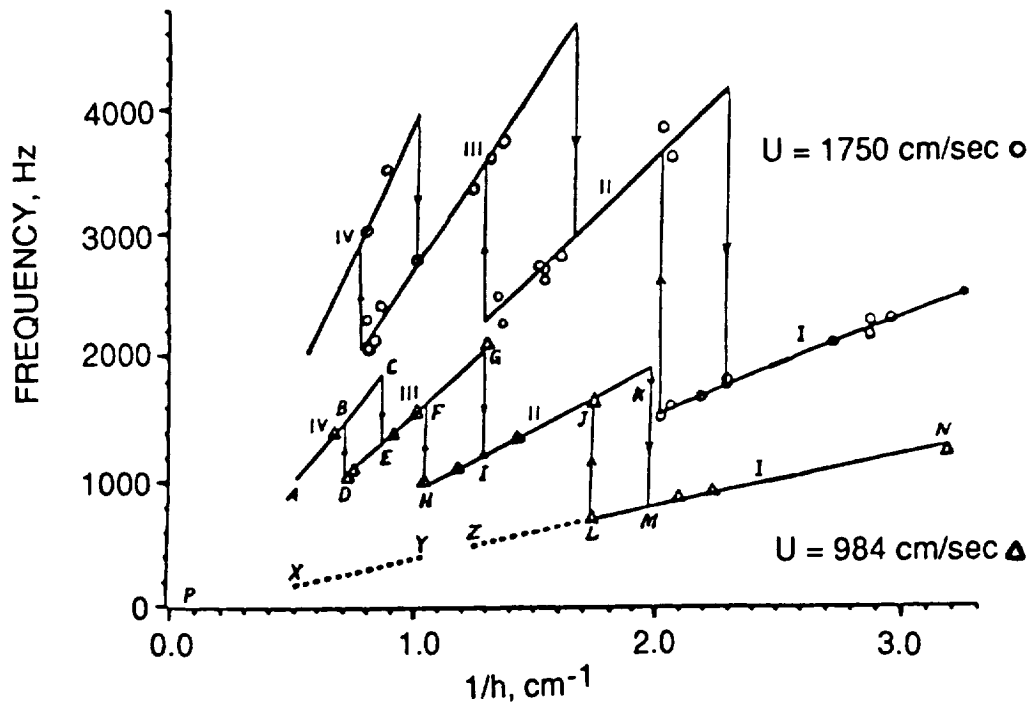


Figure 1-4 Measured Frequency vs. Inverse Distance Results from G.B. Brown's Experiment

2.0 Edge Tone Studies in the Literature

Several computational investigations have been accomplished using either potential or incompressible flow analyses. Few compressible full Navier-Stokes flow computations are found in the literature addressing edge tones.

Early experimenters proposed several theories and empirical formulas for edge tones. Curle⁵, Nyborg⁶, and Powell⁷ found that the propagation and growth of jet disturbances play an important role in the generation of edge tones. Experiments of Brown^{1,8}, Karamcheti and Bauer⁹, and Shield and Karamcheti¹⁰ led to additional empirical formulas for establishing connections between flow and acoustic effects. Brown indicated that when the jet velocity was high (greater than 600 cm/sec), Stage I often occurred simultaneously with other stages. An important aspect of the present study was to check the numerical simulation for simultaneous occurrence of edge tone stages.

Due to complicated apparatus-dependent vortex-acoustic interactions, various published experimental results do not universally agree. Some nozzles (or orifices) had acute lips while others did not. Some jet-wedge systems had little far-field feedback while others apparently had additional acoustic interference due to the supporting casing and other devices. Due to the shape and dimensions of the orifice, the pressure drop and velocity profiles may not have been the same, even under the same flow rates. Consequently, different flow conditions have yielded different frequency responses.

Large vortices play a controlling role in the instability of the edge tone flow field. In the case of a single bluff body containing a slit, its surface is considered to be the vortex-producing surface. A downstream surface, in this case the wedge, is denoted as a vortex-interaction surface. Acoustic interactions among these two surfaces and vortices in the jet flow field are inevitable at certain flow conditions. In the case of edge tones, the vortex-acoustic interaction is found to be the basic flow phenomenon as the closed-loop feedback cycle of regular vortex shedding and acoustic feedback takes over and controls the edge tone production process at a frequency dependent upon the experimental set-up geometry and jet flow velocity.

The primary insight into vortex production at the orifice noted by Curle⁵ was "the reciprocal influence of the maximum transverse velocity in the jet upon the shedding of vortices at the edge, and the sudden production of free vorticity at the edge in deflecting the jet, causes a slight extra production of vorticity on one side of the slit, which is in turn amplified as it moves downstream." Powell⁷ observed that the local maximum amplitude for edge tones would decrease with increasing wedge distance.

Stegen and Karamcheti¹¹ found that the rate of amplitude growth decreased proportionally to increasing wedge distance, while the local maximum amplitude remained essentially the same. They included a smoke flow photograph of a 20.0 degree wedge placed against a jet. In this photograph, alternate vortices are observed on the slopes of the wedge. The photograph also indicates that at distances greater than five times the wedge distance, the flow velocity field disturbances are considerably weakened. Disturbance propagation was discussed by Stegen and Karamcheti. They noted that the speed of the disturbance is a function of distance from the orifice (or nozzle), and the wavelength (distance between consecutive vortices) varies spatially to maintain the same tone frequency. Shield and Karamcheti¹⁰ experimentally investigated an edge tone flowfield using hot-wire anemometry. The variation of the phase and amplitude of the transverse velocity was measured along the centerline of the edge tone system. These measurements were made at several wedge distances during both Stage I and Stage II operation for a fixed orifice width Reynolds number of 6350. The spatial variation of the amplitude was found to depend on the distance parameter from the nozzle exit, (x/h), and on the stage of operation. The edge tone amplitude grew with distance in Stage I operation. A leveling of the amplitude, corresponding to the frequency of the transverse jet velocity, was found characteristic of the higher frequency oscillations in Stage II.

Many investigators have presented empirical formulas for pressure oscillation frequency and amplitude. The far-field radiation properties of the edge tone were aptly simulated by an acoustic dipole by Lighthill¹². According to his theory, the net force, $|P|$, exerted on a fluid by a body (which is small compared with the wavelength of the sound being generated), is related to the far-field pressure of a point dipole. This result is formulated as:

$$|P| = \frac{fF_0}{2ra} \cos\theta$$

- where $|P|$ = 0-to-peak acoustic pressure amplitude,
 f = edge tone frequency,
 F_0 = 0-to-peak amplitude of the fluctuating force of the jet impinging on the wedge
 θ = angle from the direction of the force exerted on the fluid,
 r = distance from the center of the edge, and
 a = speed of sound.

Figure 2-1 illustrates Lighthill's formulation. Note that the actual value of the sound wave amplitude, $|P|$, cannot be determined before the magnitude of the force on the edge is found. Compare this with the formula for the dipole pressure expression found in Appendix A.

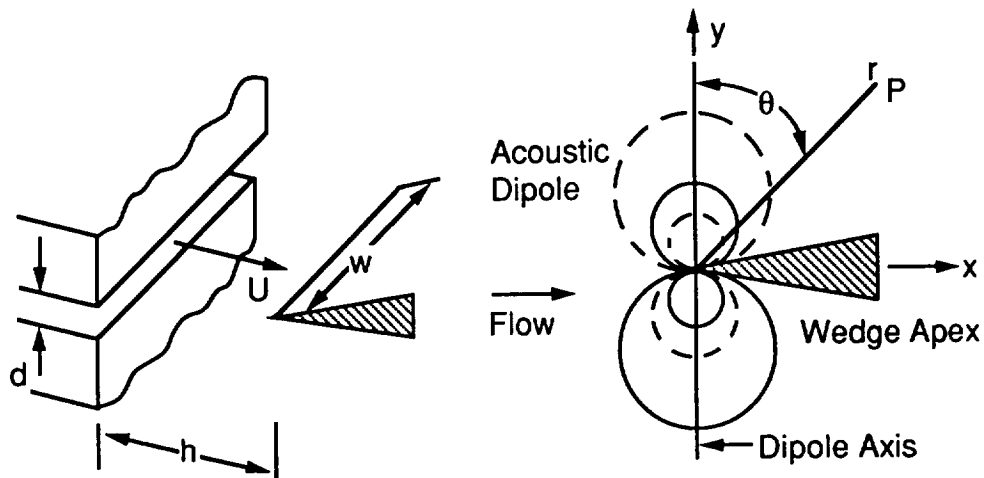


Figure 2-1 Farfield Radiation Pressure Calculation Parameters for a Dipole

For maximum intensity, ($\theta = 0$), flat-plate edge with an asymmetric vortex street propagating downstream and fixed jet velocity and wavelength, Holger et. al.^{13,14} developed the following potential flow model. Their edge tone amplitude formula was given as:

$$|P| = 0.0478 \left[(n + A_n) \left(\frac{d}{h} \right) \right]^{1.5} \left(\frac{F_{0,0} W_p U^3}{ra} \right)$$

where A_n is a stage constant with values,

- A_n = 0.40 if $n = 1$,
= 0.35 if $n = 2$, and
 U = initial jet speed,
 h = wedge distance,
 d = orifice thickness,
 r = distance from the center of the edge,

$$F_{0,0} = \text{non-dimensional } F_0 = \frac{F_0}{0.104\rho U^2 W d}$$

ρ = fluid density, and
 W = wedge width.

When using 10.4 as the value for the non-dimensional force amplitude $F_{0,0}$, Holger's equation agrees with Powell's data⁸ for Stages I and II. Plotting the quantity $\rho(h/d)^{1.5}$ as a function of U , reduces Powell's data to a single plot for each stage. The non dimensional values of h/d ranged from 2.5 to 10.0.

D. Rockwell et. al.^{15,16,17} presented analyses and flow visualization data to show the mechanics of vortex-corner and vortex-wedge interaction using the hydrogen bubble technique and dye injection. Instantaneous traces of resultant variations in transverse location of the incident vortices (with respect to the corner) were shown to produce modulated pressure signals. Low-frequency, self-modulated patterns were also investigated by Rockwell and Knisely¹⁸ using correlations between pressure and the upstream velocity field.

Ohring^{19,20} performed calculations to verify the dipole nature of the edge tone using potential, incompressible flow methods. The wedge was abruptly removed from an earlier computed, multi-frequency edge tone flow, having a Reynolds number of 450, and replaced by an oscillating dipole. The computed flow field strongly resembled the flow field with the wedge present. The moduli of the computed sound pressure components corresponding to various frequencies yielded a "figure eight" pattern in the far-field, with the largest component or tone associated with the frequency of jet impingement. The maximum sound radiated for all components decreased linearly with increasing distance from the body.

Additionally, Brown^{21,22} presented excellent discussions on edge tones and related sound-producing instruments such as organ pipes and whistles. Here Brown discussed the operation of organ pipes in which the resonator eventually controls the frequency of the instrument and reviewed a variety of edge tone theories, further asserting mechanisms for the edge tone phenomenon in sound producing instruments.

Staubli and Rockwell²³ performed flow visualization and pressure measurements for both stationary and vibrating wedges and found that the upstream influence initially distorted the jet at the nozzle exit and caused non homogeneous phase variations along the stream wise extent of the jet. A superposition model which included upstream-induced, unstable wave velocities was found to effectively simulate these distortions.

This constitutes the state-of-the-art in edge tone understanding available in the literature as of 1987.

3.0 Methodology

The present study is an application of the USA code, developed by Chakravarthy et. al.²⁴ at the Rockwell Science Center, to verify the code's ability to accurately predict the acoustic phenomena observed in Brown's experimental data. The primary regions of interest in an edge tone configuration are the vicinity of the orifice and the wedge tip. Since there is no reflection or other significant sound sources, it is assumed that the far-field influence is negligible. The characteristic distances are the orifice-wedge spacing or wedge distance, h , and the orifice (or slit) thickness, d . The wedge angle, α , is another significant parameter. The slit width and depth are of secondary importance provided they are much greater than the orifice thickness. Under these conditions, three-dimensional effects are negligible and nearly fully-developed flow conditions are reached at the exit of the orifice. The key flow parameters are the mean jet speed, U , and the distance from the orifice to the wedge tip, h . The corners of the orifice considered in the present study are rectangular. In other studies from the literature, orifice lips had more acute angles^{19, 23}. Such geometries yield flow fields and frequency results which differ from the 90-degree lip results presented here.

The Unified Solutions Algorithm (USA) Computer Code

The CFD code used in the present study is a multi-zone compressible full Navier-Stokes flow solver. It employs a finite-volume, upwind-biased, total variation diminishing (TVD) numerical scheme. The TVD discretization eliminates spurious numerical oscillations without introducing additional numerical dissipation. The USA code options used in the present study are perfect gas (air), laminar flow, implicit approximate factorization, and full block tridiagonal matrix inversion, with first-order time and third-order spatial accuracy. The numerical simulations using this code were performed on NASA/MSFC's Cray X/MP computer.

The governing equations for the present study are the time-dependent two-dimensional compressible flow Navier-Stokes equations:

$$Q_t + (F - F_v)_x + (G - G_v)_y = 0$$

where Q is a vector of conserved variables, F and G are the inviscid fluxes and F_v and G_v are the viscous vectors :

$$Q = \begin{bmatrix} E_t \\ \rho \\ \rho u \\ \rho v \end{bmatrix}, \quad F = \begin{bmatrix} (E_t + p)u \\ \rho u \\ \rho u^2 + p \\ \rho uv \end{bmatrix}, \quad G = \begin{bmatrix} (E_t + p)v \\ \rho v \\ \rho uv \\ \rho v^2 + p \end{bmatrix},$$

$$F_v = \begin{bmatrix} u\tau_{xx} + v\tau_{xy} - q_x \\ 0 \\ \tau_{xx} \\ \tau_{xy} \end{bmatrix}, \quad \text{and} \quad G_v = \begin{bmatrix} v\tau_{yy} + u\tau_{xy} - q_y \\ 0 \\ \tau_{xy} \\ \tau_{yy} \end{bmatrix}.$$

Here these variables have been nondimensionalized with respect to reference quantities where the prime (') indicates actual physical units:

$$x = \frac{x'}{L_{ref}}, \quad y = \frac{y'}{L_{ref}}, \quad \rho = \frac{\rho'}{\rho_{ref}}, \quad u = \frac{u'}{u_{ref}}, \quad v = \frac{v'}{u_{ref}}, \quad t = \frac{t'}{\left(\frac{L_{ref}}{u_{ref}}\right)},$$

$$T = \frac{T'}{T_{ref}}, \quad \mu = \frac{\mu'}{\mu_{ref}}, \quad \text{and} \quad p = \frac{p'}{\rho_{ref} u_{ref}^2}$$

and L_{ref} = length per grid unit, $u_{ref} = \frac{a_{ref}}{\sqrt{\gamma}}$, and a_{ref} = reference speed of sound. The velocity component 'u' is in the axial direction and 'v' is in the direction transverse to the wedge. The equation of state for an ideal gas in the non-dimensional form is given by:

$$p = \rho T$$

and the total energy, E_t , is the sum of internal energy and kinetic energy:

$$E_t = \frac{p}{\gamma - 1} + \frac{\rho}{2} (u^2 + v^2)$$

The viscous stresses and heat fluxes are given in tensor form by:

$$\tau_{xx} = \frac{2\mu(2u_x - v_y)}{3Re_{ref}}, \quad \tau_{xy} = \frac{\mu(u_y + v_x)}{Re_{ref}}, \quad \tau_{yx} = \frac{2\mu(2u_y - v_x)}{3Re_{ref}},$$

$$q_x = \frac{-k_{ref} T_{ref} k T_x}{\mu_{ref} u_{ref}^2 Re_{ref}}, \quad \text{and} \quad q_y = \frac{-k_{ref} T_{ref} k T_y}{\mu_{ref} u_{ref}^2 Re_{ref}}$$

where the reference Reynolds number, Re_{ref} , is defined as: $Re_{ref} = \frac{\rho_{ref} u_{ref} L_{ref}}{\mu_{ref}}$, μ is dynamic viscosity, k is thermal conductivity, τ is shear stress, and q is heat flux.

Further details, including the TVD formulations, as used in the USA code are outlined in the paper by Chakravarthy²⁴.

Boundary Conditions

The Reynolds number for laminar-turbulent transition based on orifice thickness is 1083 for $U = 1750$ cm/sec, which is less than half the critical Reynolds number for all wedge distances h up to 4.0. This implies that only laminar flow should be considered in this study.

Four flow variables -total energy, density, u-velocity, and v-velocity, (E_t , ρ , u , and v respectively)- are calculated during each numerical iteration. An inflow boundary condition requires fixing three variables, and an outflow boundary condition requires fixing two variables. A subsonic inflow condition is assumed at the orifice inlet, and no-slip conditions are used on wall surfaces.

In a subsonic boundary condition, one may fix either pressure or density. The selection of which variable to fix for these conditions can yield slightly different convergence. It was found for this series of simulations that a fixed pressure condition gave faster convergence. The equation for pressure, p , in terms of total energy, density, and velocity components for perfect gas is given by:

$$p = (\gamma - 1) \left[E_t - \frac{\rho}{2} (u^2 + v^2) \right]$$

where $\gamma = 1.4$, is the specific heat ratio for air. At far-field boundaries, outflow conditions are used if the flow direction is out of the grid, and inflow conditions are used if the flow direction is into the grid.

Flow Conditions

Eight edge tone cases were simulated by varying the distance from the slit to the edge in order to induce different frequency stages. According to Brown's experiments¹, when the distance from the wedge to the slit is less than 0.30 cm, there is inadequate room for the jet to bend, the flow splits more or less evenly on each side of the wedge, and an edge tone does not occur. This type of response is called a pre-edge tone case. In Case 1, the wedge is within this minimal distance to the slit aperture and the production of an edge tone does not occur. Case 2 was run at the 0.33 cm edge tone onset distance. Case 3 was a mid-distance Stage I edge tone simulation. Case 4 was a Stage II simulation. Cases 5 and 6 were Stage III edge tone simulations, where the wedge was induced to vibrate with a one-degree maximum angle of attack, induced according to the expected Stage III frequency. Case 6A is a Stage III edge tone simulation. All cases except Cases 5 and 6 employed a rigid wedge. Case 7 was a Stage IV simulation. Case 8 is a post-edge tone simulation, where the distance to the slit aperture from the wedge is greater than the 2.0 cm maximum distance at which Brown indicated that edge tones were no longer found. A list of edge tone cases simulated in this investigation is given in Table 3-1.

Table 3-1 Simulated Edge Tone Cases

| CASE | STAGE | DISTANCE h, cm | EXPERIMENTAL FREQUENCY (BROWN) |
|------|-------|-------------------|--------------------------------------|
| 1 | PRE- | 0.30 | - |
| 2 | I | 0.33 | 2359 |
| 3 | I | 0.40 | 1936 |
| 4 | I | 0.56 | 1367 |
| | II | 0.56 | 3145 |
| 5* | I* | 0.82 | 916 |
| | II* | 0.82 | 2107 |
| | III* | 0.82 | 3481 |
| 6 | I | 0.86 | 871 |
| | II | 0.86 | 2003 |
| | III | 0.86 | 3309 |
| 7 | I | 1.60 | 442 |
| | II | 1.60 | 1017 |
| | III | 1.60 | 1681 |
| | IV | 1.60 | 2388 |
| 8 | POST- | 4.00 | - |

* WEDGE VIBRATION SIMULATED ALSO

Stage III calculations for a vibrating wedge yielded slightly better frequency agreement with Brown's empirical frequency than the values for a rigid wedge, Case 6A. The wedge vibration was induced in the "v" (transverse) direction corresponding to a one-degree angle of attack variation from an axis running through the wedge apex and the center of the slit aperture. The frequency driving the wedge vibration was set to the expected frequency, derived from Brown's formula, for the 0.82 cm Stage III edge tone.

For each iteration, pressures were monitored at several locations near the wedge and slit aperture, and in the farfield. Additionally, wedge lift (C_L) and drag (C_D) coefficients were calculated from pressures developed on the wedge. Pressures reported are non-dimensional pressure coefficients, (C_p), with $C_p = \frac{p-p_\infty}{.5\rho v^2}$ where p is the local pressure and p_∞ is the pressure in the far field. A Fast Fourier Transform (FFT) analysis on these C_p time histories was used to determine the root-mean-square (rms) spectral characteristics for time-dependent pressure forces. Also calculated were pressure differentials for points on opposite sides of the jet flow near the orifice and on opposite sides of the wedge apex.

Grid Systems

Figure 3-1 shows a typical grid employed in the present computations. Surrounding the wedge, there is an O-grid. As shown in the figure, the grid is clustered near solid surfaces: the orifice-bounding surfaces and the wedge surface. The grid is also highly clustered in the active region of the jet between the orifice and the wedge. The numerical computational domain matches Brown's experimental set-up except for the screw mechanism having been removed. The grid clustering was tailored for each wedge distance case.

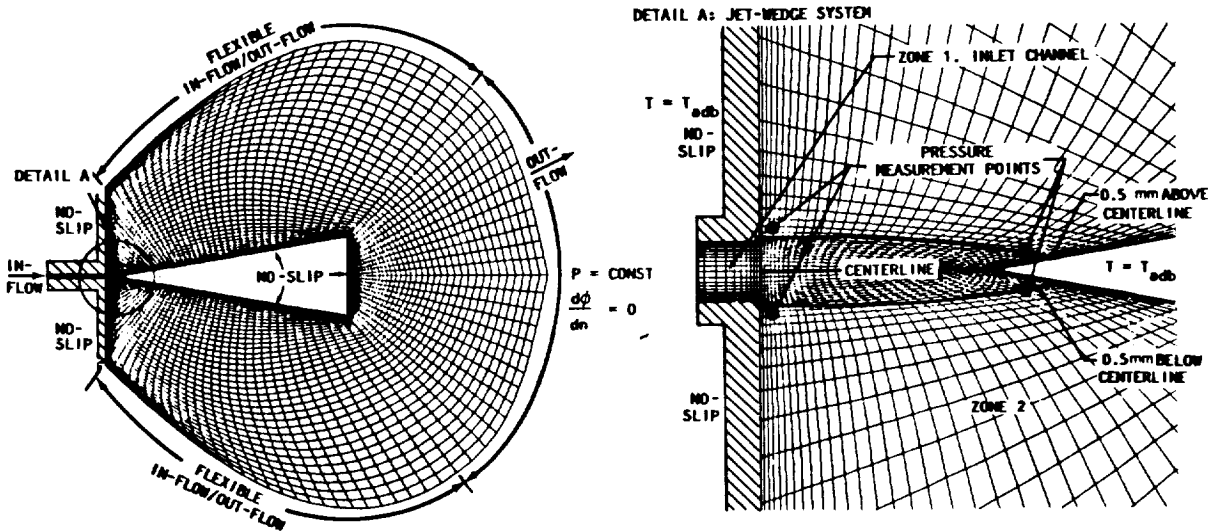


Figure 3-1 Representative Grid System Employed in Edge Tone Simulations

In all first and second stage simulations, the wedge-to-orifice distance is small and the jet curvature is mild; thus, relatively few grid points are necessary. In the third and fourth stage simulations, the wedge-to-orifice distance is more than twice as long and the jet profile is more vigorous; therefore, more grid points are needed. A dense farfield grid system was used in Case 3 to resolve far-field sound pressure levels.

In the present computations, larger computational regions and a full wedge length are used in Cases 2, 4, and 7. Since C_L is based on the wedge length, the length scale factor for these cases

is unity. The length scale factor for Cases 1, 3, and 8 is 0.24, and for Cases 5 and 6 is 0.49. These length scale factors were used to generate the C_{Lrms} data .

Simulation Duration

The duration of each simulation run made on the computer was sufficient to obtain four or five cycles of the lowest edge tone stage frequency present at the particular wedge distance considered. Four or five cycles at the lowest frequency was found to be adequate for FFT analysis. The longest run duration was for the case at $h = 1.6$ cm and was 0.35 seconds. Run duration was a trade-off between amplitude and frequency accuracy versus economy in computer resources. Cases were run only long enough to obtain reasonable accuracy in the FFT estimates and running longer would have yielded only slightly improved accuracy but at greatly increased cost. Plotting frequency as a function of inverse wedge distance shows a linear trend in this analysis somewhat better than the scatter in Brown's frequency measurements.

4.0 Results

For each case listed in Table 3-1, a separate section illustrating results of that particular simulation is provided. In addition to a description of the important flow features observed, each section contains a picture of the grid system employed, density, enthalpy, or pressure contour plots, a velocity directions or streamline plot, and a time history plot with an associated FFT of either C_L or C_p illustrating the frequencies obtained. Figure 4-1 illustrates graphically the excellent agreement of these edge tone simulations with Brown's frequency data. Table 4-1 summarizes the numerical amplitude and frequency results.

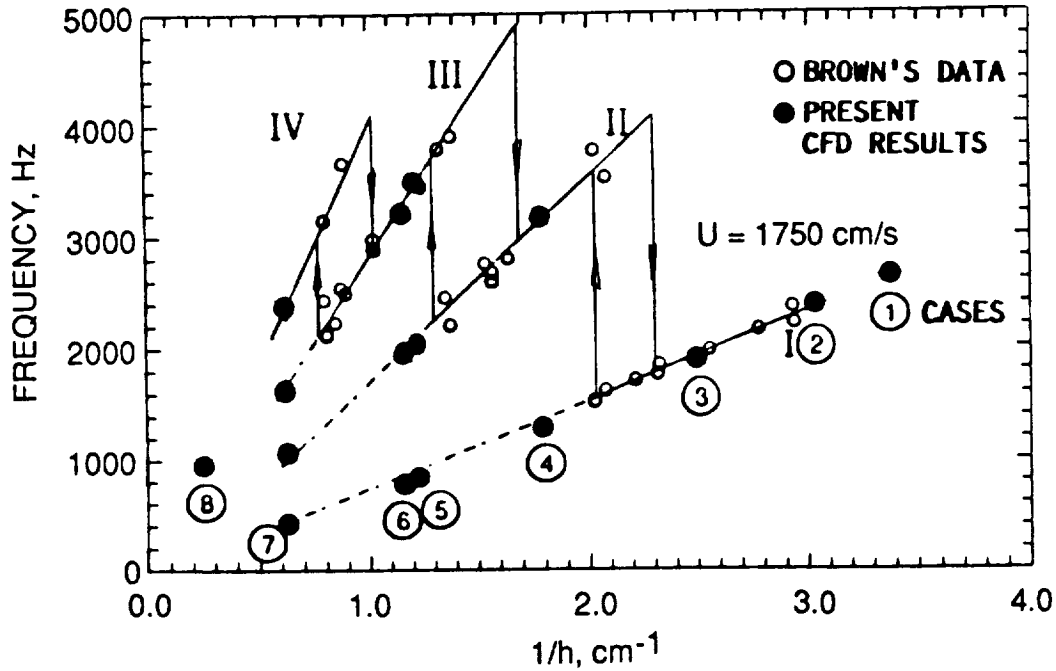


Figure 4-1 Comparison of Present Simulation Frequency Results with Brown's Data

Table 4-1 Summary of Results

| CASE | STAGE | DISTANCE h, cm | C_L | | C_p | | EXPERIMENTAL FREQUENCY (BROWN) |
|------|-------|-------------------|-----------|-----------|-----------|-----------|--------------------------------------|
| | | | FREQUENCY | AMPLITUDE | FREQUENCY | AMPLITUDE | |
| 1 | PRE- | 0.30 | 2533 | 0.003 | - | - | - |
| 2 | I | 0.33 | 2452 | 0.014 | 2370 | 0.0740 | 2359 |
| 3 | I | 0.40 | 1830 | 0.077 | 1902 | 0.6800 | 1936 |
| 4 | I | 0.56 | 1281 | 0.058 | 1299 | 0.0470 | 1367 |
| | II | 0.56 | 3177 | 0.010 | 3261 | 0.0120 | 3145 |
| 5* | I* | 0.82 | 670 | 0.051 | 859 | 0.1700 | 916 |
| | II* | 0.82 | 2007 | 0.045 | 2807 | 0.1430 | 2107 |
| | III* | 0.82 | 3532 | 0.112 | 3491 | 0.1710 | 3481 |
| 6 | I | 0.86 | 610 | 0.010 | 762 | 0.2050 | 871 |
| | II | 0.86 | 2153 | 0.078 | 1957 | 0.0200 | 2003 |
| | III | 0.86 | 3192 | 0.017 | 3220 | 0.2750 | 3309 |
| 7 | I | 1.60 | 430 | 0.011 | 363 | 0.0966 | 442 |
| | II | 1.60 | 1090 | 0.003 | 955 | 0.0761 | 1017 |
| | III | 1.60 | 1664 | 0.012 | 1561 | 0.0457 | 1681 |
| | IV | 1.60 | 2386 | 0.009 | 2188 | 0.0719 | 2388 |
| 8 | POST- | 4.00 | 880 | 0.003 | - | - | - |

* SMALL WEDGE VIBRATION INDUCED AT STAGE III FREQUENCY.

Pre-Edge Tone (0.30 cm)

According to Brown's experiments, when the distance from the wedge to the orifice is less than 3.3 mm, there is inadequate room for the jet to bend and the edge tone does not occur. The pre-edge tone case was run with a wedge distance of 3.0 mm. Only very low amplitude flow oscillations were found in this case. Comparatively, the signals are too weak to be considered an edge tone oscillation.

The grid system employed for the pre-edge tone simulation is illustrated in Figure 4-2. Symmetric flow patterns are found in the density and enthalpy contours, and streamlines as shown in Figures 4-3 through 4-6. The time history and FFT analysis for the lift coefficient is shown in Figures 4-7 and 4-8. There are small fluctuations in the lift coefficient associated with small undulations visible in the jet boundary. The lift signal amplitudes for this case are much smaller than those of the other edge tone studies as shown in Table 4-1. The small value of the lift coefficient indicates that this pre-edge tone case does not produce significant edge tone sound.

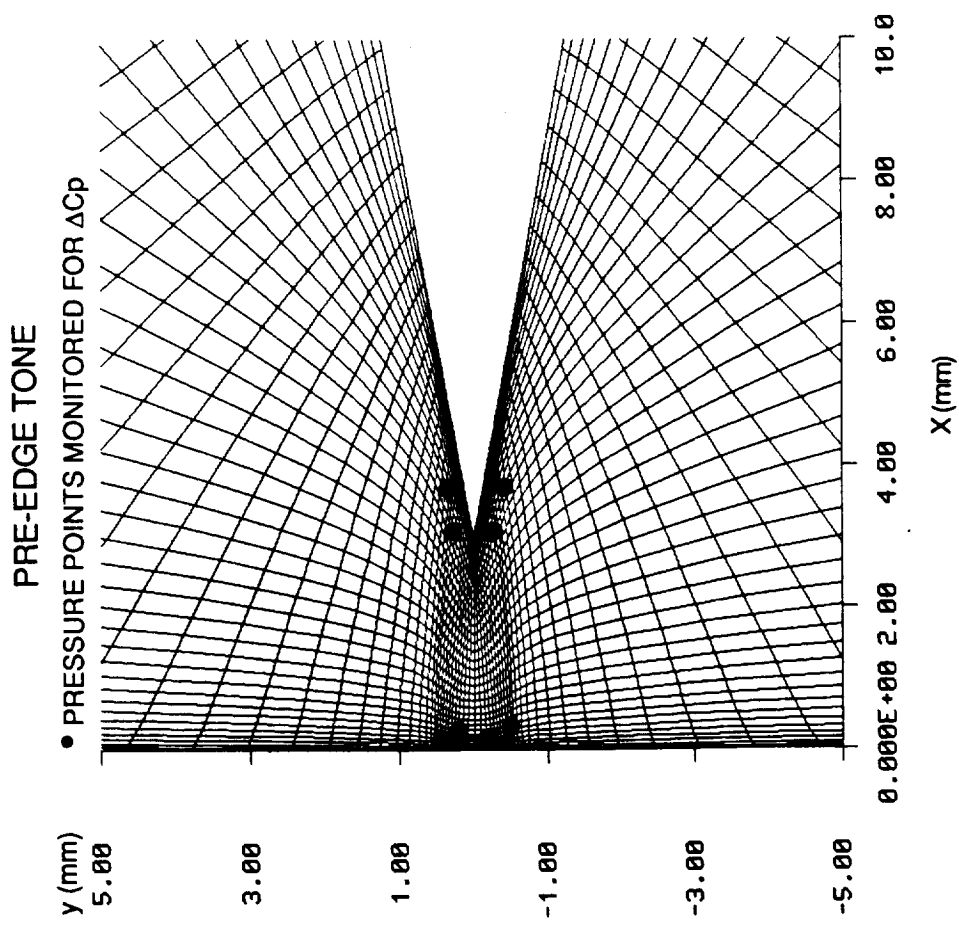


Figure 4-3 Detail A, Jet Wedge System for Case 1
(0.30 cm)

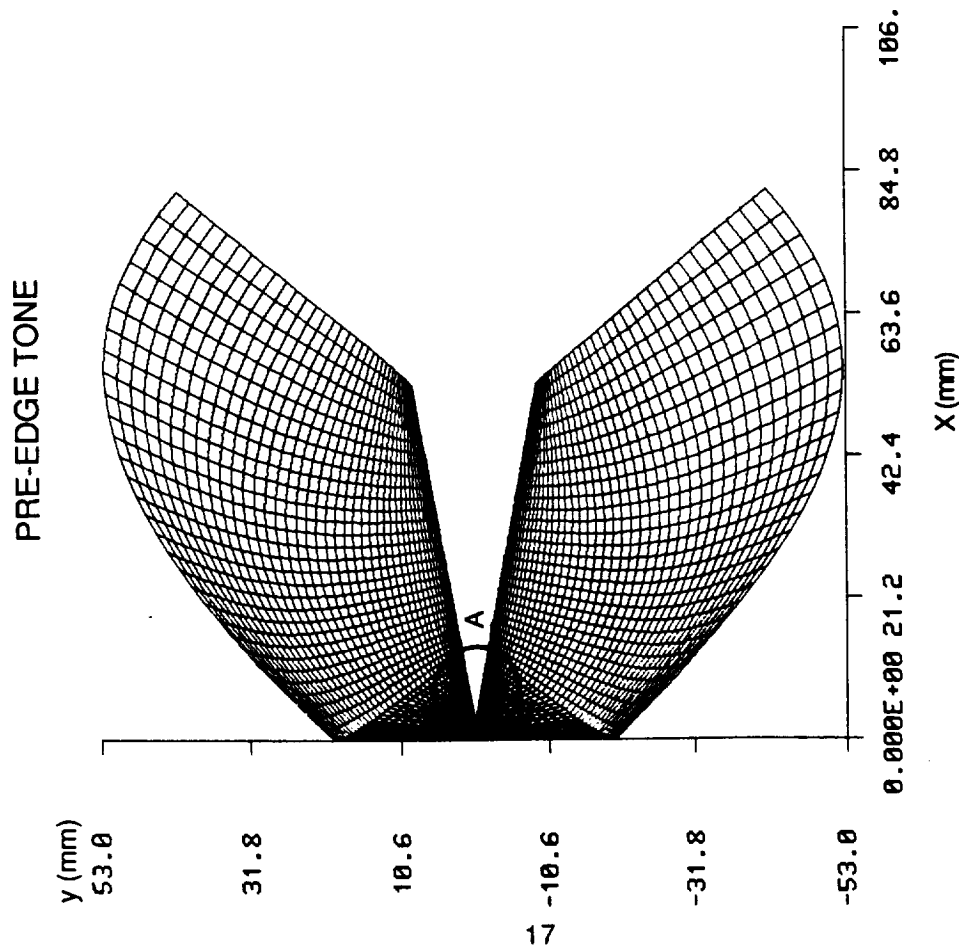


Figure 4-2 Computational Grid for Case 1 (0.30 cm)

PRE-STAGE

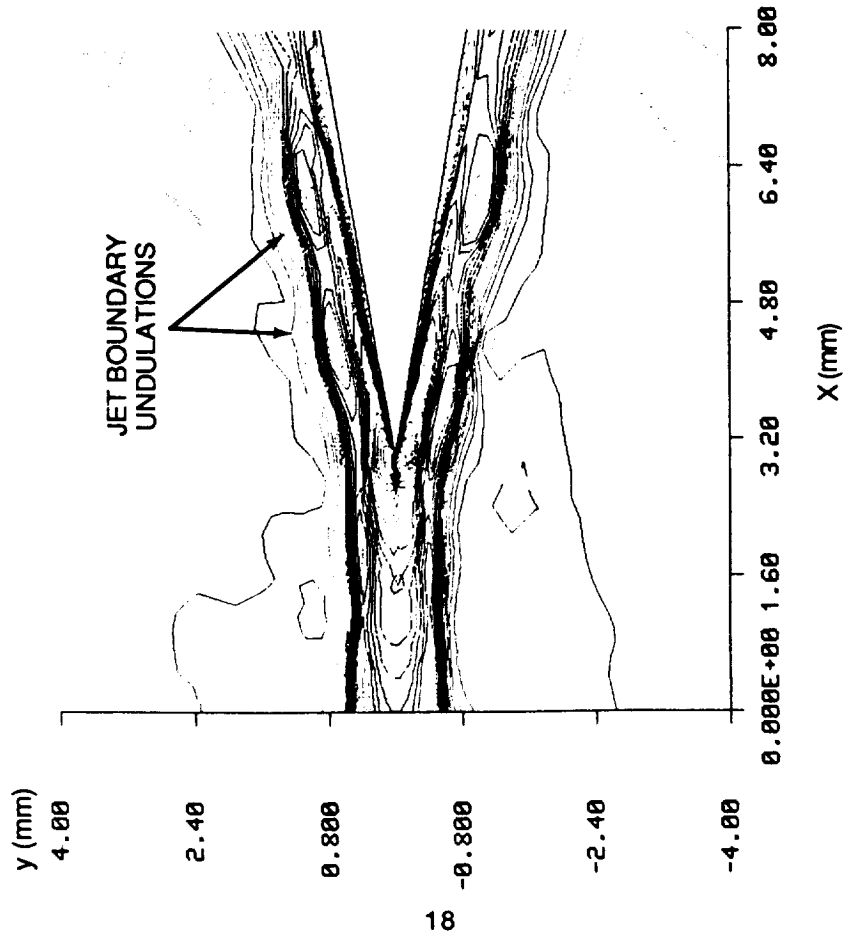


Figure 4-4 Detail A, Density Contours for Case 1 (0.30 cm)

PRE-STAGE

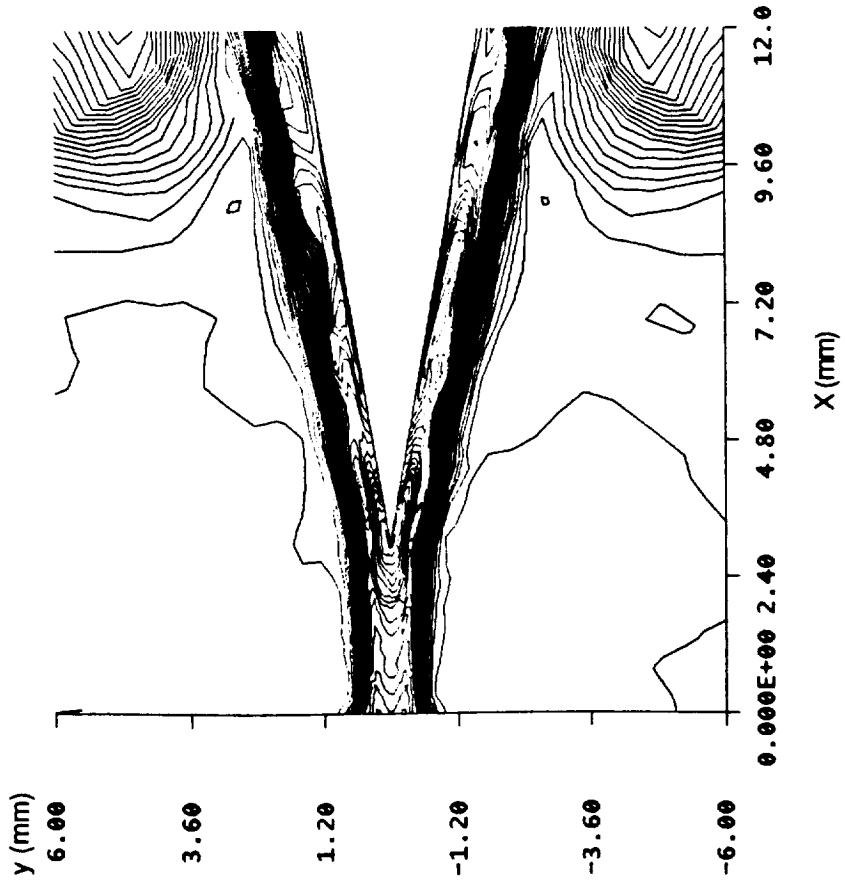


Figure 4-5 Enthalpy Contours for Case 1 (0.30 cm)

PRE-STAGE

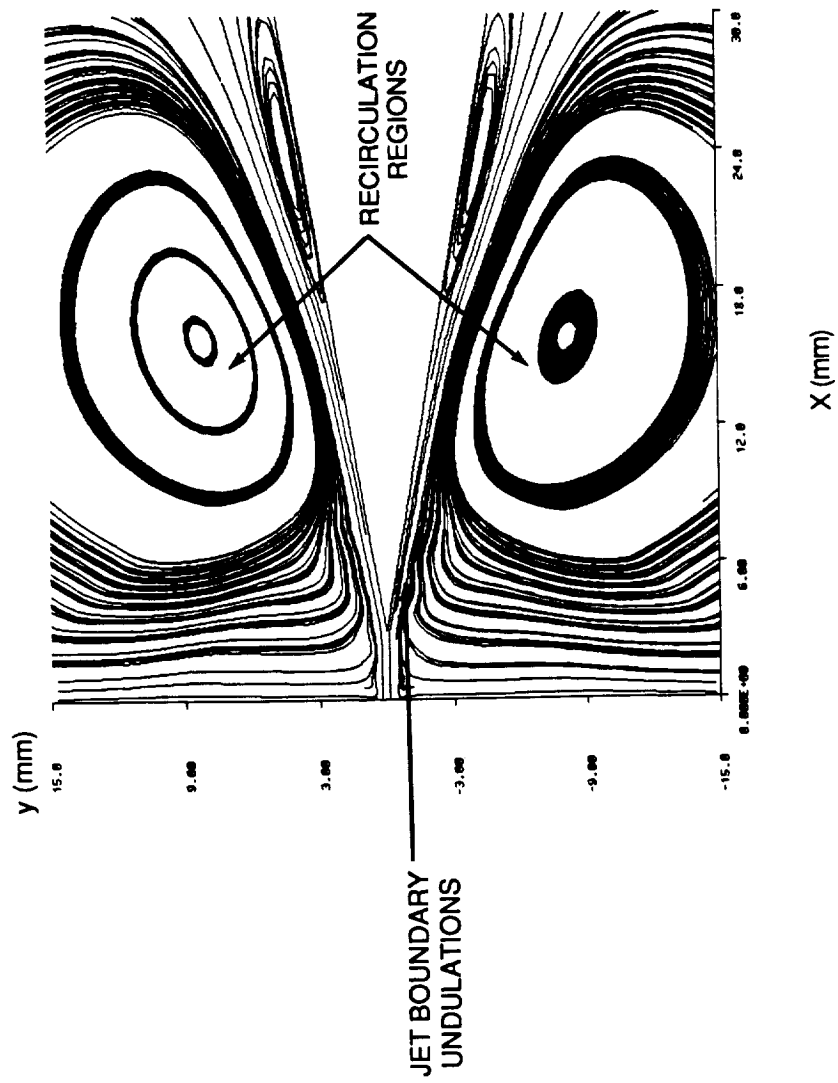


Figure 4-6 Streamlines for Case 1 (0.30 cm)

PRE-STAGE

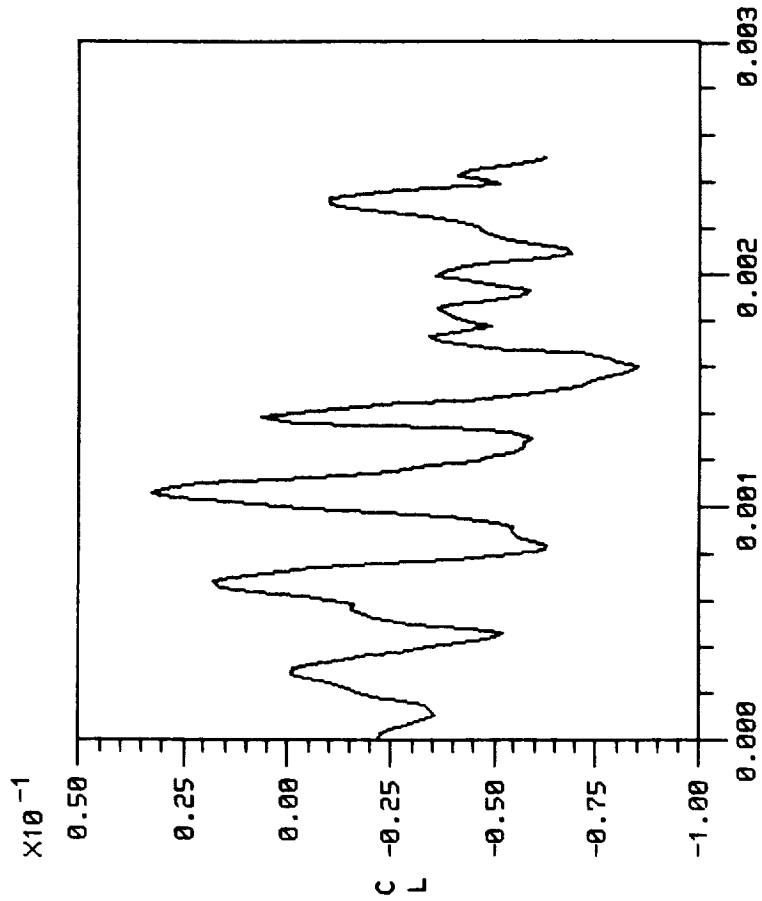


Figure 4-7 Lift Coefficient Time History for Case 1 (0.30 cm)

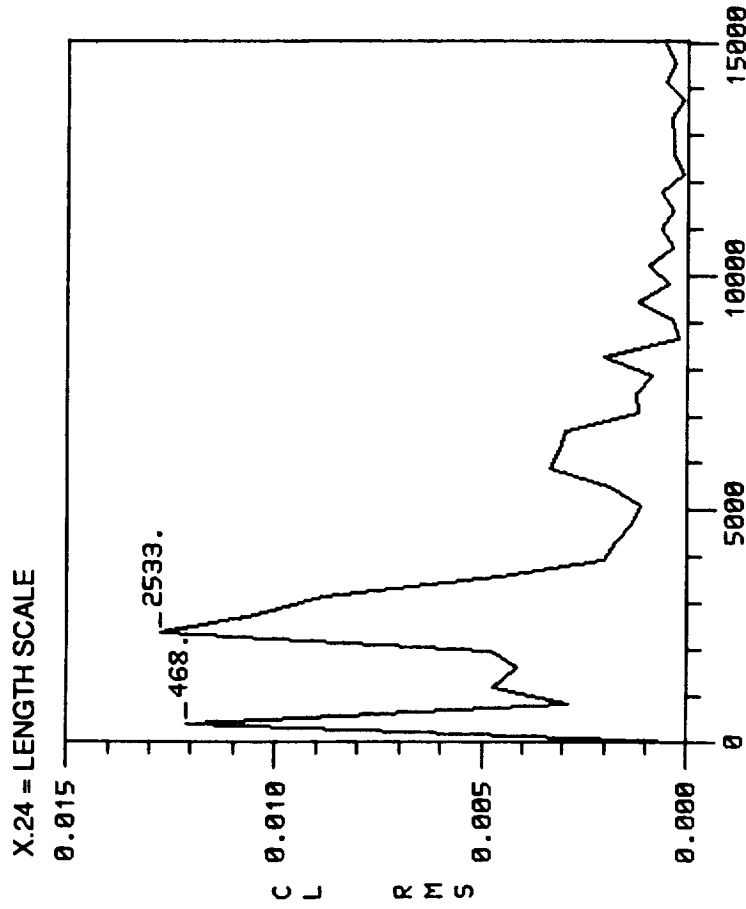


Figure 4-8 Frequency Analysis for Case 1 (0.30 cm)

Stage I Edge Tone (0.33 cm)

The grid system employed for this Stage I edge tone simulation (Case 2) is illustrated in Figures 4-9 and 4-10. A velocity directions plot (arrows scaled to grid size, not velocity vector magnitudes), Figure 4-11, illustrates the main flow features for Case 2. Vortices shed from the lips of the orifice travel downstream. The upper vortex has impinged on and is above the wedge apex. The lower vortex is more than half-way from the orifice to the wedge apex and is beginning to impinge on the apex. Transverse flow entrainment inward is evident and there is a small stagnation region on the vertical wall below the jet orifice. The velocity-direction plot confirms that the lower vortex approaching the wedge apex is clockwise (CW) and the upper vortex is counterclockwise (CCW). The wedge acts as a divider for the flow, inducing vortices over the both surfaces of the wedge. Downstream of the large vortices, two smaller and narrower separation regions on the wedge are seen counter-rotating to these large vortices. The flow field is clearly dynamic with primary sound generation due to the vortex impingement near the wedge apex.

Figures 4-12 and 4-13 contain Mach number contours showing the oscillating motion of the jet. The velocity in the narrow region between the upper CCW vortex and the wedge apex is high and therefore the pressure is low above the wedge apex as shown in the pressure contour plots Figures 4-14 and 4-15. On the other hand, the velocity is lower and the pressure is higher on the lower side of the wedge apex. The alternate low and high pressure contours are indicative of an acoustic dipole.

Figures 4-16 and 4-17 illustrate time history plots of the lift coefficient and FFT frequency analysis results. The lift coefficient frequency and C_p data agree well with Brown's data, Table 4-1. Since Case 1 is a pre-edge tone case and Case 3 is a regular Stage I edge tone case, Case 2 is very close to the on-set of edge tones where Brown was able to first detect audible sound..

STAGE I

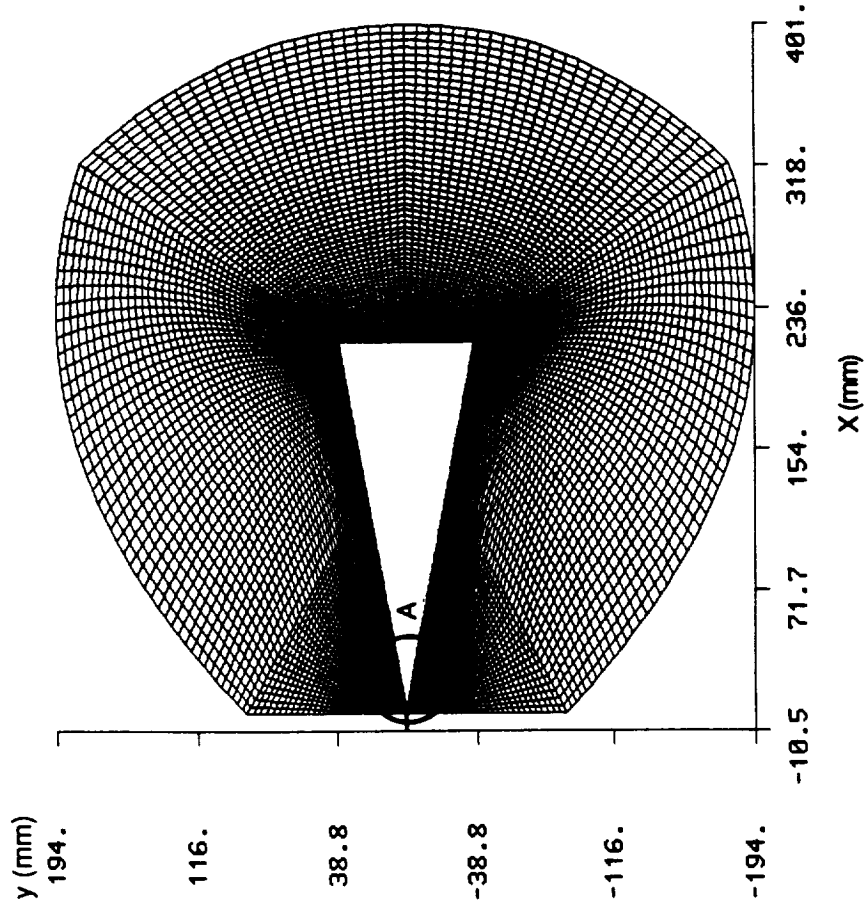


Figure 4-9 Computational Grid for Case 2 (0.33 cm)

STAGE I

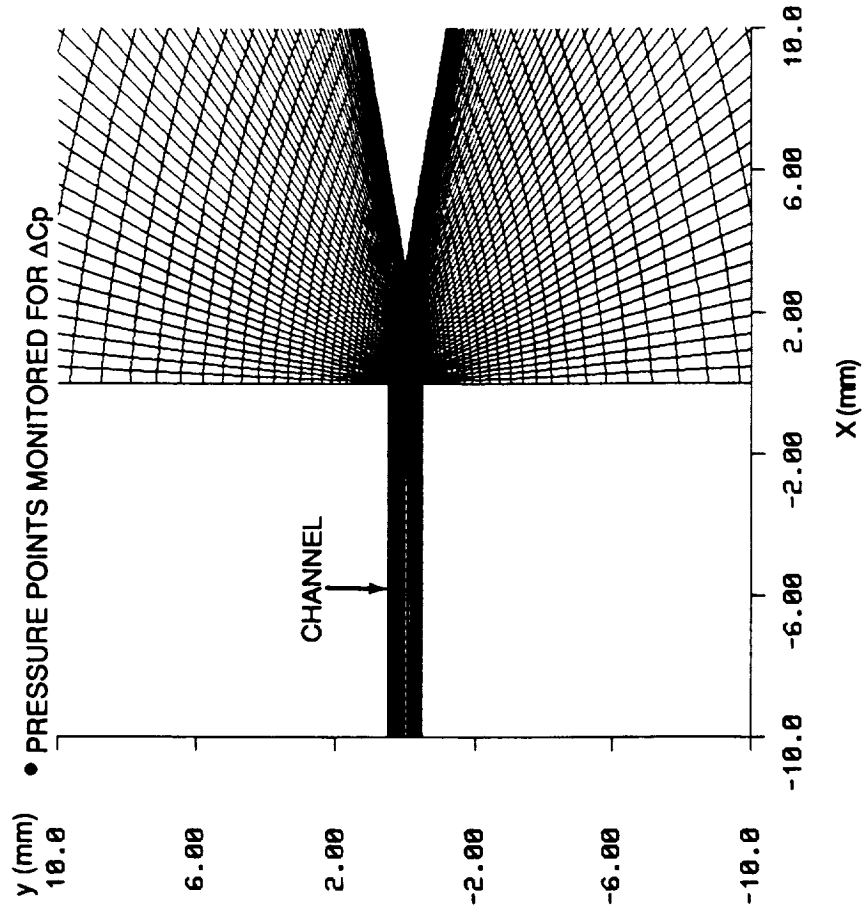


Figure 4-10 Detail A, Jet Wedge System for Case 2 (0.33 cm)

STAGE I

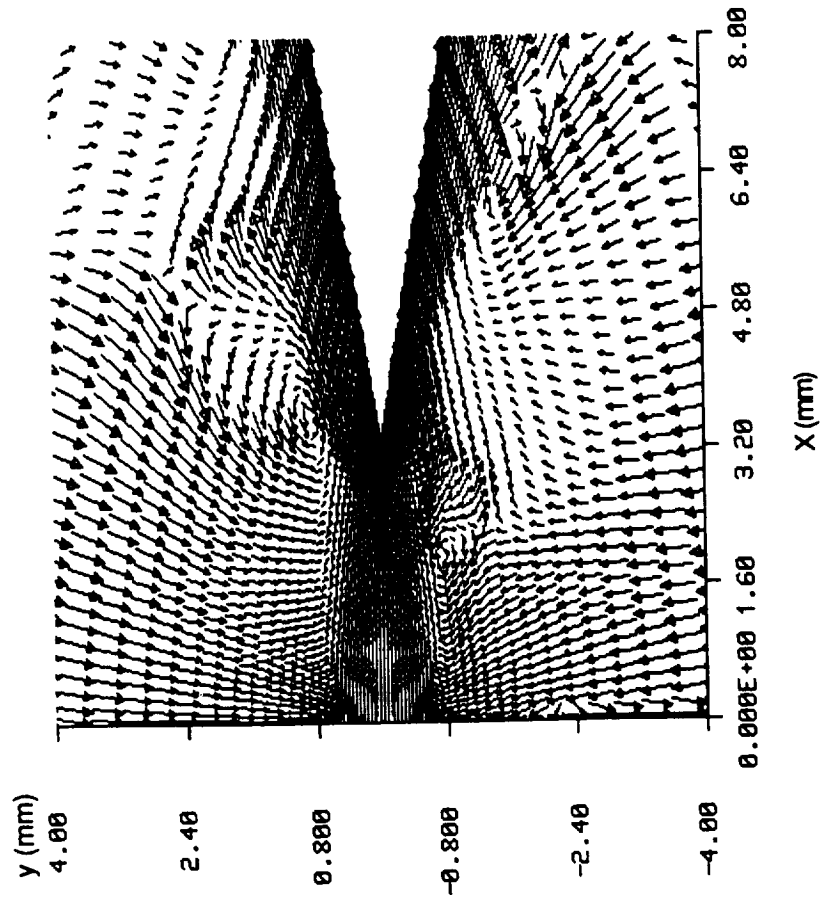


Figure 4-11 Velocity Directions for Case 2 (0.33 cm)

STAGE I

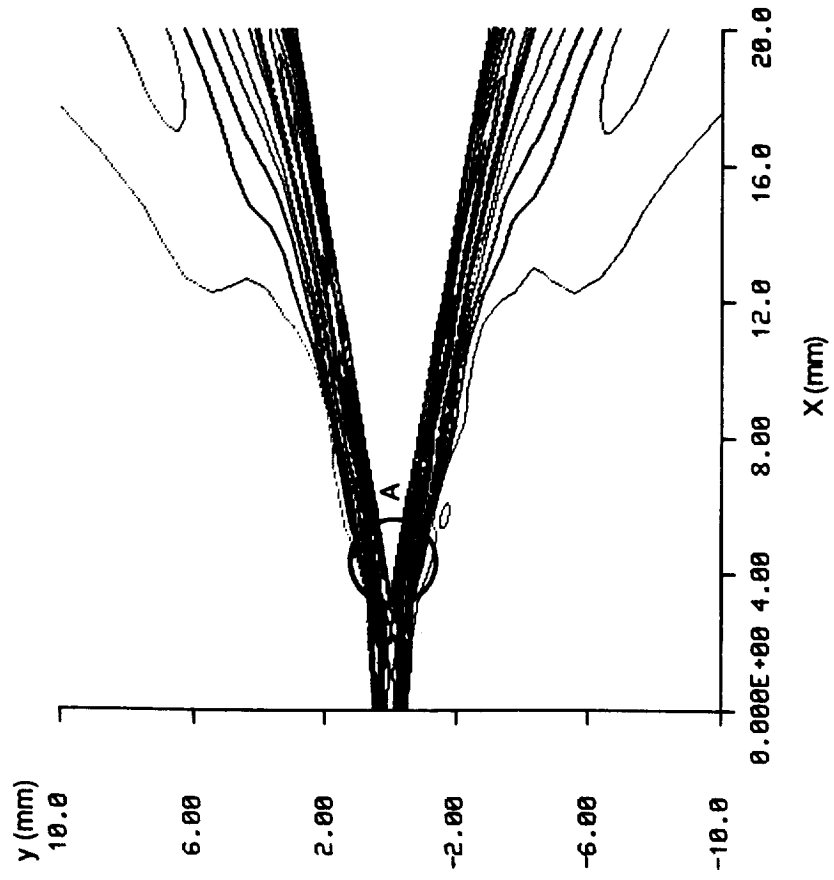


Figure 4-12 Mach Number Contours for Case 2 (0.33 cm)

STAGE I

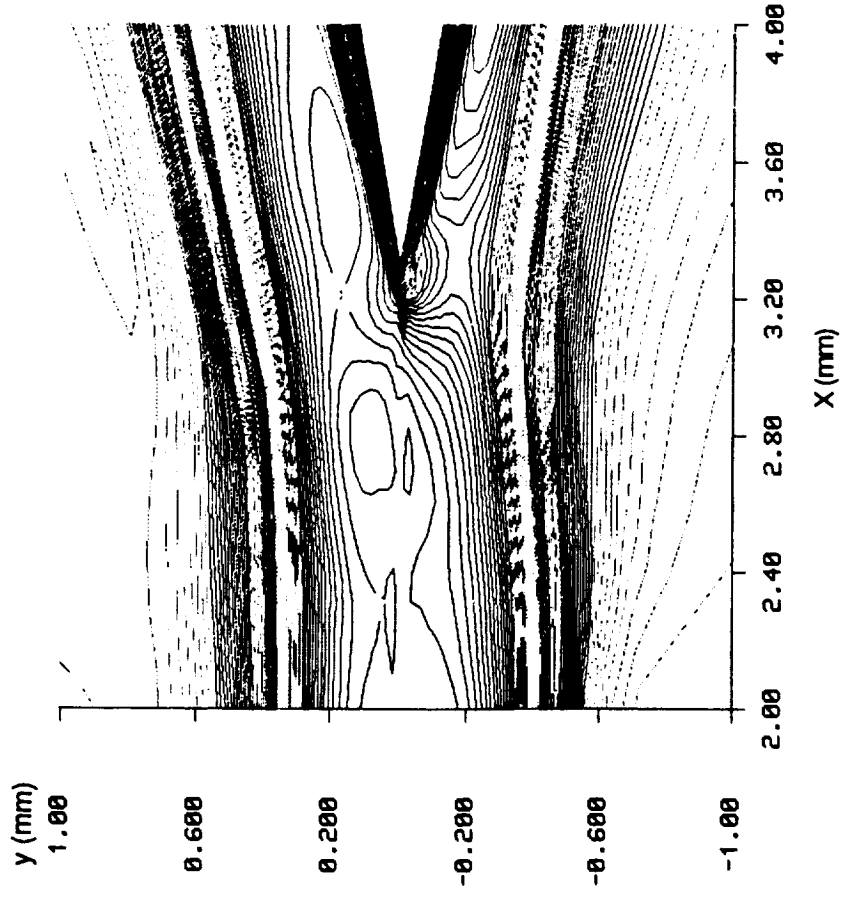


Figure 4-13 Detail A, Mach Number Contours for Case 2 (0.33 cm)

STAGE I

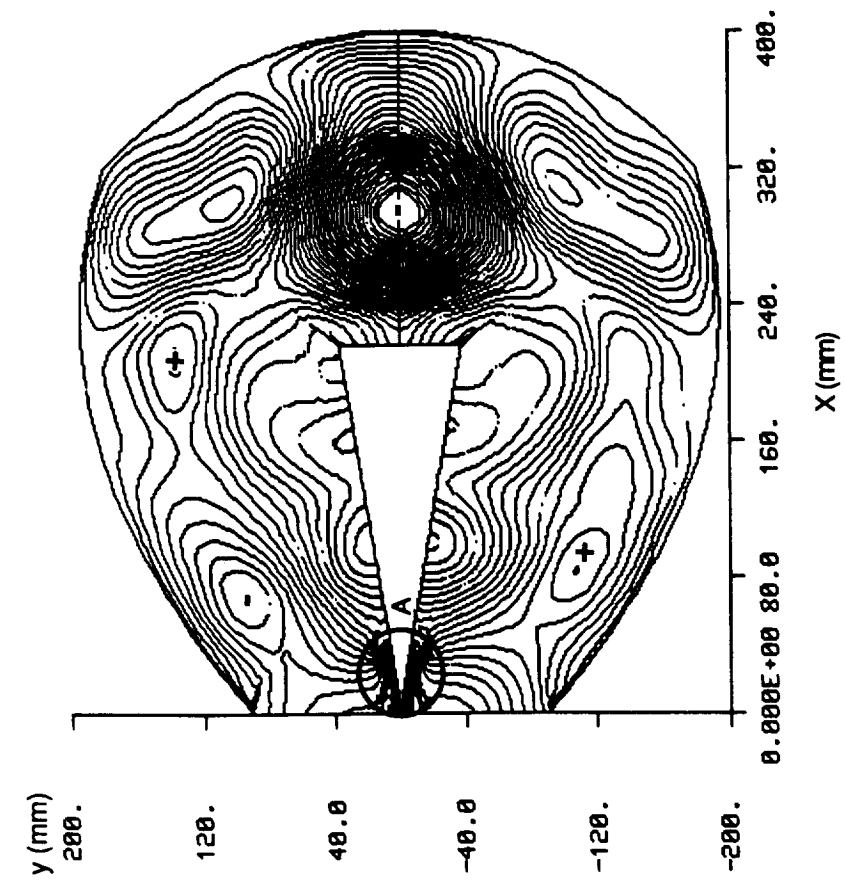


Figure 4-14 Pressure Contours for Case 2 (0.33 cm)

STAGE I

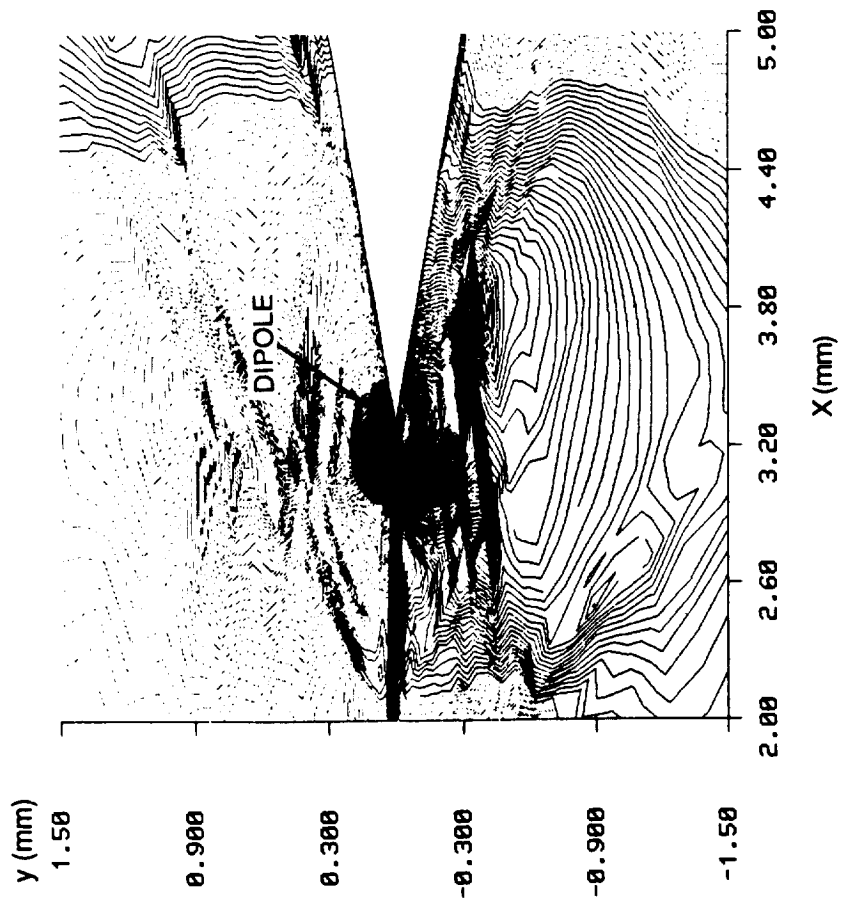


Figure 4-15 Detail A, Pressure Contours Case for Case 2 (0.33 cm)

STAGE I

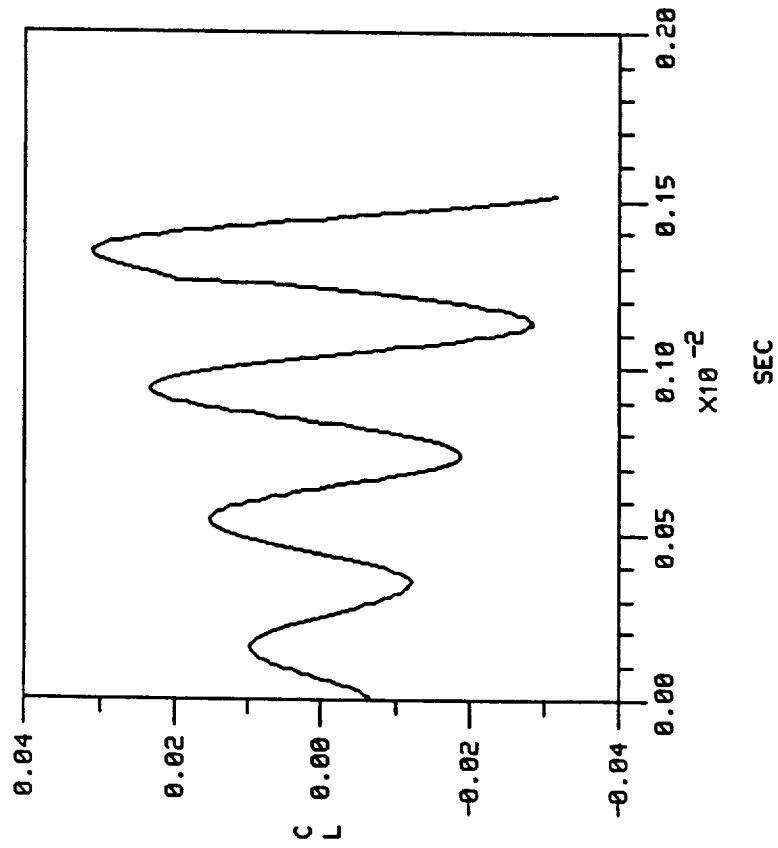


Figure 4-16 Lift Coefficient Time History for Case 2 (0.33 cm)

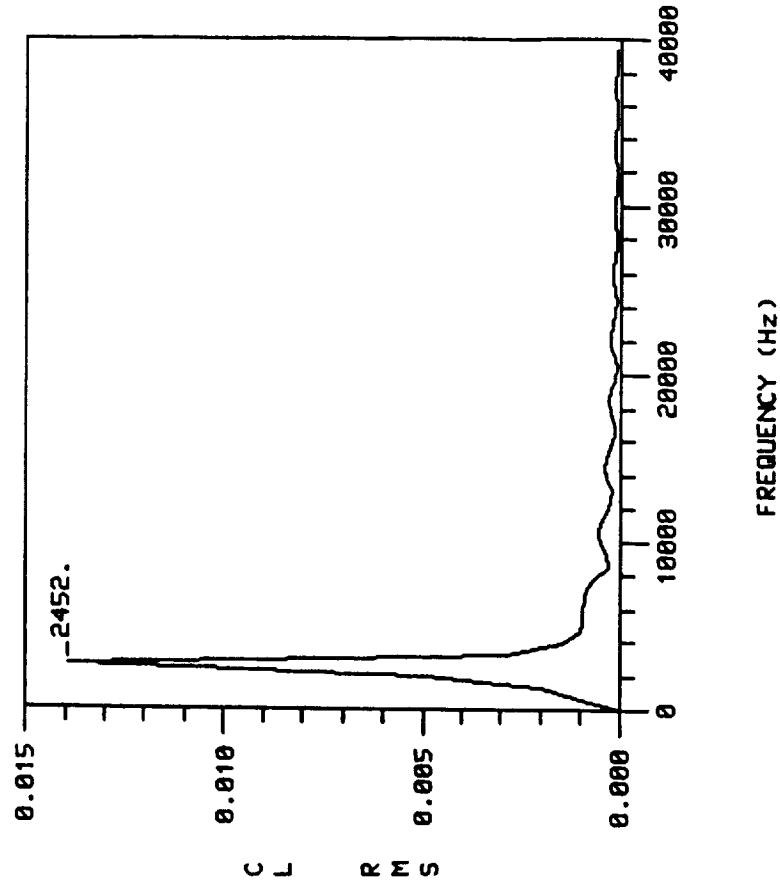


Figure 4-17 Frequency Analysis for Case 2 (0.33 cm)

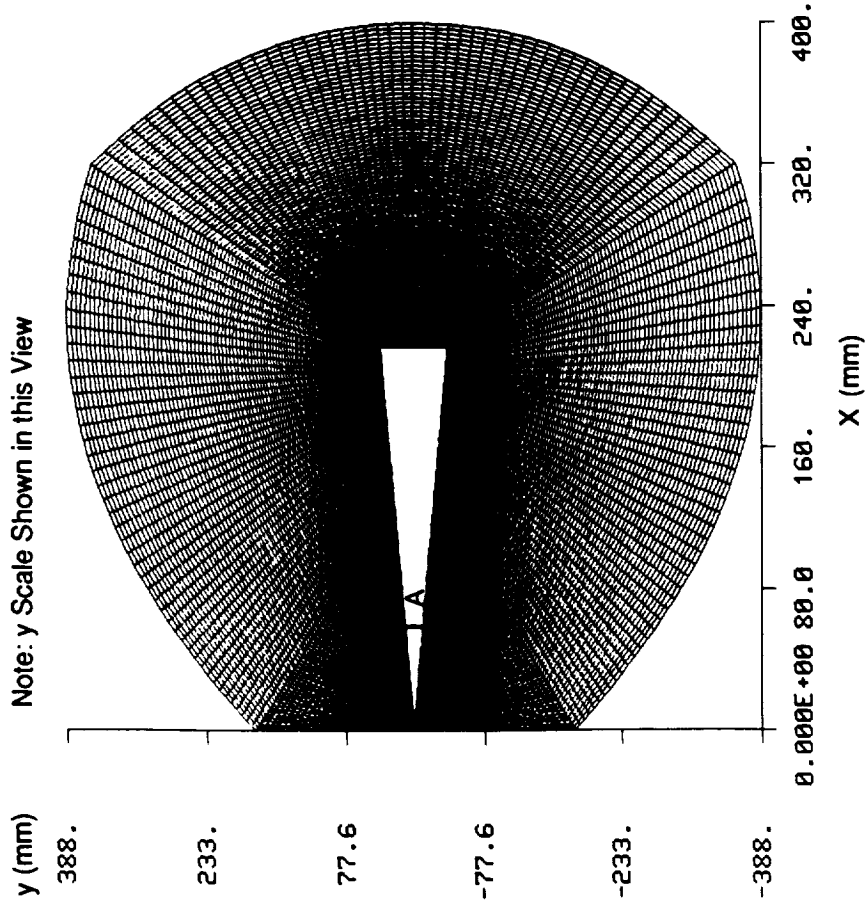
Stage I Edge Tone (0.40 cm)

The grid system employed for this Stage I edge tone simulation is illustrated in Figures 4-18 and 4-19. The flow perturbation under the influence of vortices impinging on the wedge apex is evident in density and enthalpy contour plots, Figures 4-20 and 4-21. A streamline plot, Figure 4-22, indicates the relative positions and distances between vortices which have been shed from the jet orifice corners. The alternate vortex impingement pattern is clearly illustrated in the velocity directions plot, Figure 4-23. The wedge apex plots indicate the dynamic oscillating dipole feature of the edge tone flow fields.

The pressure coefficient time history plot, Figure 4-24, for a point near the wedge apex, exhibits the expected first stage frequency generated by the acoustic dipole. The peak frequency derived from the FT analysis, illustrated in Figure 4-25 is 1902 Hz and the rms amplitude is 0.68.

STAGE I

Note: y Scale Shown in this View



STAGE I

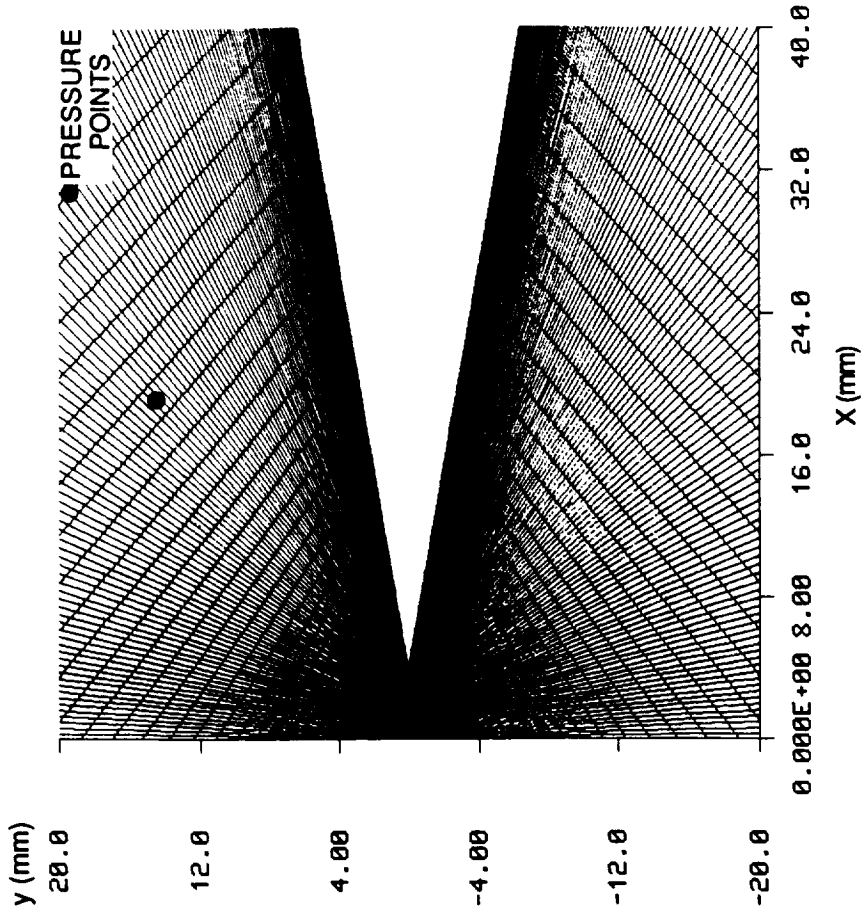


Figure 4-18 Computational Grid for Case 3 (0.40 cm)

Figure 4-19 Detail A, Computational Grid for Case 3 (0.40 cm)

STAGE I

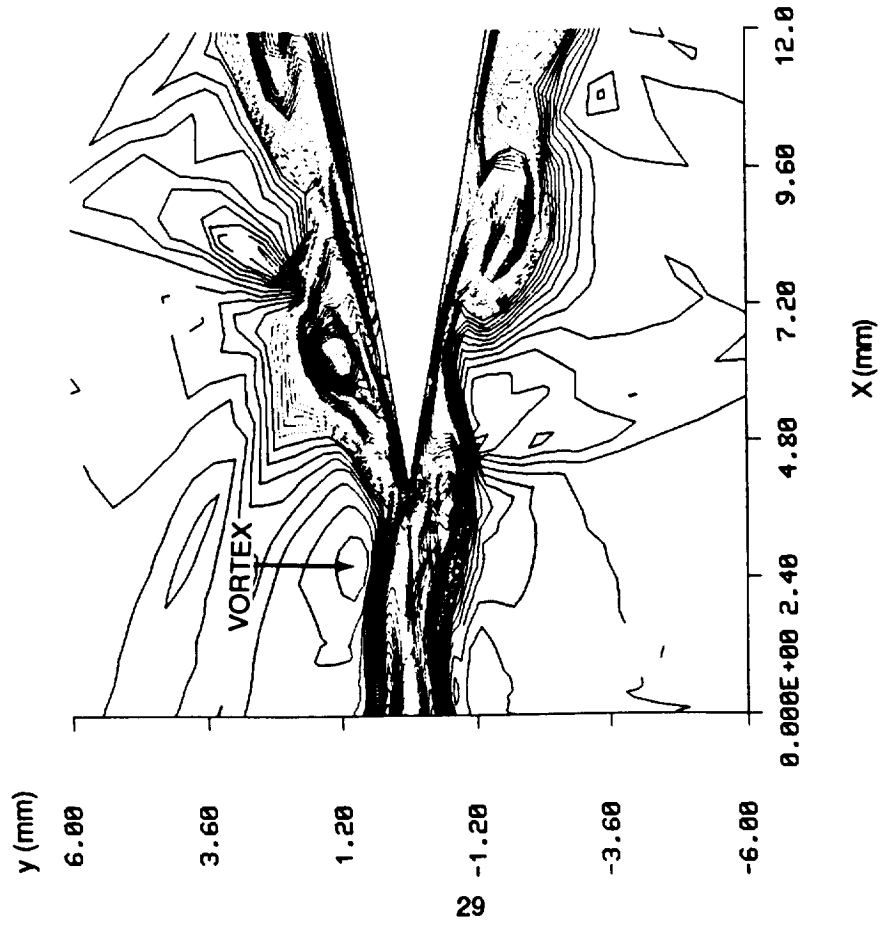


Figure 4-20 Density Contours for Case 3 (0.40 cm)

STAGE I

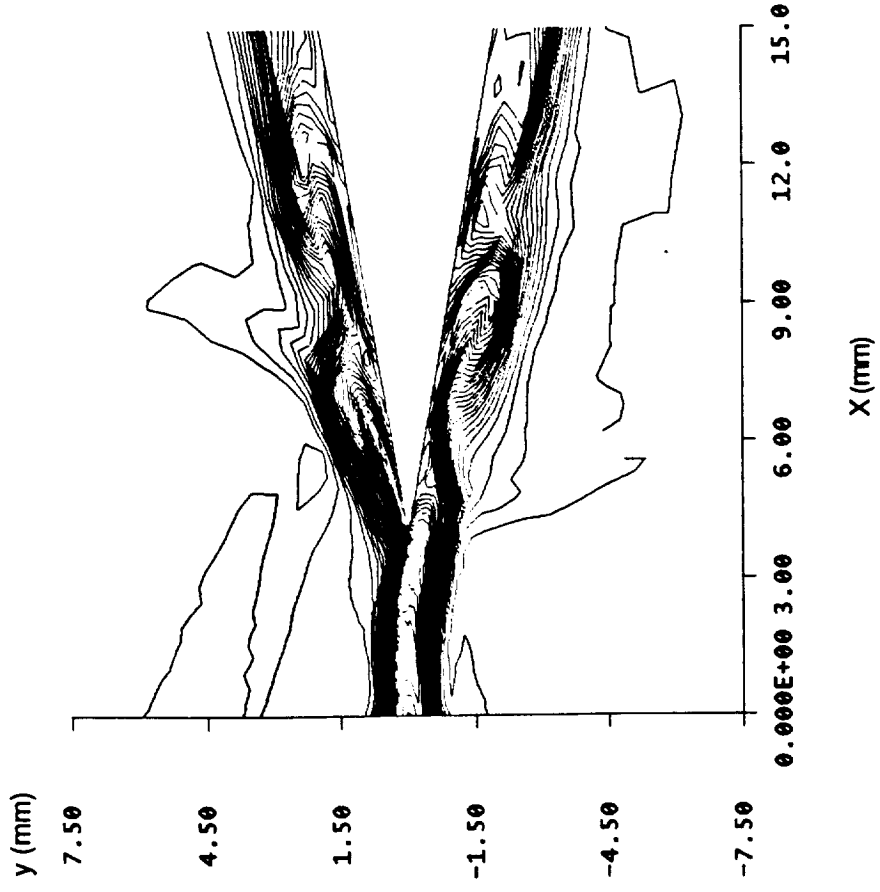


Figure 4-21 Enthalpy Contours for Case 3 (0.40 cm)

STAGE I

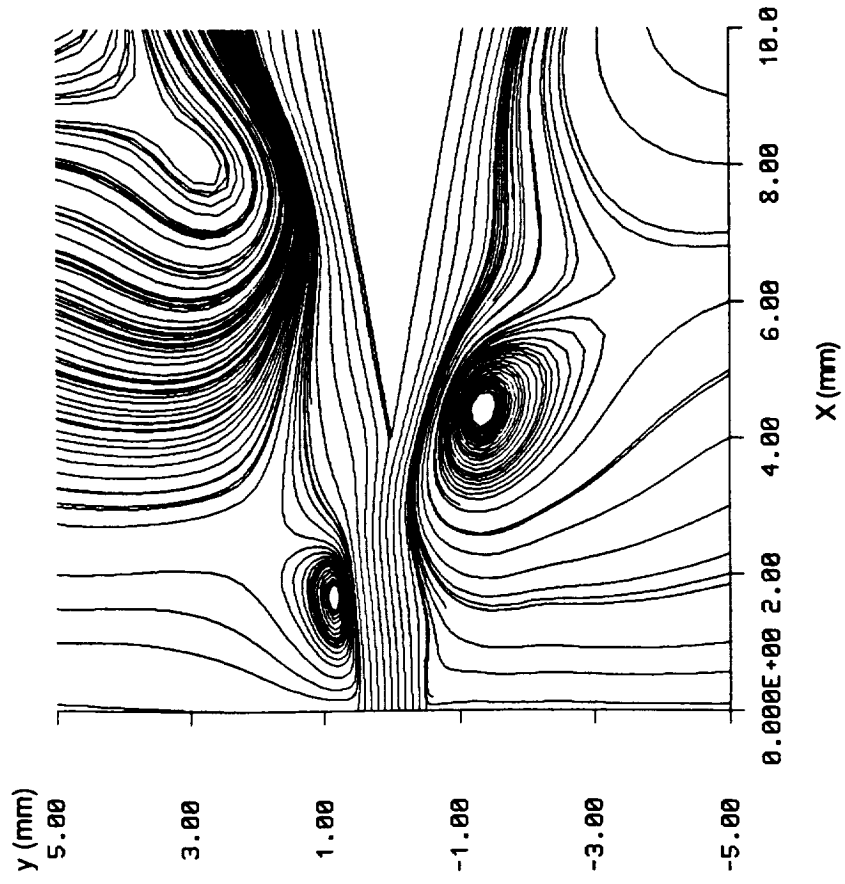


Figure 4-22 Streamlines for Case 3 (0.40 cm)

STAGE I

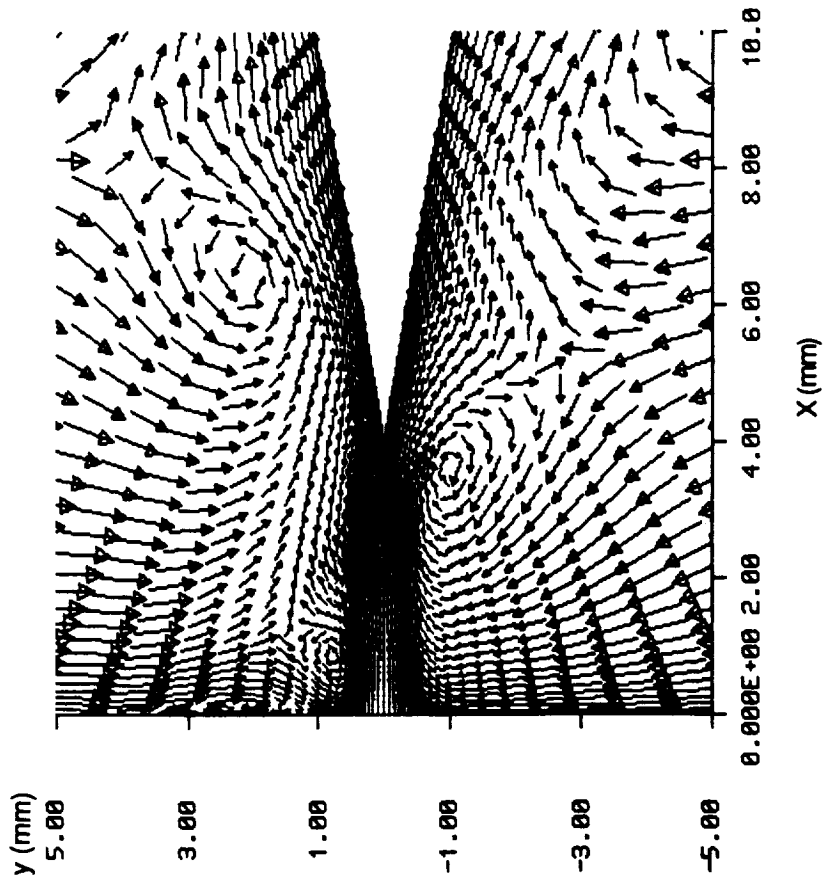


Figure 4-23 Velocity Directions for Case 3 (0.40 cm)

STAGE I

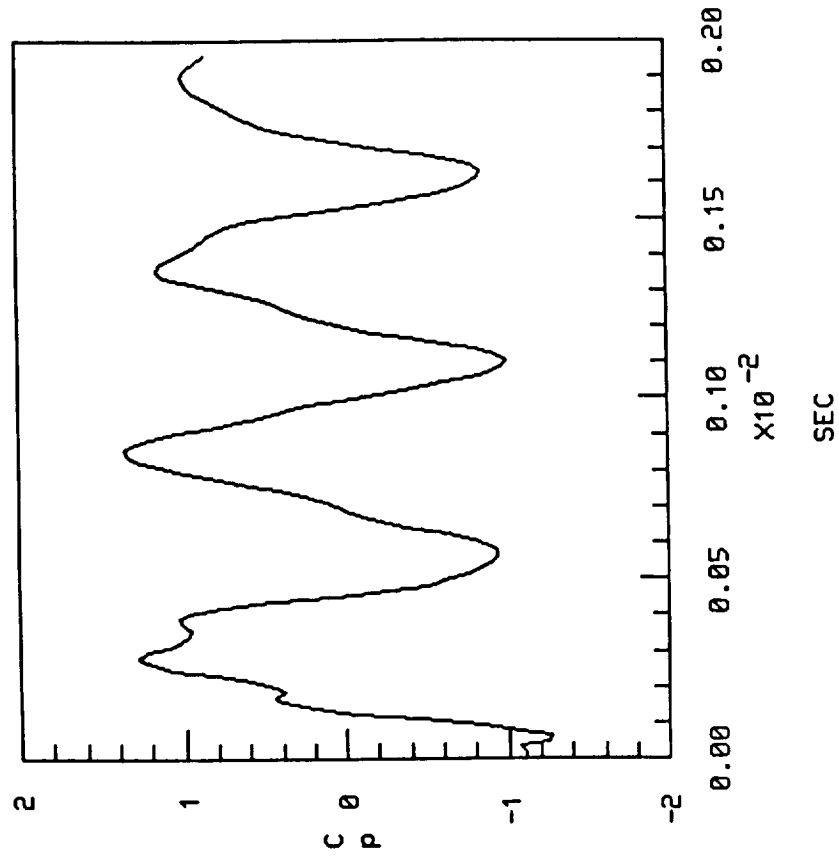


Figure 4-24 Pressure Coefficient at Point Near Wedge Apex for Case 3 (0.40 cm)

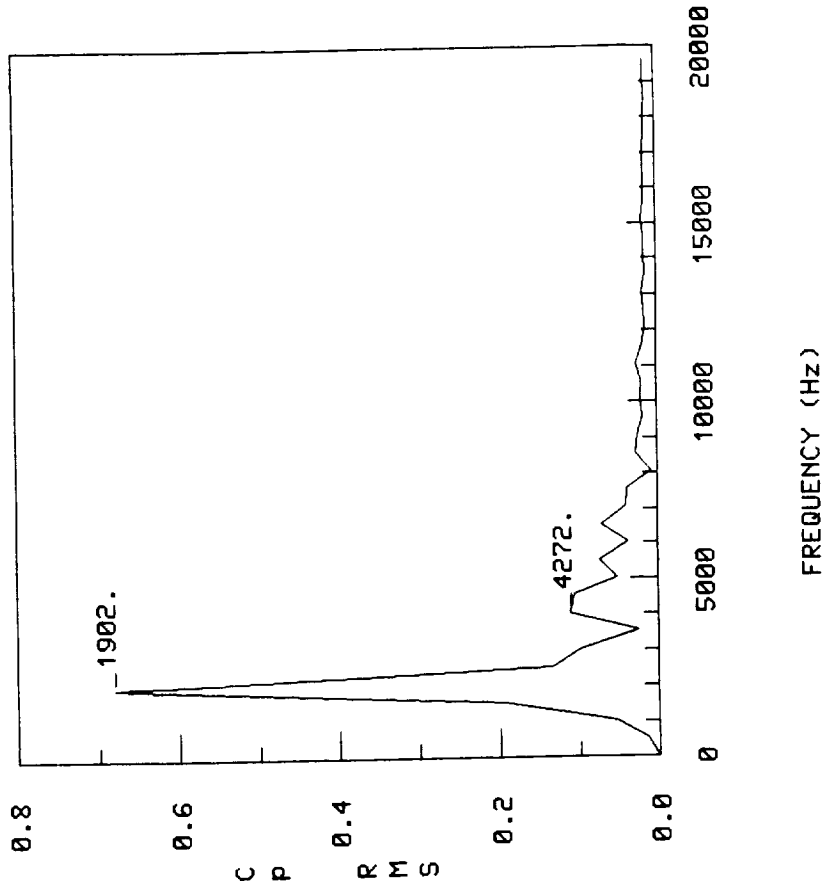


Figure 4-25 Frequency Analysis at Point Near Wedge Apex for Case 3 (0.40 cm)

Stage II Edge Tone (0.56 cm)

The grid system employed for this Stage II edge tone simulation is illustrated in Figures 4-26 and 4-27. Jet interaction with the wedge is more pronounced here than in previous cases. These resemble the smoke picture of Brown¹. As a Stage II case, there is a undulation crest in the jet which agrees with Brown's observation.

As indicated by the near-field plots, Figure 4-28 through 4-30, the vortex transport wave length is approximately 0.26 cm. As measured from the far-field pressure contours, Figure 4-31, the acoustic transport wavelength, λ , is approximately 11.0 cm. This agrees with the fact that the acoustic speed is 42.5 times greater than the vortex transport speed in this simulation.

Figure 4-32 and 4-33 show the lift coefficient time history and frequency plots for Stage II. The major flow oscillation is due to vortex impingement, which is at the Stage I frequency of 1281 Hz. Jet instability causes the flow undulation vortex transport wavelength at the Stage II frequency of 3177 Hz. The present computation indicates that the higher stages are due to the jet-vortex induced undulations. Brown observed that at jet velocities above 500 to 600 cm/sec, Stage I co-exists with each of other stages.

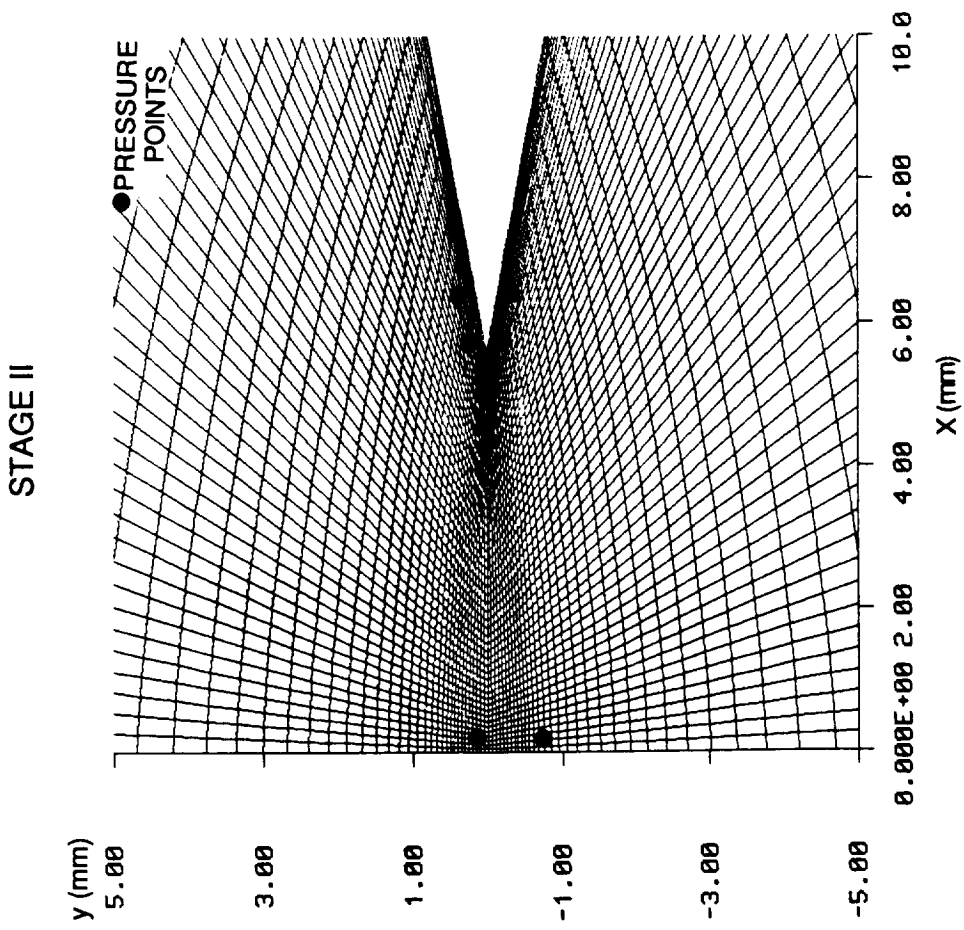


Figure 4-27 Detail A, Jet Wedge System for Case 4 (0.56 cm)

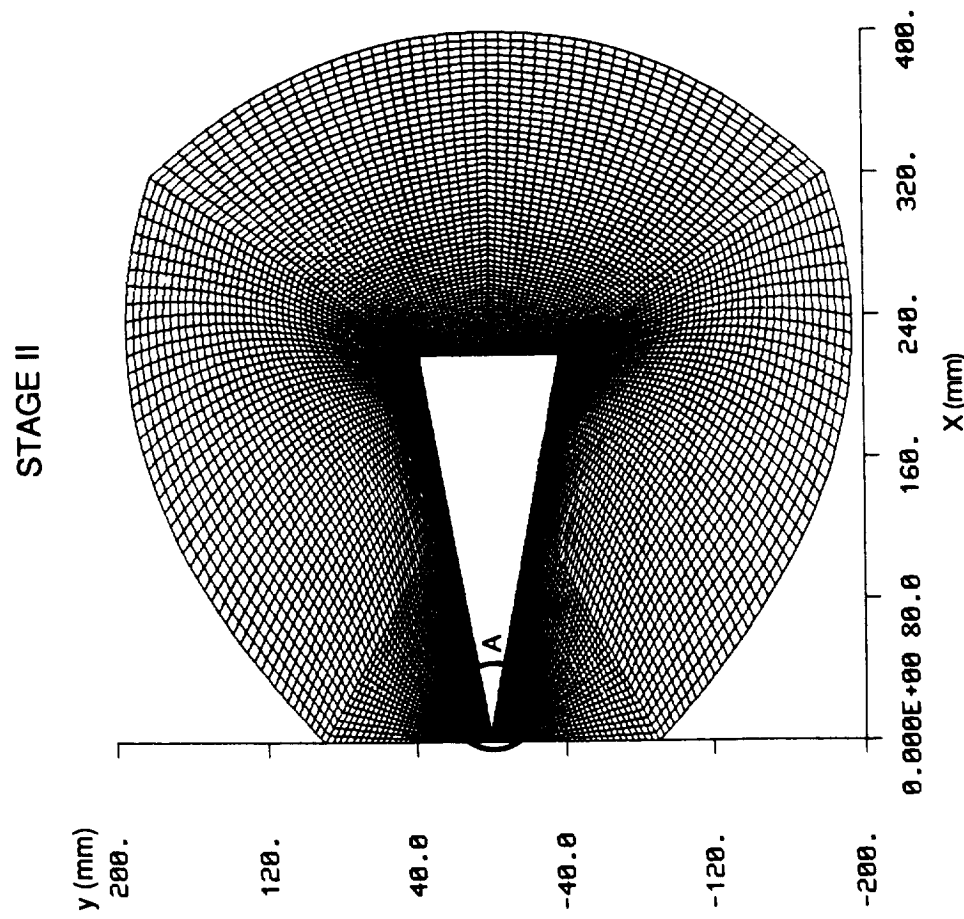
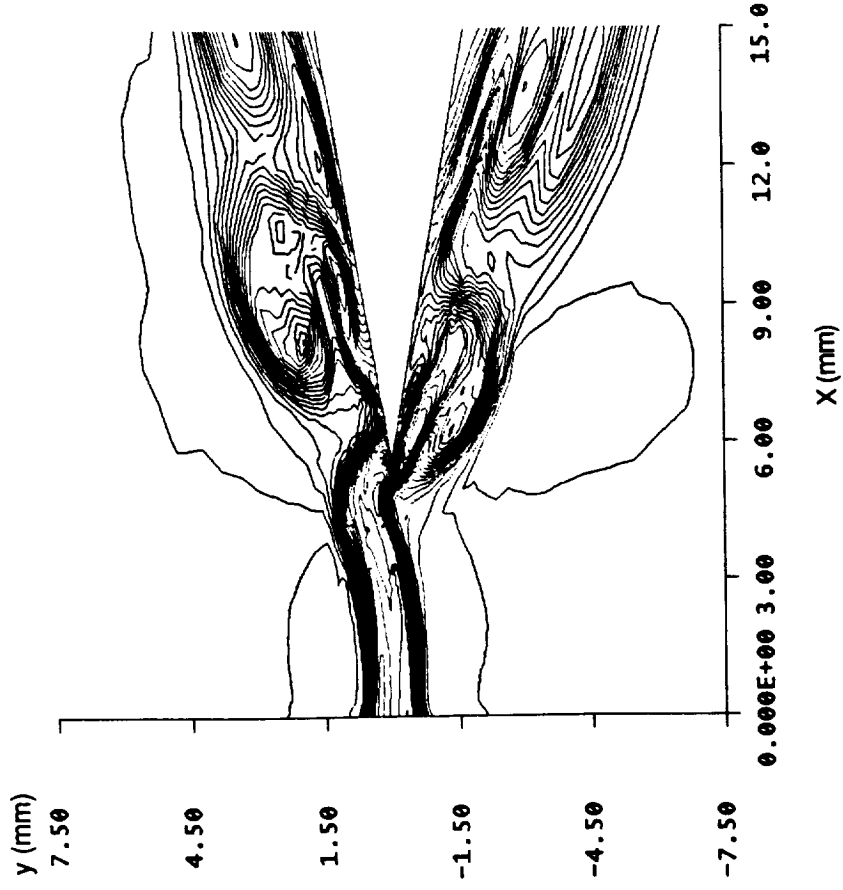


Figure 4-26 Computational Grid for Case 4 (0.56 cm)

STAGE II



STAGE II

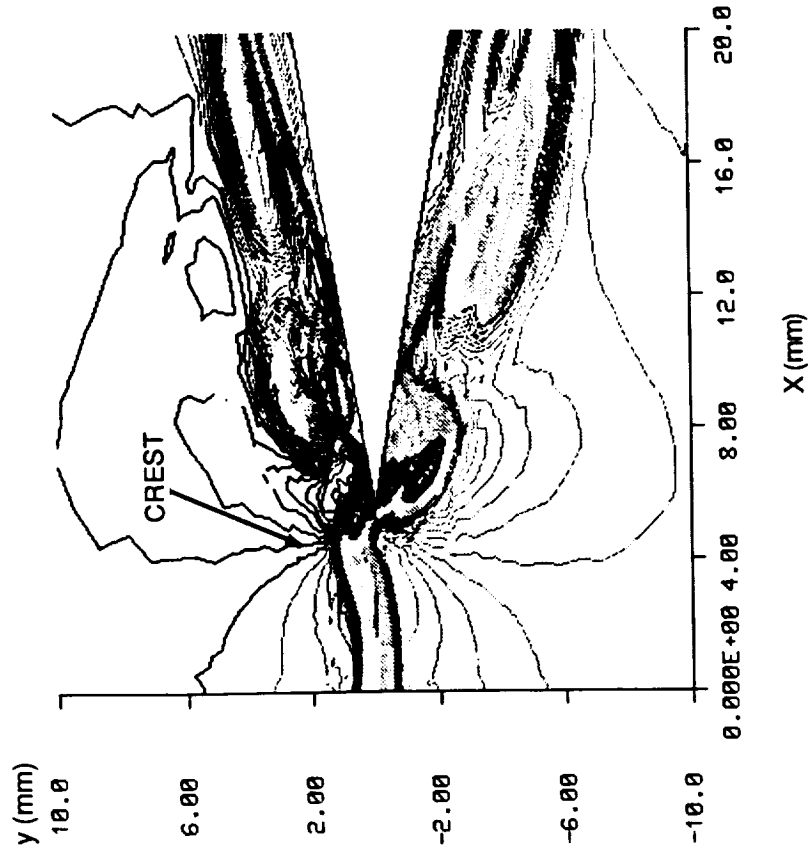


Figure 4-29 Enthalpy Contour for Case 4 (0.56 cm)

Figure 4-28 Density Contour for Case 4 (0.56 cm)

STAGE II

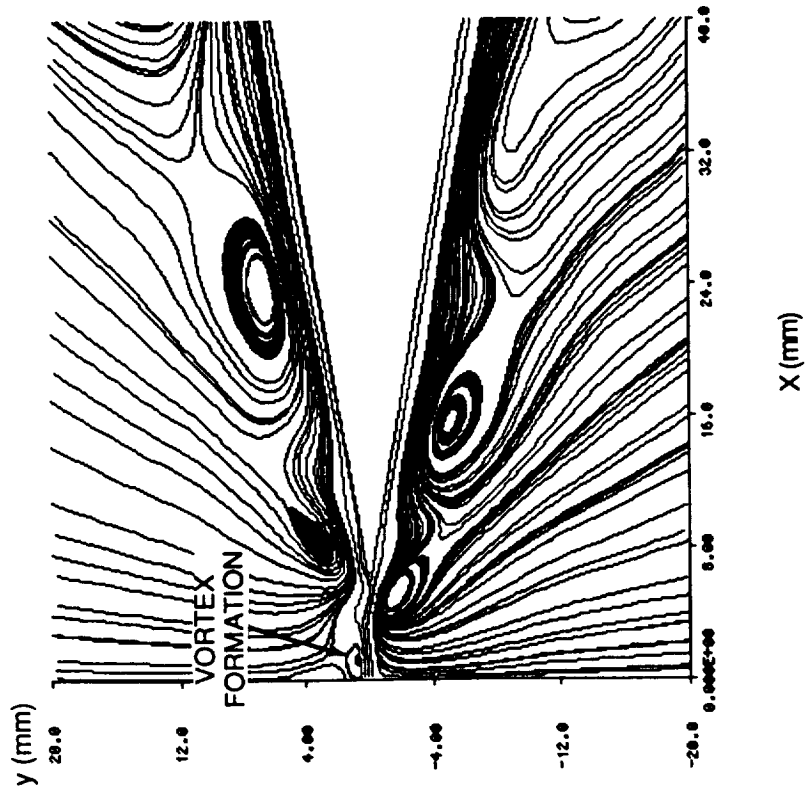


Figure 4-30 Streamlines for Case 4 (0.56 cm)

STAGE II

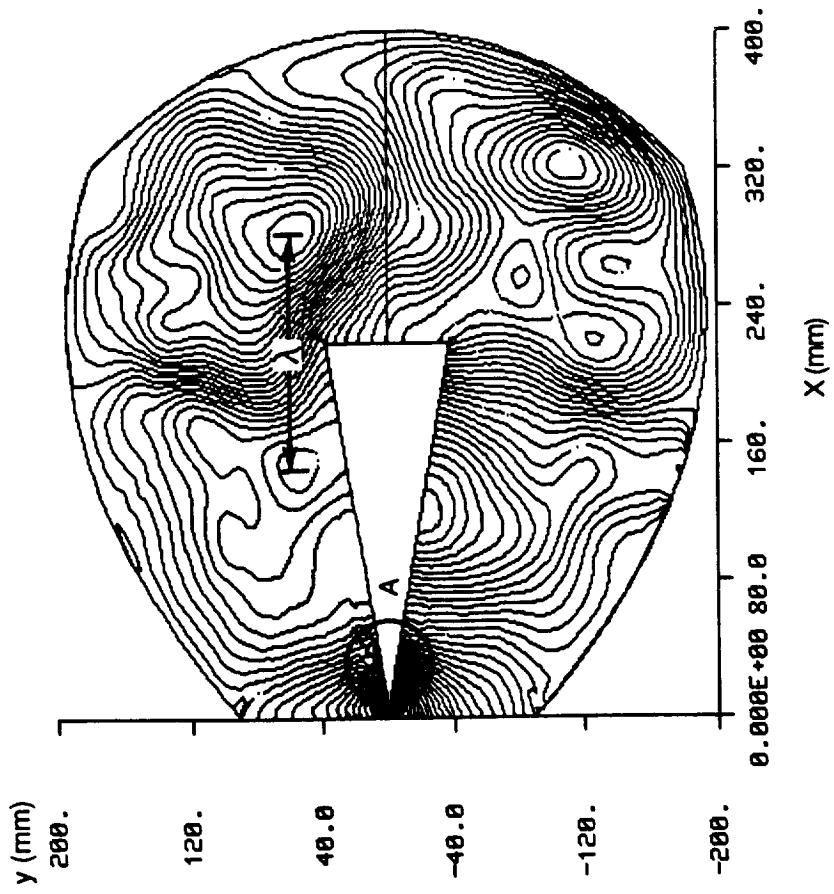


Figure 4-31 Pressure Contour for Case 4 (0.56 cm)

STAGE II

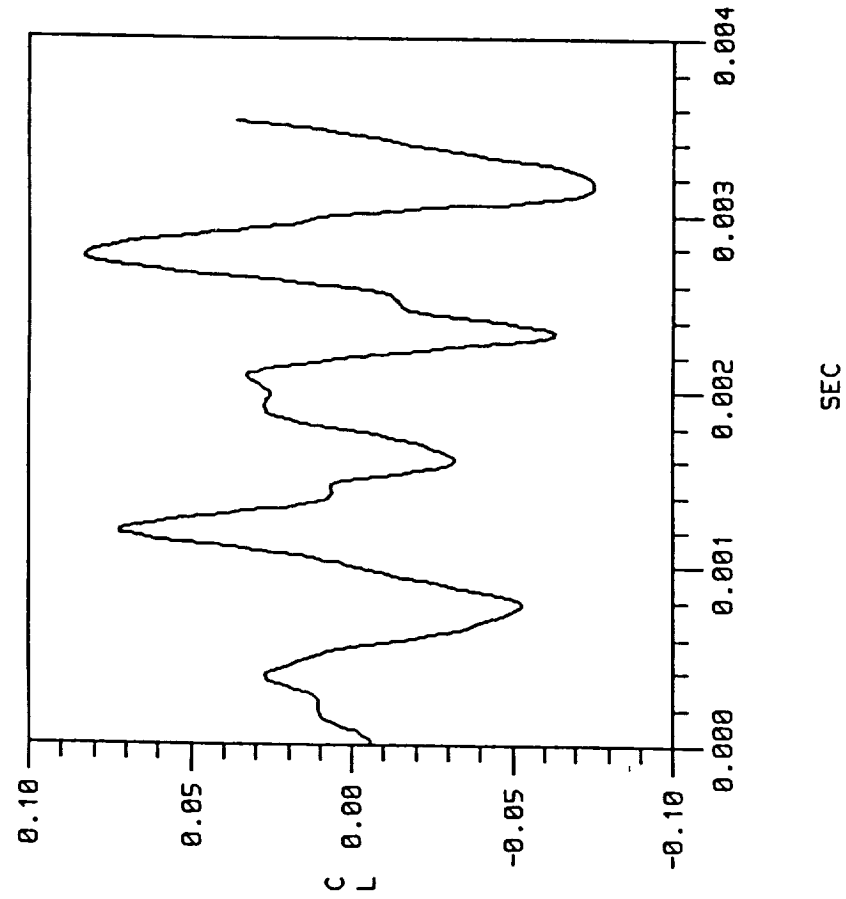


Figure 4-32 Lift Coefficient Time History for Case 4 (0.56 cm)

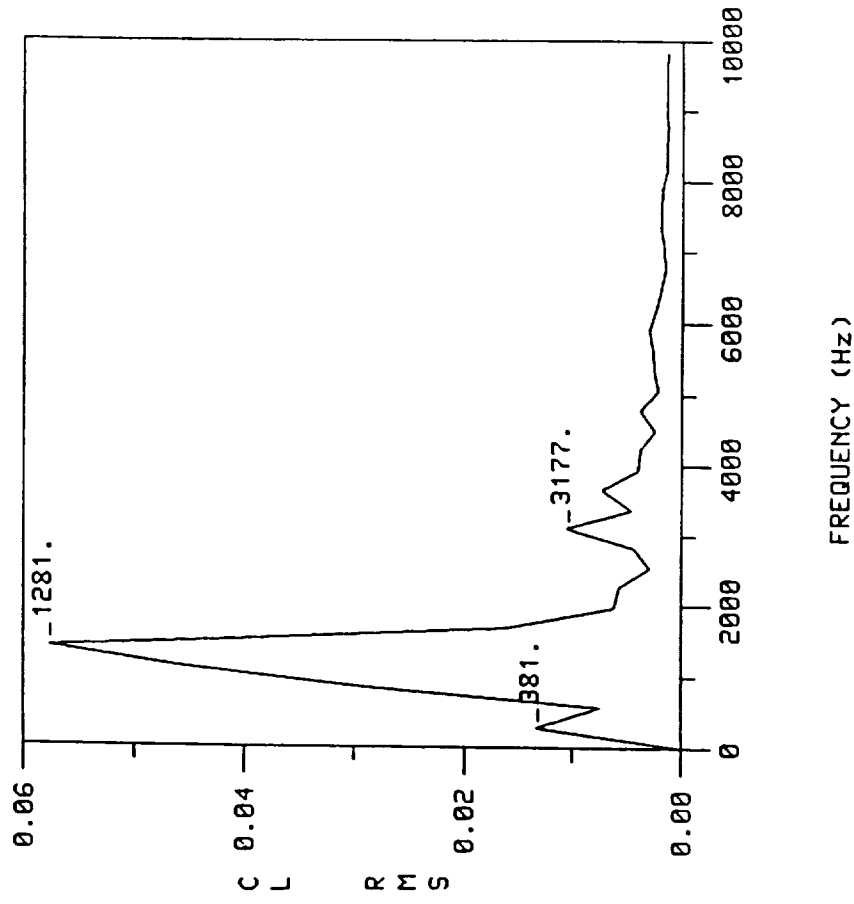


Figure 4-33 Frequency Analysis for Case 4 (0.56 cm)

Stage III Edge Tone (0.82 cm)

In this third stage edge tone simulation, the wedge was induced to vibrate with a one degree maximum angle-of-attack according to the expected Stage III frequency. In the literature, most work has been done for the first and second stages and little data can be found to support the third stage of Brown's data. A small structural vibration might exist in the experimental setup and, therefore, needed to be included in the numerical simulation. Hence, the other case incorporates a small wedge vibration (maximum 1 degree angle of attack) assuming that the structure of the wedge is excited at the third stage frequency. The 1.0 degree angle-of-attack is much smaller than the transverse jet motion, which is on the order of 15.0 degrees. With added vibration, the third stage frequency becomes very distinct in this simulation.

The grid system employed for this Stage I edge tone simulation is illustrated in Figures 4-34 and 4-35.

The density and enthalpy contours, Figures 4-36 and 4-37, illustrate the increased deformation of the jet and flow disruption near the wedge apex. The lift coefficient time history and FFT analysis, Figures 4-38 and 4-39, exhibit the third stage frequency. The numerical predictions for edge tone frequencies and rms amplitudes for this case are given in Table 4-1.

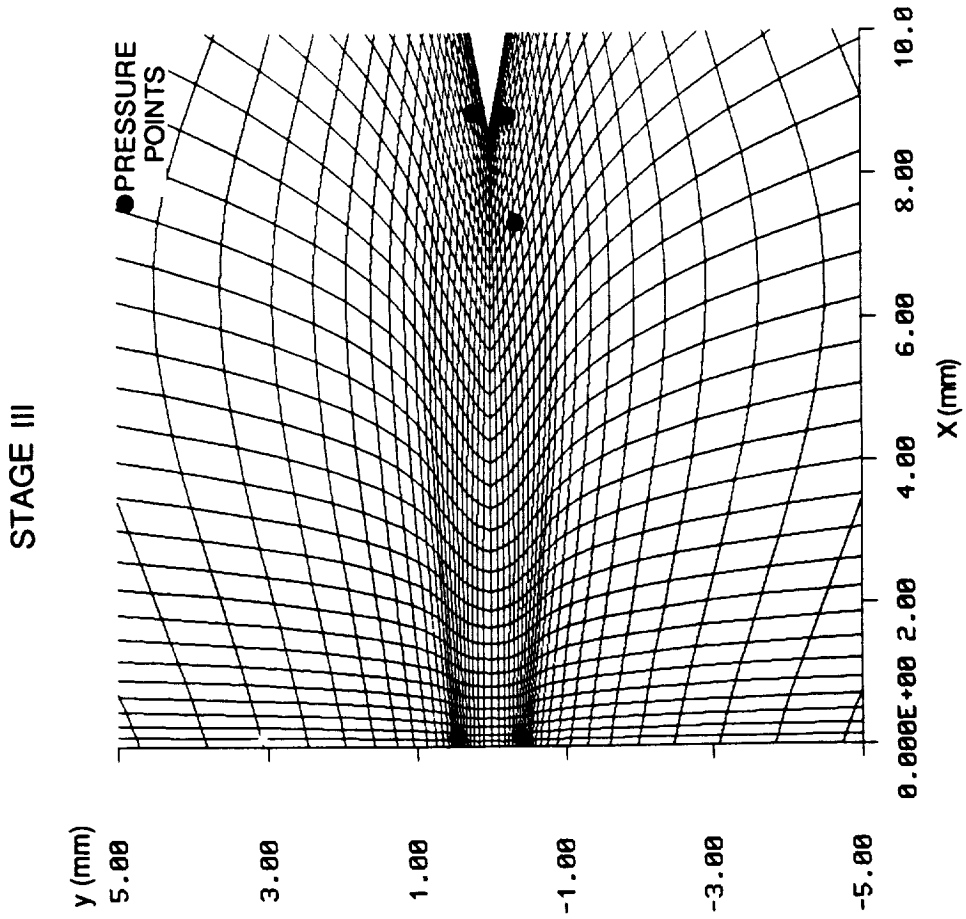


Figure 4-35 Detail A, Computational Grid for Case 5 (0.82 cm)

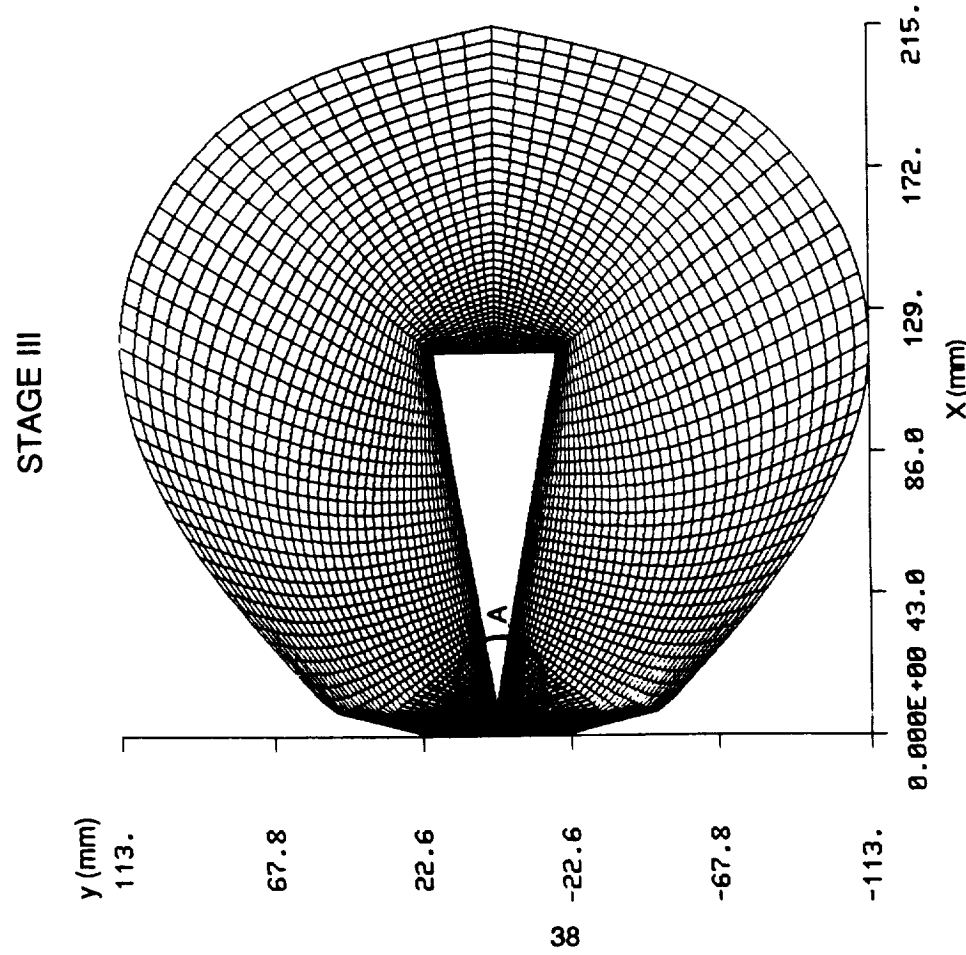


Figure 4-34 Computational Grid for Case 5 (0.82 cm)

STAGE III

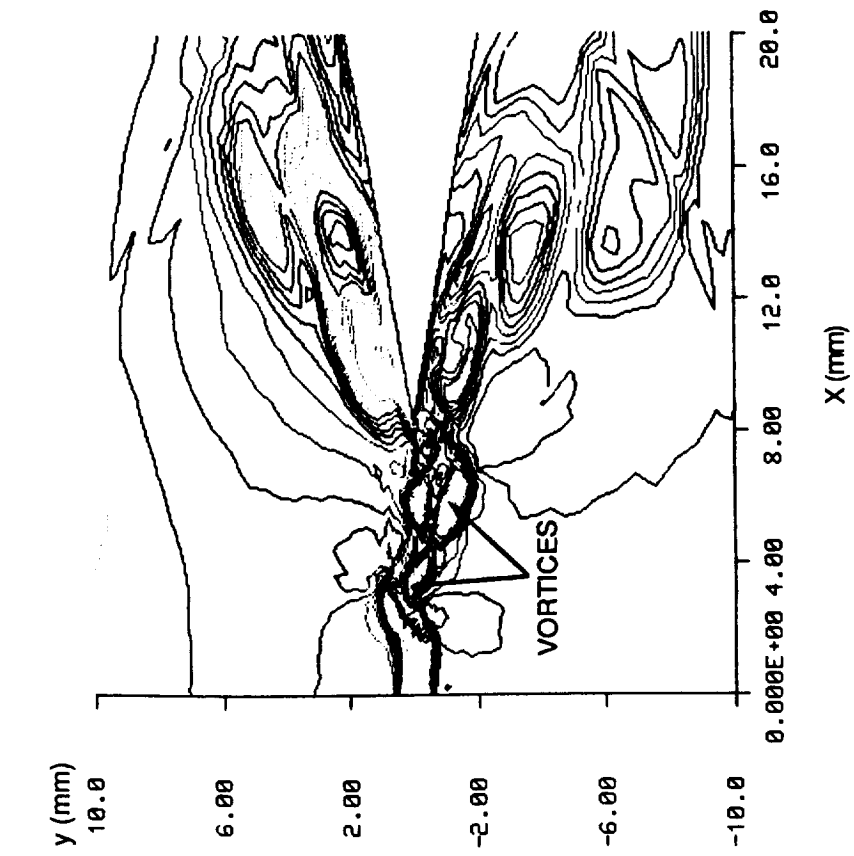


Figure 4-36 Density Contour for Case 5 (0.82 cm)

STAGE III

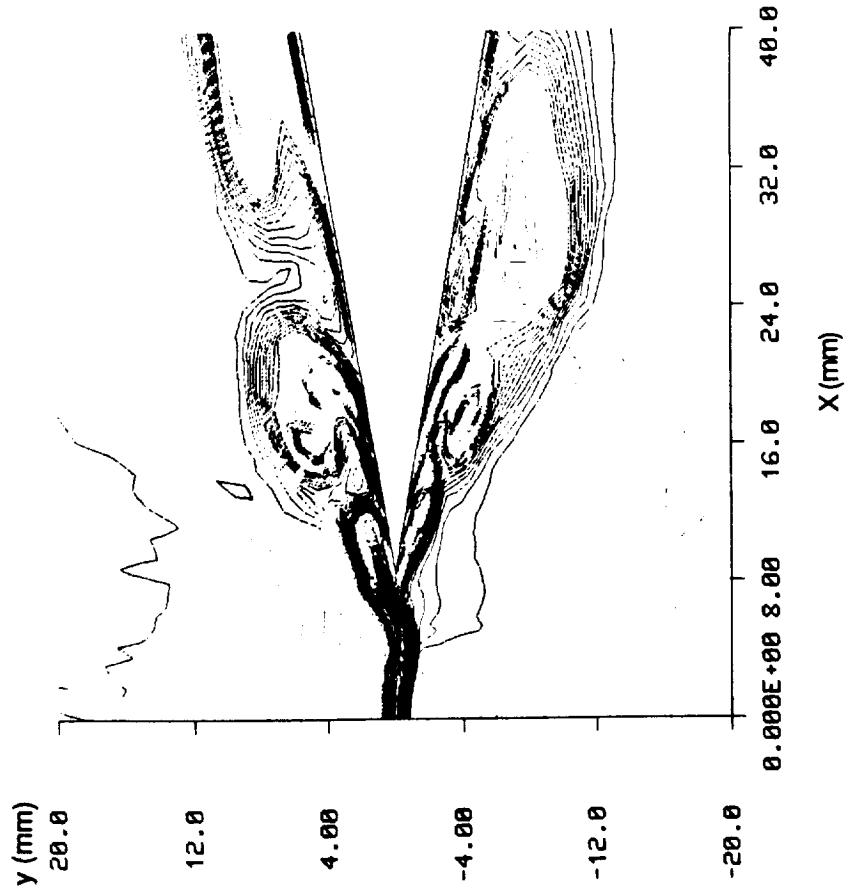


Figure 4-37 Enthalpy Contour for Case 5 (0.82 cm)

STAGE III

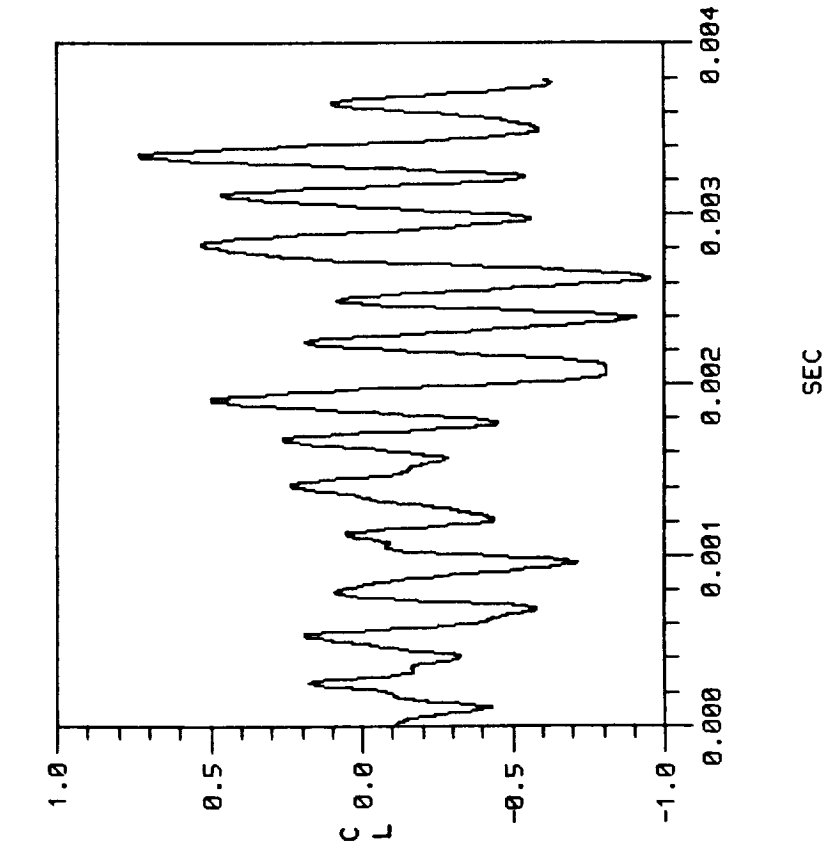


Figure 4-38 Lift Coefficient for Case 5 (0.82 cm)

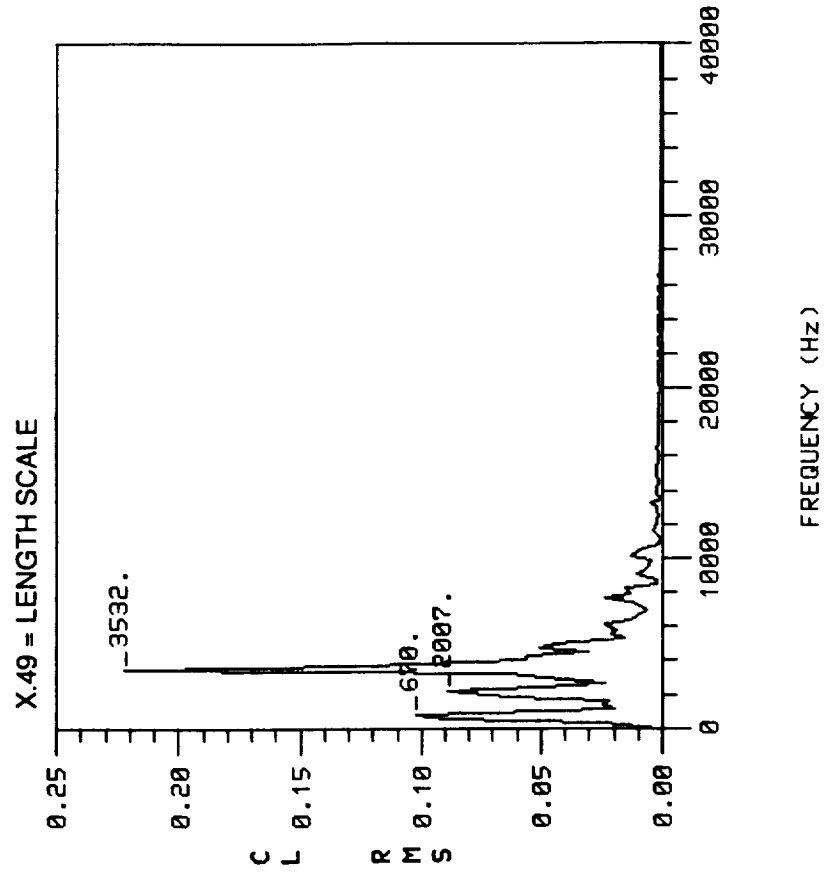


Figure 4-39 Frequency Analysis for Case 5 (0.82 cm)

Stage III Edge tone (0.86 cm)

The vortex-acoustic coupling in the third stage case is much more complicated than in the first two stages. Two parallel cases were run for the Stage III study. A stationary wedge was employed in this second Stage III simulation. In this case, more than one stage was observed, however, the third stage was observed to be rather weak in comparison with the first two stages.

The grid system employed for this Stage III edge tone simulation is illustrated in Figures 4-40 and 4-41. Typical stationary wedge results are shown in Figures 4-42 through 4-45. The density contours and streamlines, Figure 4-43, indicate the formation of vortices. The greater wedge distance in the third stage operation allows more jet pattern variation before interaction with the wedge. The density contours, Figure 4-42, indicate that there are vortex precursors in the jet. In this figure a vortex is shown impinging on one side of the wedge apex. Here the velocity is higher and the pressure lower than the other side of the wedge apex, as may be noted in the velocity contour plot, Figure 4-44. Here, the Mach contours highlight the flow oscillations. The low and high density contours near the wedge apex are consistent with the pressure dipole oscillation. The farfield pressure contours, Figure 4-45, reveal the acoustic wave length of 10.1 cm which agrees well with the predicted Stage III frequency of 3309 Hz.

The lift coefficient time histories and FFT analyses are shown in Figures 4-46 and 4-47. In the frequency response of the lift coefficient, the third stage frequency dominates other frequencies. It was noted that for a point located inside the jet stream, pressure measurement data did not give good third stage predictions. This indicates that the frequency measurement for edge tones should be done in the far field or near the wedge but not inside the jet stream. The frequency predictions for case 6, a stationary wedge, are given in Table 4-1.

STAGE III

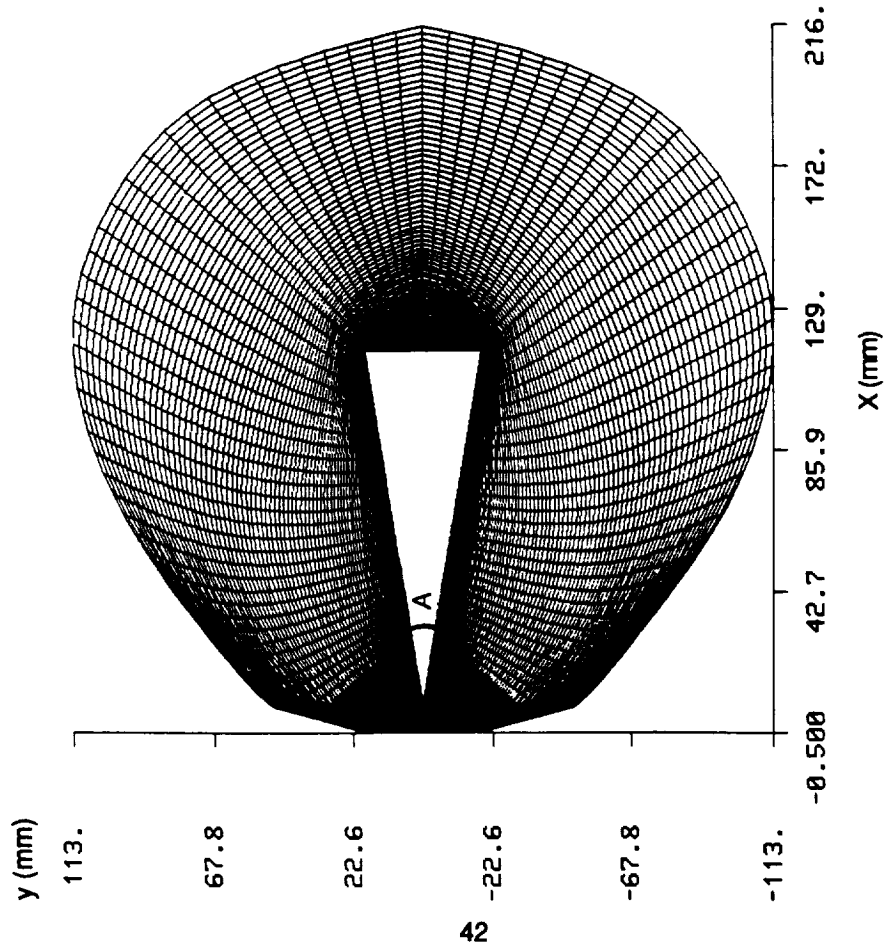


Figure 4-40 Computational Grid for Case 6 (0.86 cm)

STAGE III

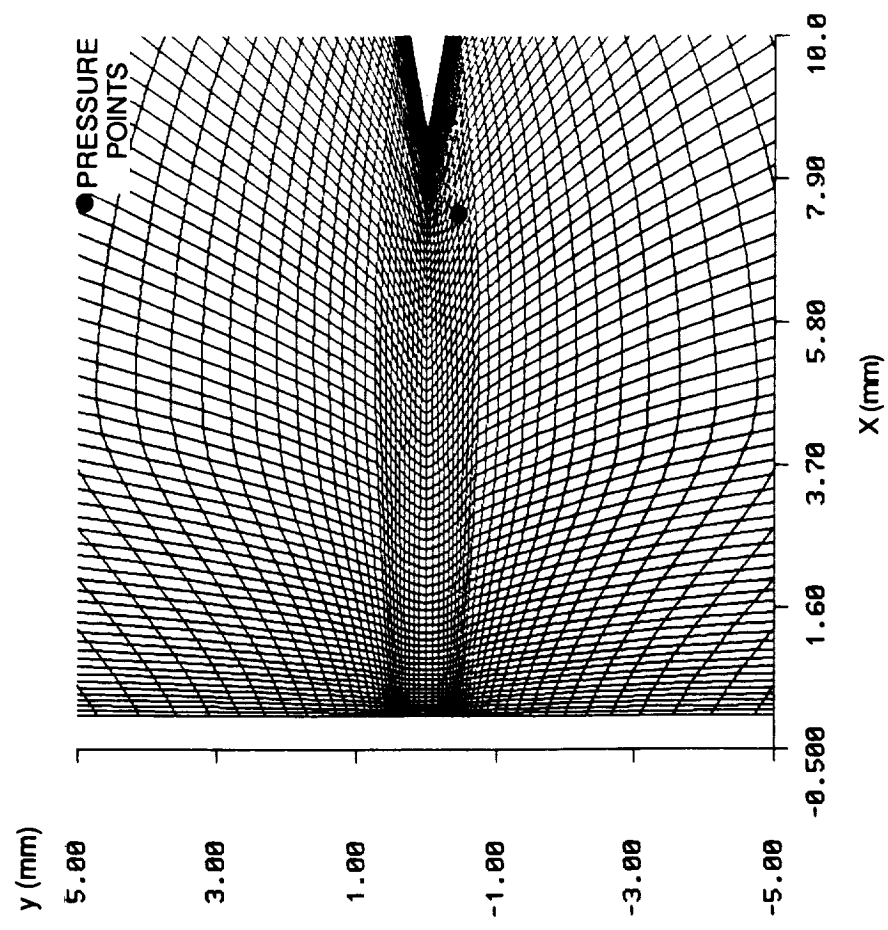


Figure 4-41 Detail A, Jet Wedge System for Case 6 (0.86 cm)

STAGE III

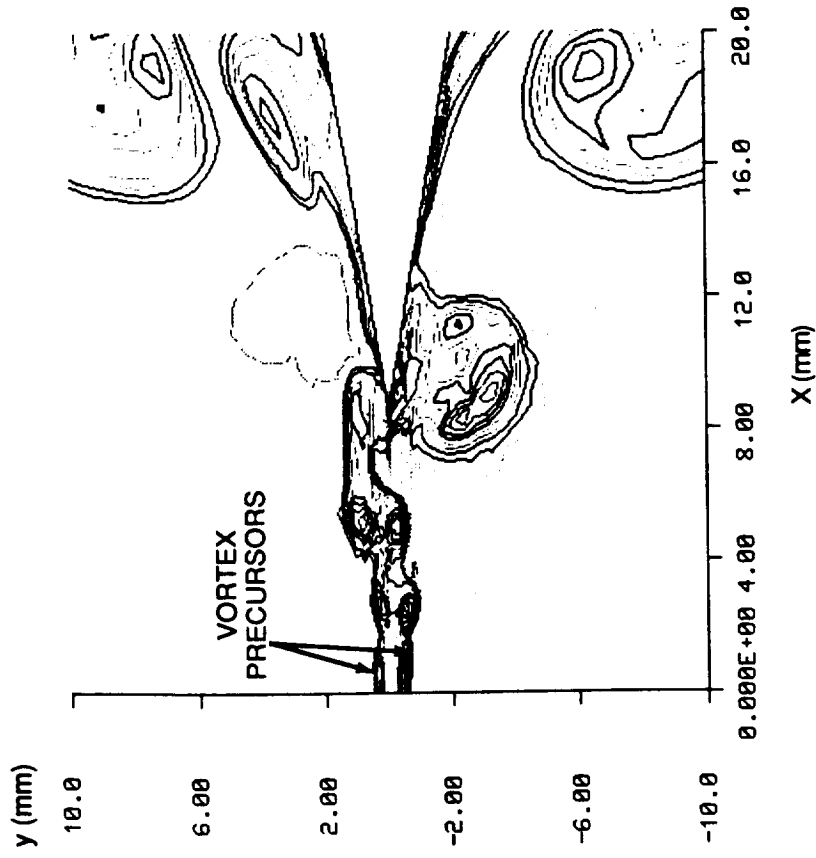


Figure 4-42 Density Contour for Case 6 (0.86 cm)

STAGE III

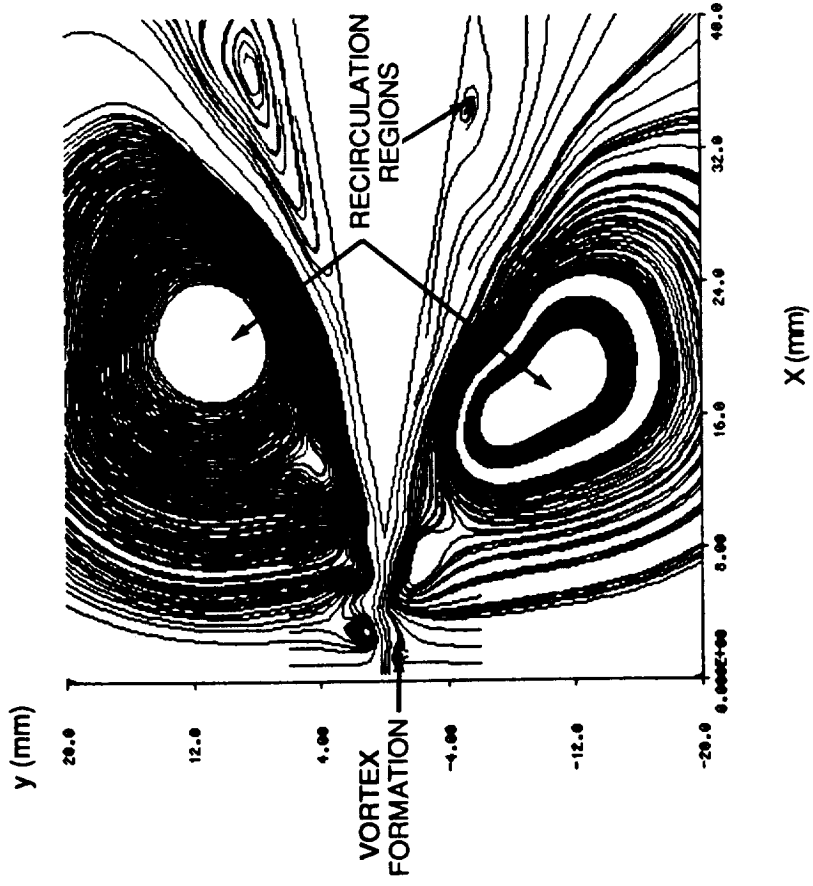


Figure 4-43 Streamlines for Case 6 (0.86 cm)

STAGE III

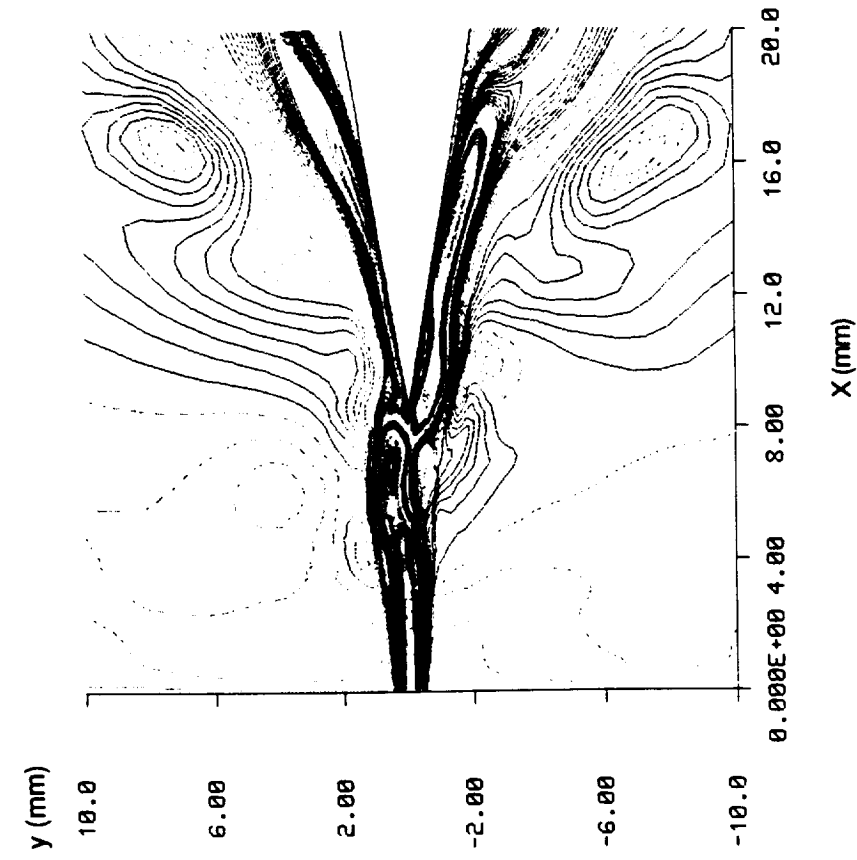


Figure 4-44 Mach Number Contour for Case 6 (0.86 cm)

STAGE III

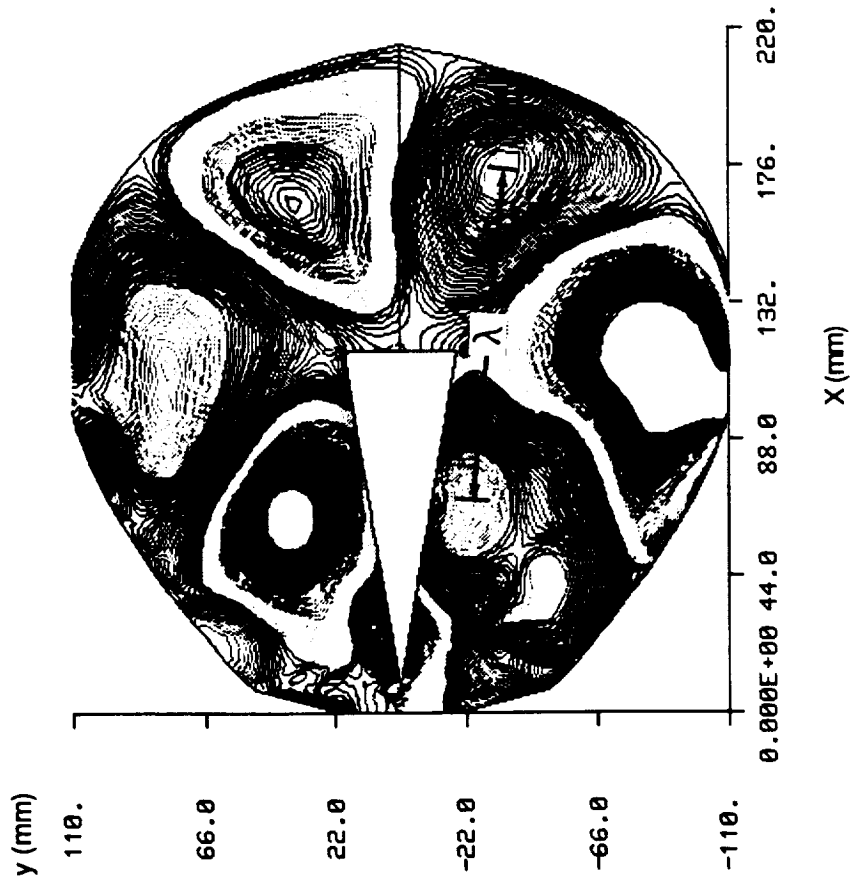


Figure 4-45 Farfield Pressure Contour for Case 6 (0.86 cm)

STAGE III

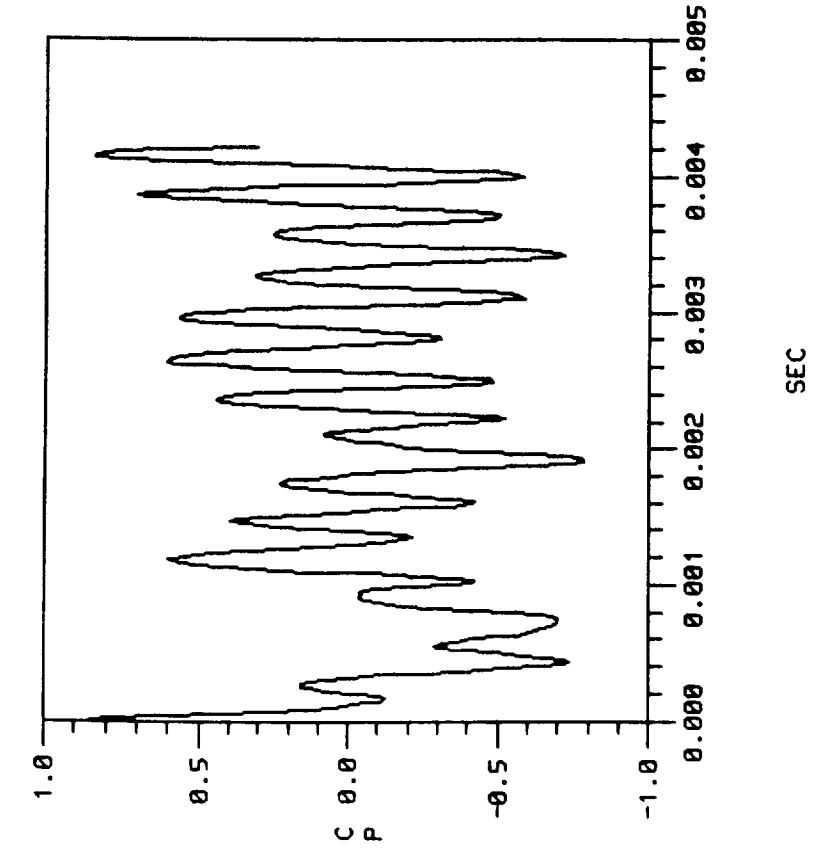


Figure 4-46 Pressure Coefficient Time History for Case 6 (0.86 cm)

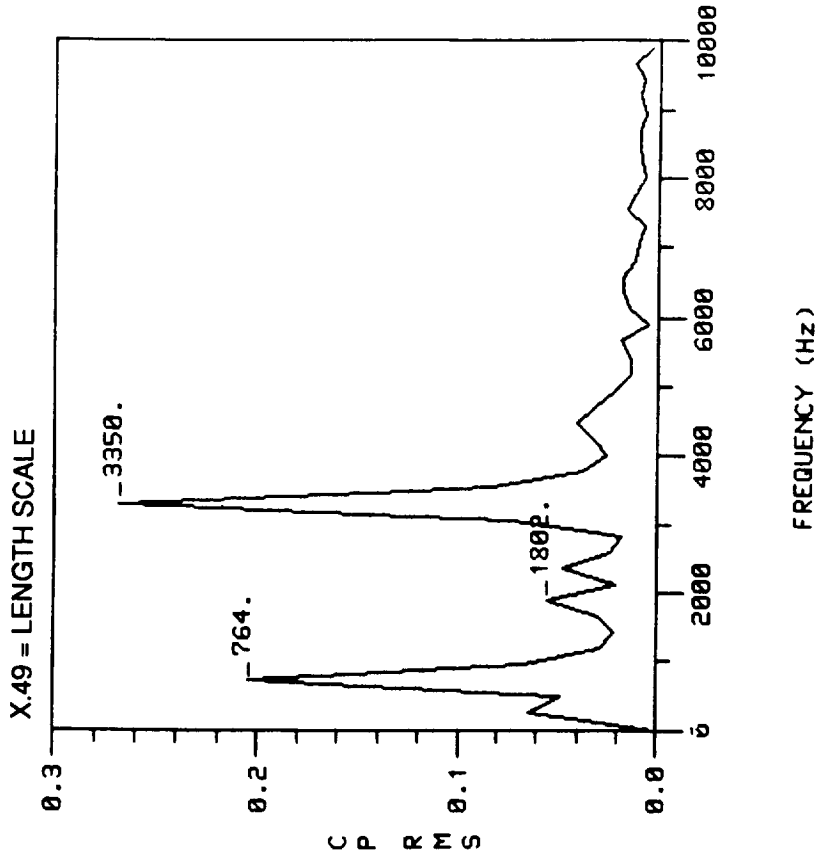


Figure 4-47 Frequency Analysis for Case 6 (0.86 cm)

Stage IV Edge tone (1.6 cm)

The grid system employed for this Stage IV edge tone simulation is illustrated in Figures 4-48 and 4-49. When jet speed decreases as wedge distance increases, the jet is more susceptible to the wedge dipole effects, which deflect the jet and create vortex/undulation centers along the jet boundaries. Consequently, the jet exhibits the extremely dynamic nature of the edge tone flow field near the wedge apex. The near-field density, Figure 4-50 and enthalpy contours, Figure 4-51 bear remarkable resemblance to Brown's smoke picture.

Brown observed that as the edge tone jumps to higher stages, the large recirculation regions on the side of the wedge moved closer to the wedge apex. In the present computation, the large recirculation regions in the Stage IV did move closer to the wedge tip but become a dual vortex pattern as shown in Figure 4-52. This dual vortex pattern was noted only in the Stage IV simulation.

Figure 4-53 shows the time history of the lift coefficient which exhibits the multi-frequency feature of the wedge in this stage. In the FFT frequency spectrum plot, Figure 4-54, the Stage I, Stage III and Stage IV amplitudes are apparent, while the Stage II amplitude is rather weak. This simulation affirms that Stage I oscillations co-exist with each of other stages as reported by Brown.

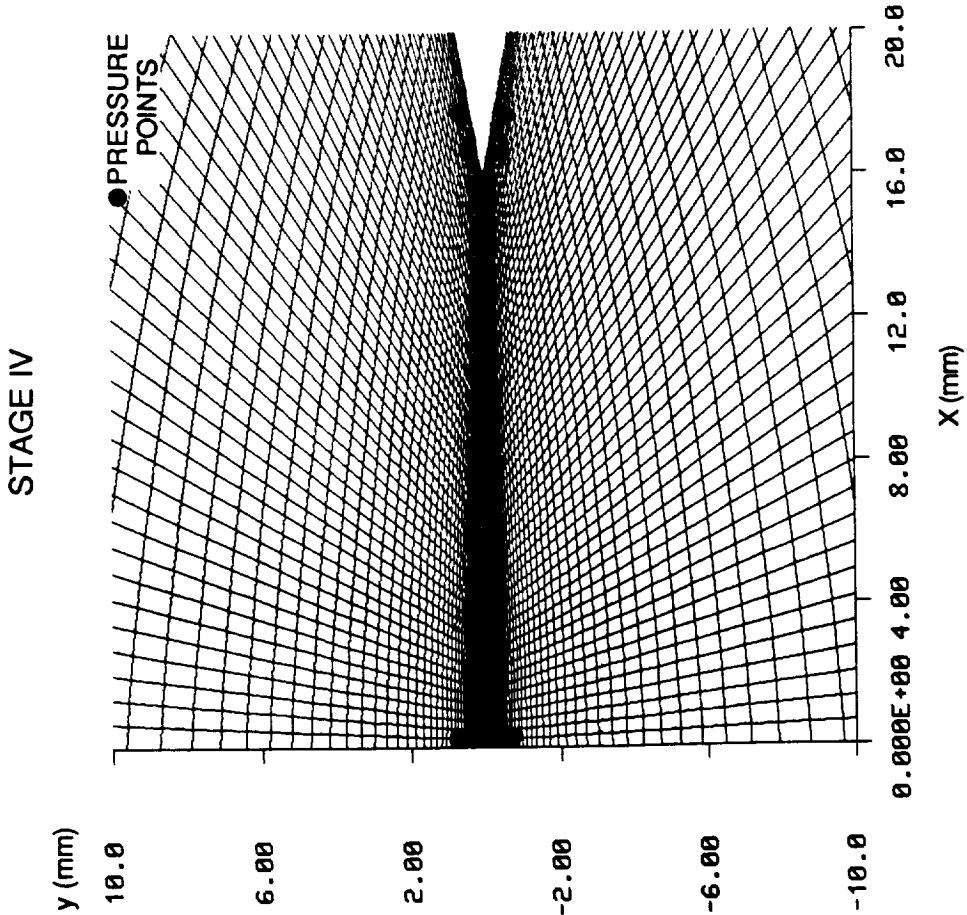


Figure 4-49 Detail A, Jet Wedge System for Case 7 (1.6 cm)

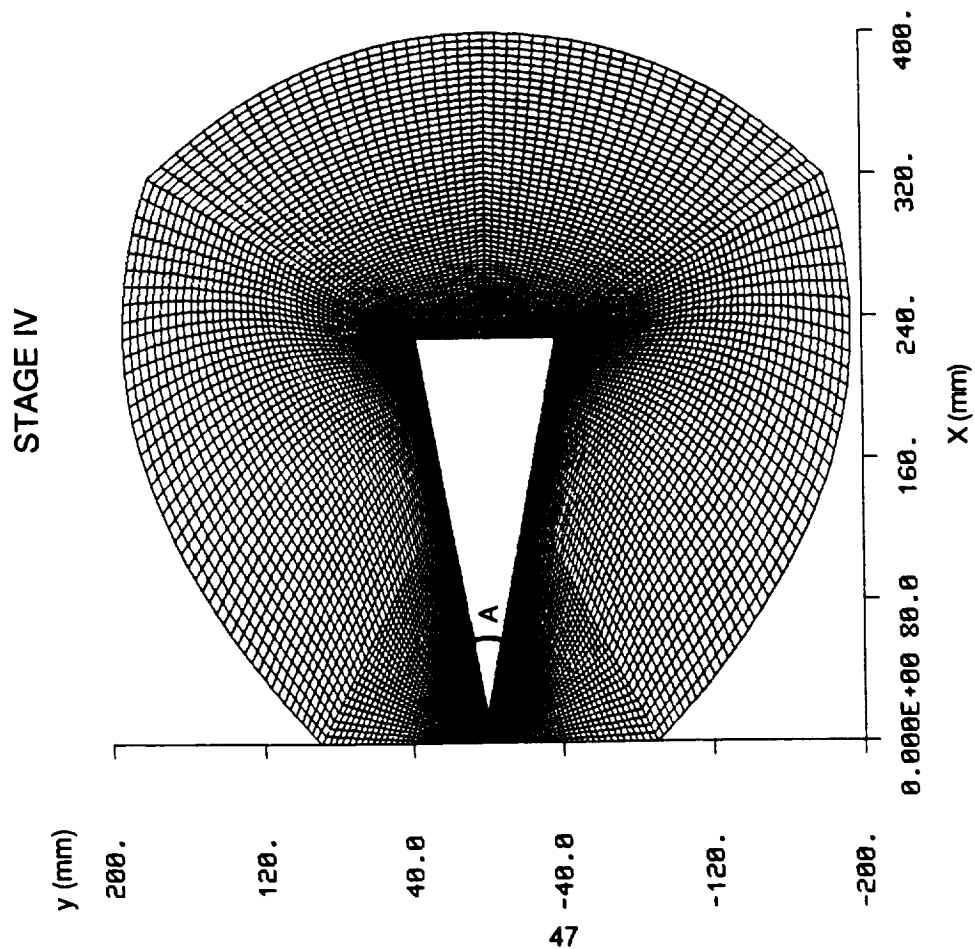


Figure 4-48 Computational Grid for Case 7 (1.6 cm)

STAGE IV

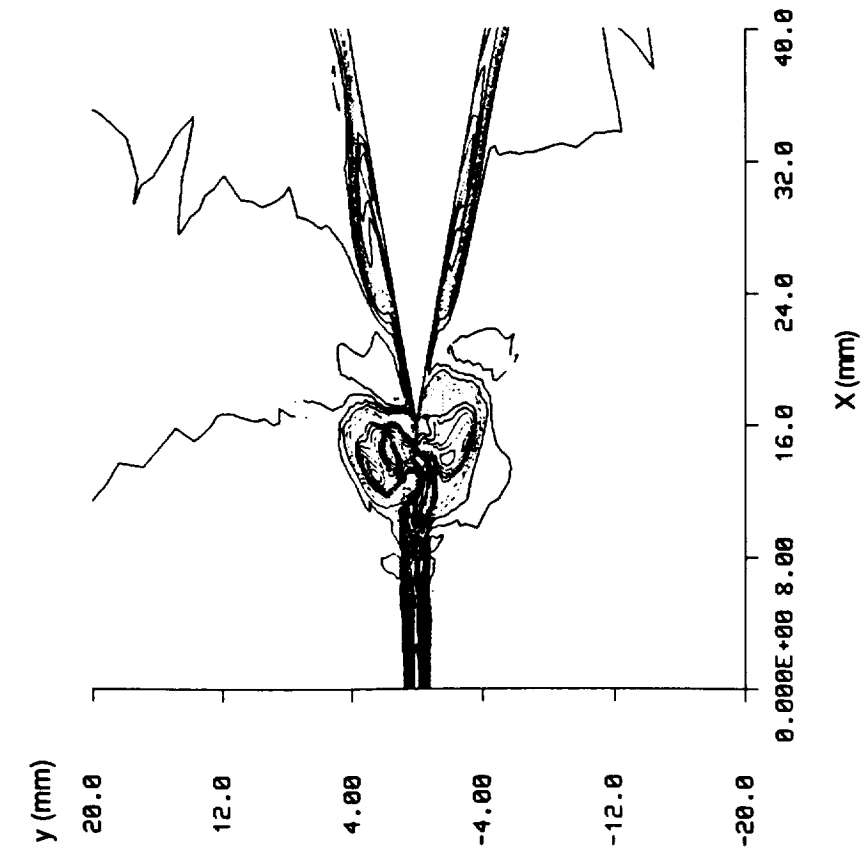


Figure 4-50 Density Contour for Case 7 (1.6 cm)

STAGE IV

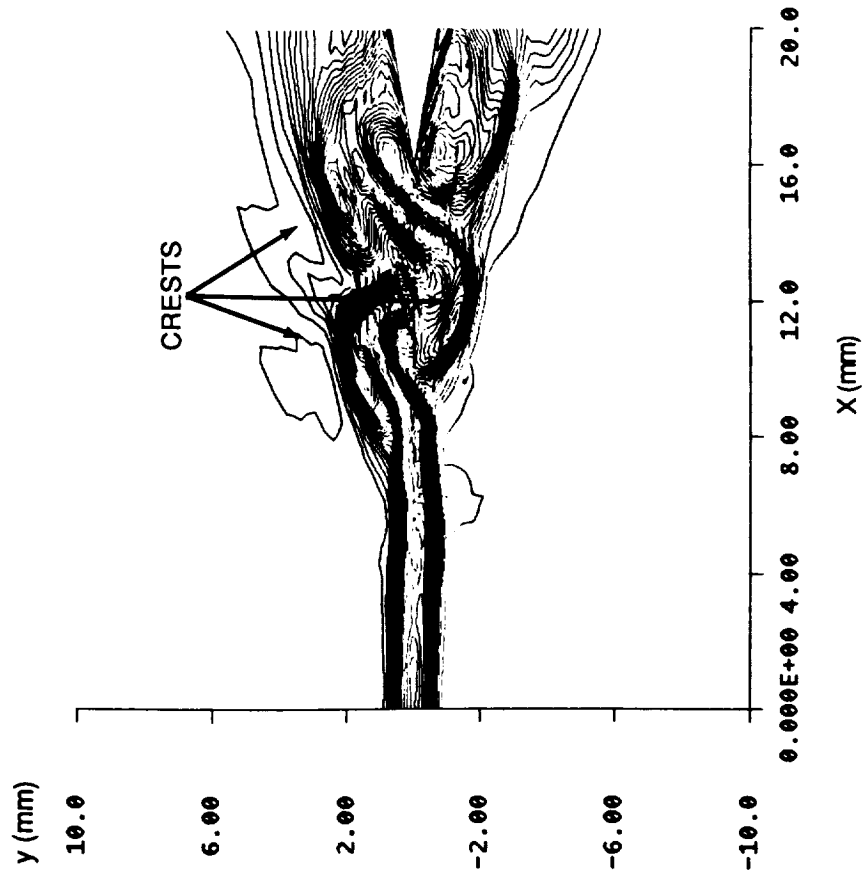


Figure 4-51 Enthalpy Contour for Case 7 (1.6 cm)

STAGE IV

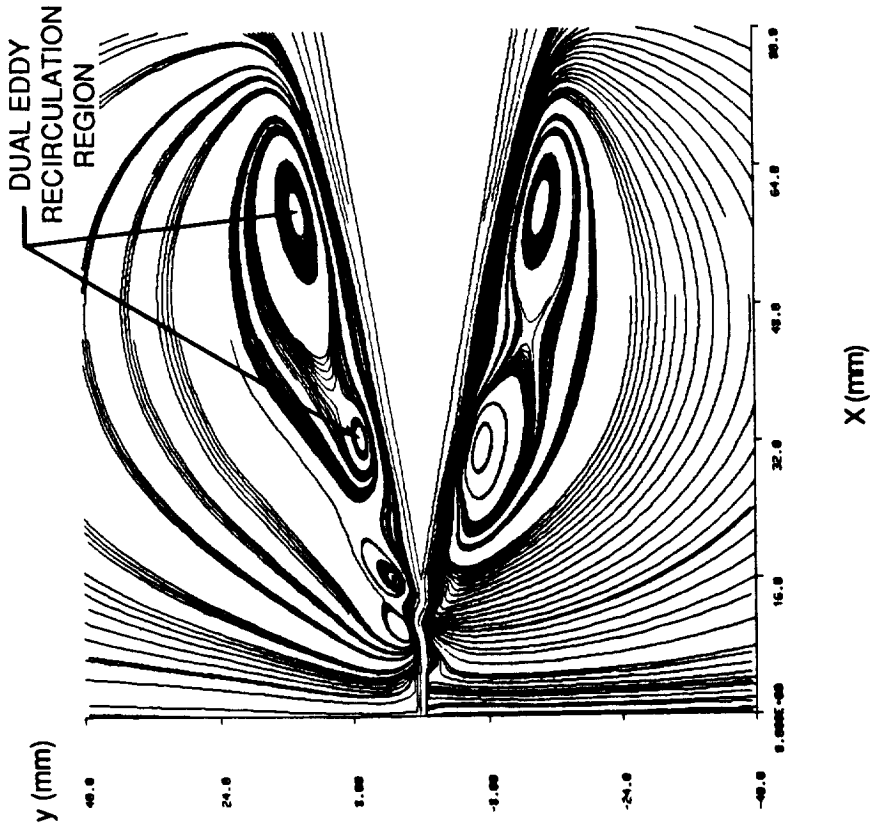


Figure 4-52 Streamlines for Case 7 (1.6 cm)

STAGE IV

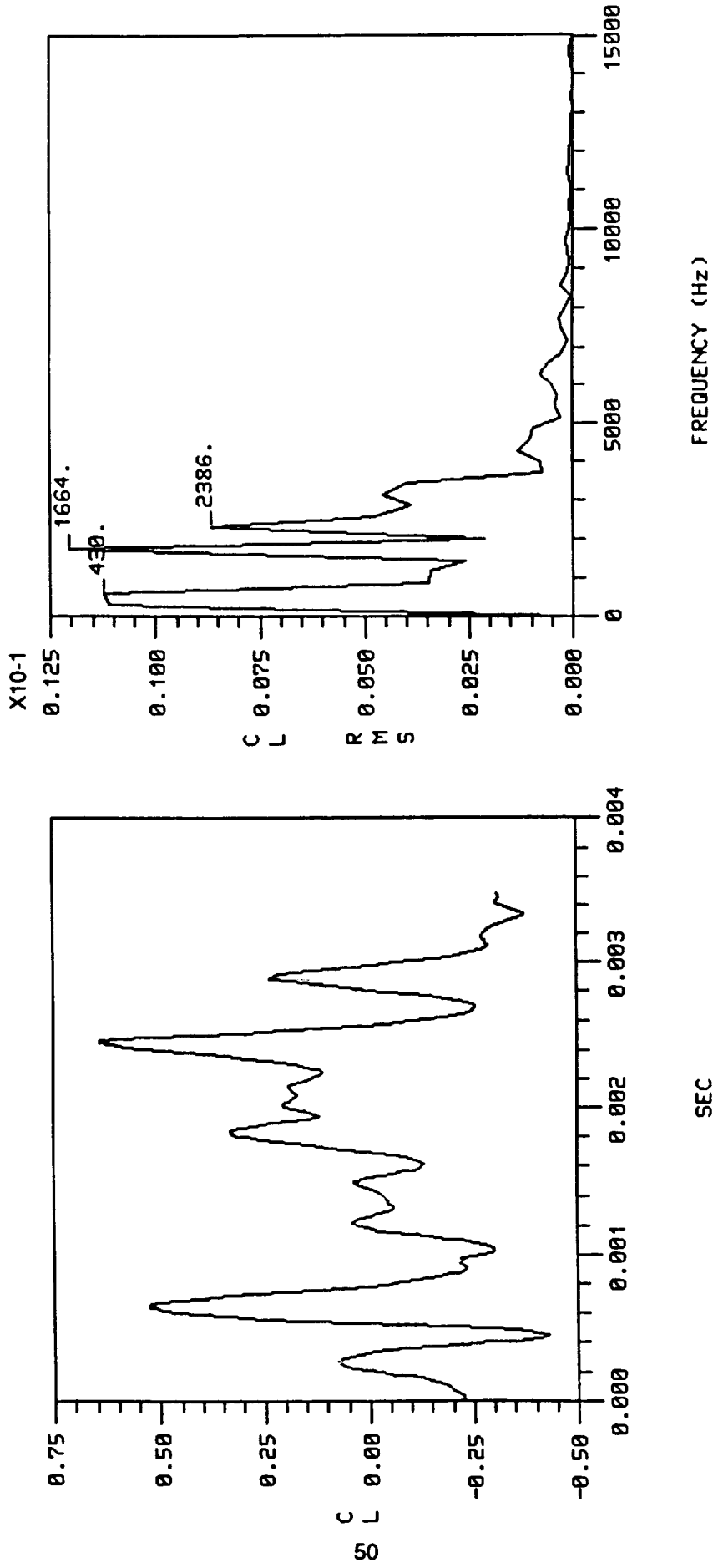


Figure 4-53 Lift Coefficient Time History for Case 7 (1.6 cm)

Figure 4-54 Frequency Analysis for Case 6 (0.86 cm)

Post-Edge Tone (4.0 cm)

According to Brown's experiment, when the distance from the wedge to the orifice is greater than 2.0 cm, the acoustic feedback, with strength decreasing linearly with distance, would be too weak to trigger alternate vortex shedding at the orifice lips. The post-edge tone case was run with a wedge distance of 4.0 cm. Extremely low amplitude flow oscillations in the lift coefficient were observed. Comparatively, the signals in this case are also too weak to be considered edge tone oscillations.

The grid system employed for this post-edge tone simulation is illustrated in Figures 4-55 and 4-56. The Mach number contours, Figure 4-57, and density contours, Figure 4-58, illustrate the observation that the flow remains generally symmetric and the jet-wedge interaction is weak. There is no substantial wedge acoustic dipole induced. The streamline plot, Figure 4-59, illustrates the absence of jet flow undulations.

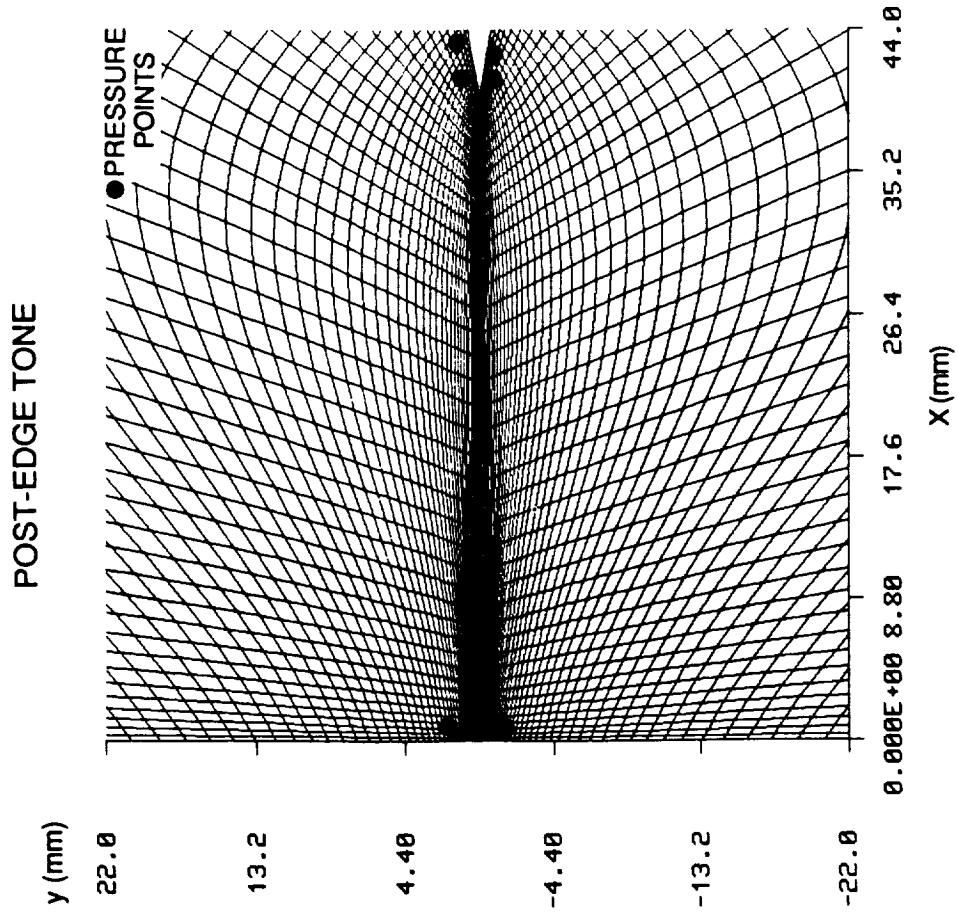


Figure 4-55 Computational Grid for Case 8 (4.0 cm)

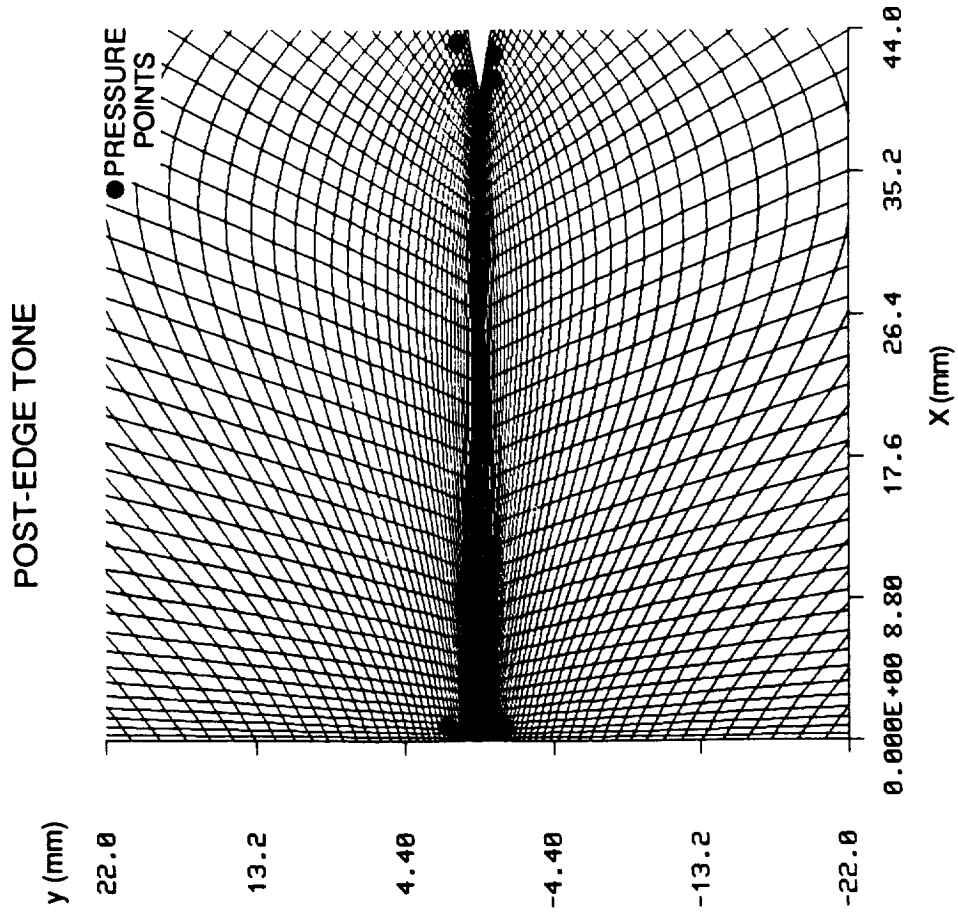


Figure 4-56 Detail A, Jet Wedge System for Case 8 (4.0 cm)

POST-STAGE

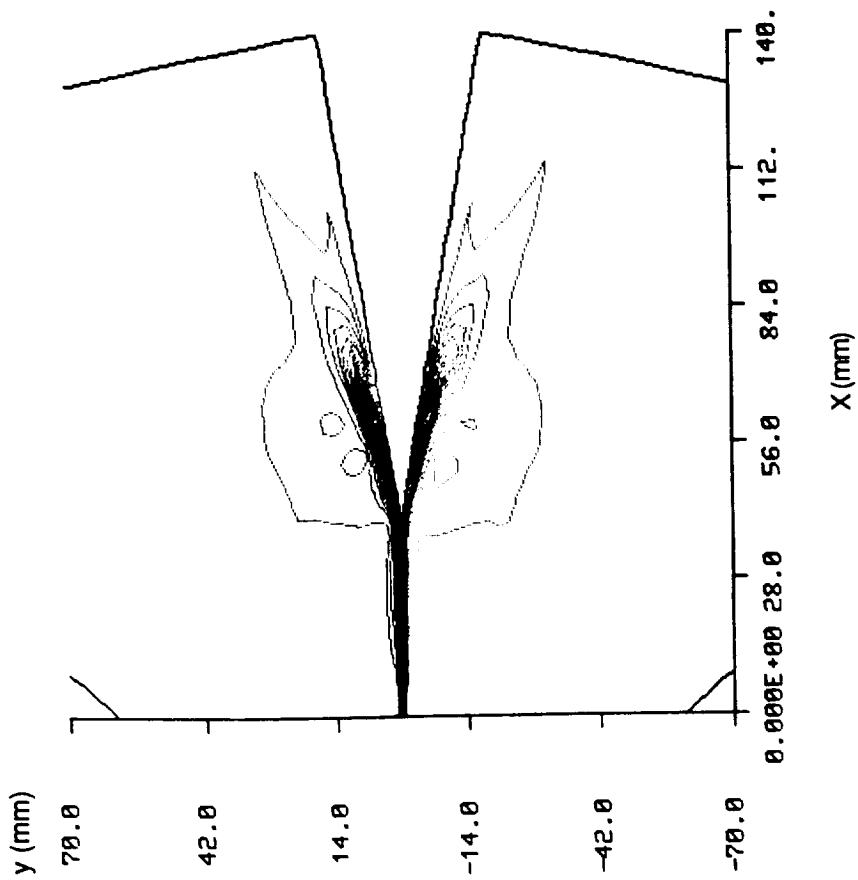


Figure 4-57 Mach Number Contour for Case 8 (4.0 cm)

POST-STAGE

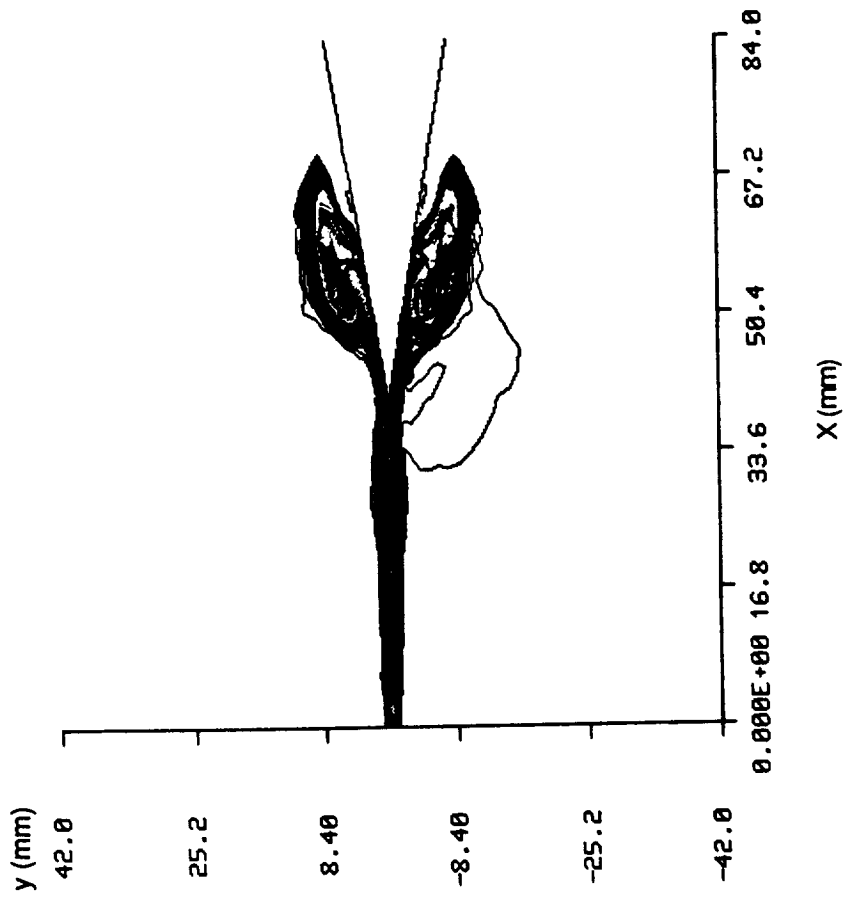


Figure 4-58 Density Contour for Case 8 (4.0 cm)

POST-STAGE

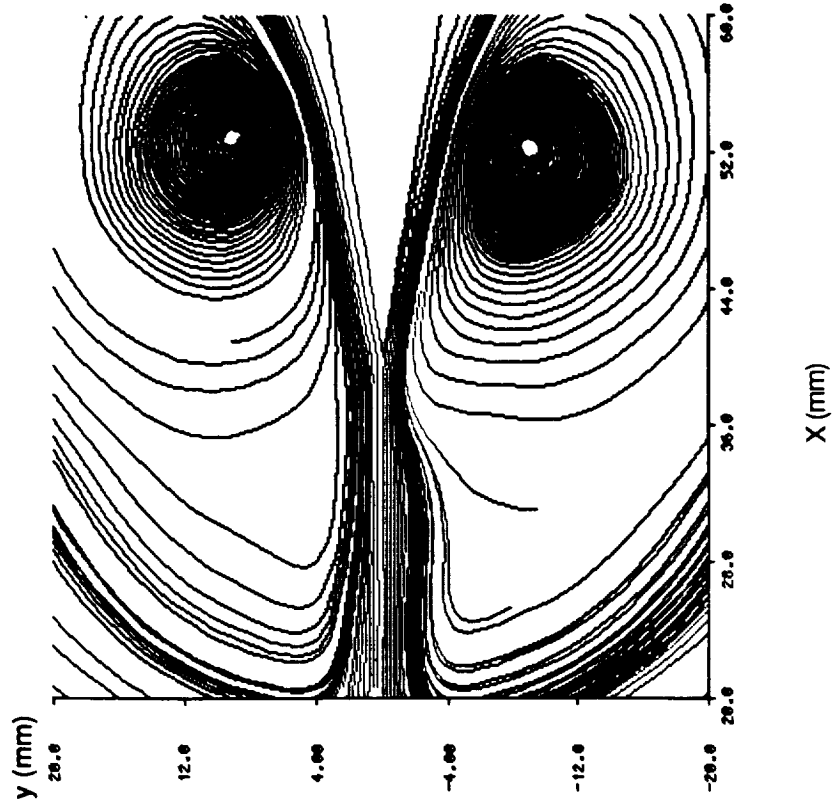


Figure 4-59 Streamlines for Case 8 (4.0 cm)

5.0 Discussion and Interpretation of Results

The ability of the USA CFD code to produce time-accurate solutions in non-steady flows at low speeds has been validated in several studies. Dougherty et. al. ^{25,26}, in two separate papers have used the code to perform time-accurate studies involving vortex shedding from circular cylinders and cavities. The ability of the numerical simulation to capture the acoustic nature of the feedback system in the edge tone was clearly illustrated.

Pressure Differential at the Wedge Apex: the Dipole Nature of the Edge Tone

Pressure, as a function of time, at a point under the wedge apex and at a point over the wedge apex is shown in Figure 5-1, for the Stage I edge tone in Case 3. The difference in these pressures is shown in Figure 5-2. The three extremities of the curve indicate maximum jet impingement on the wedge apex. The two maxima indicate impingement on the lower side of the wedge and the minimum indicates an impingement on the upper side. The sinusoidal shape of the pressure differential indicates that the wedge apex pressure field is nearly a perfect dipole. The period of the pressure generated wave estimated from the figure is 0.52 ms, corresponding to a 1900 Hz frequency

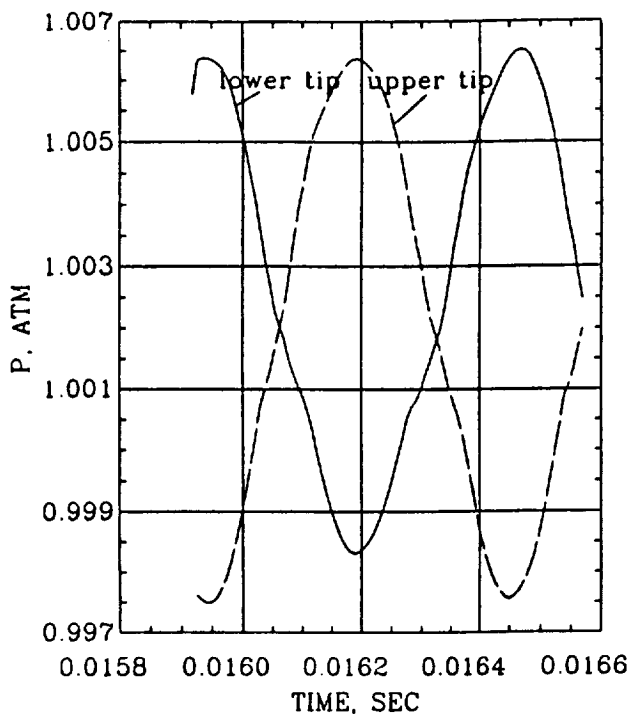


Figure 5-1 Pressure Signals Above and Below the Wedge Apex

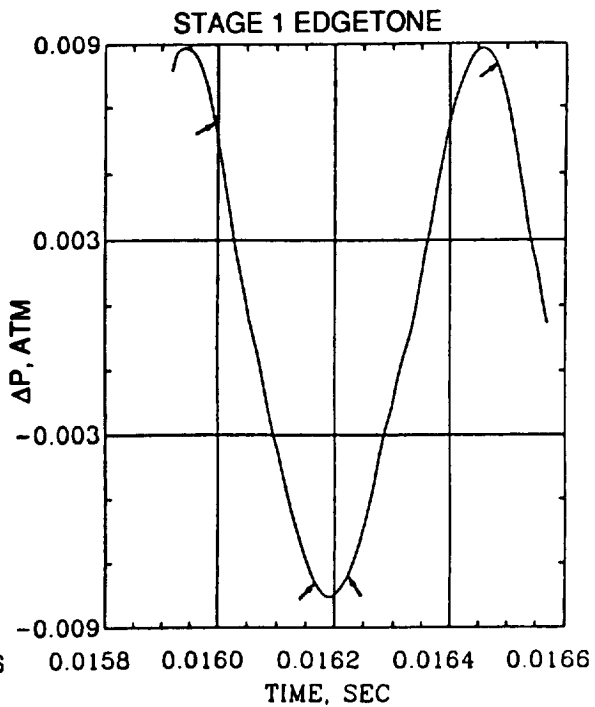


Figure 5-2 Pressure Differential Between Wedge Apex Points

Pressure Differential at the Orifice: Flow Response to the Wedge Dipole

Pressure signals from the orifice corners are shown in Figures 5-3, for the Stage I edge tone of Case 3. These signals have a frequency more than twice that of the wedge apex signals. The difference between these signals is shown in Figure 5-4. The similarity in pressure differential plots between the wedge apex and the orifice implies that these two acoustic elements oscillate at the same frequency and that the orifice must be mainly influenced by the wedge dipole.

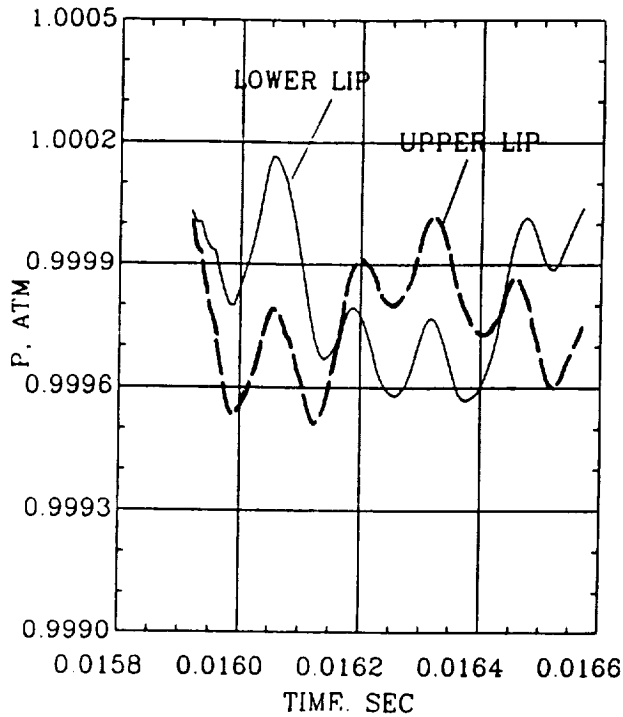


Figure 5-3 Pressure Signals on Top and Bottom of Orifice

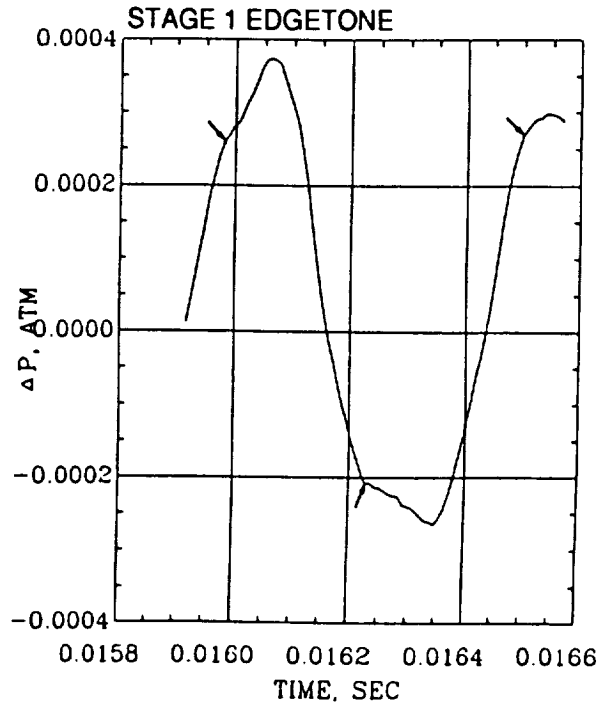


Figure 5-4 Pressure Differential Between Orifice Points

Amplitude Decrease from the Wedge Apex

In addition to direct frequency comparison with Brown's data, pressure amplitudes were obtained using the fine grid system of the 0.40 cm Stage I edgetone Case 3.. When the jet is impulsively started, a compression wave front originates at the orifice. As the front reaches the wedge apex, a strong pressure compression occurs. This compression causes an acoustic emission which propagates outward from the apex at the speed of sound.

Pressure was monitored during the computation at several points in the flow field to study the propagation and amplitude of acoustic emission from the wedge apex. The amplitude obtained from this study is plotted versus transverse distance, y , in Figure 5-5. Points which were close to the wedge apex had higher amplitude which dropped exponentially with ' y ' in the near-field. The distance between points "a" and "b" is 0.856 cm and the time delay between peaks for point "a" and point "b" is 0.025 ms. This implies a propagation speed of 34200 cm/sec, which agrees well with the speed of sound at room temperature used in these simulations.

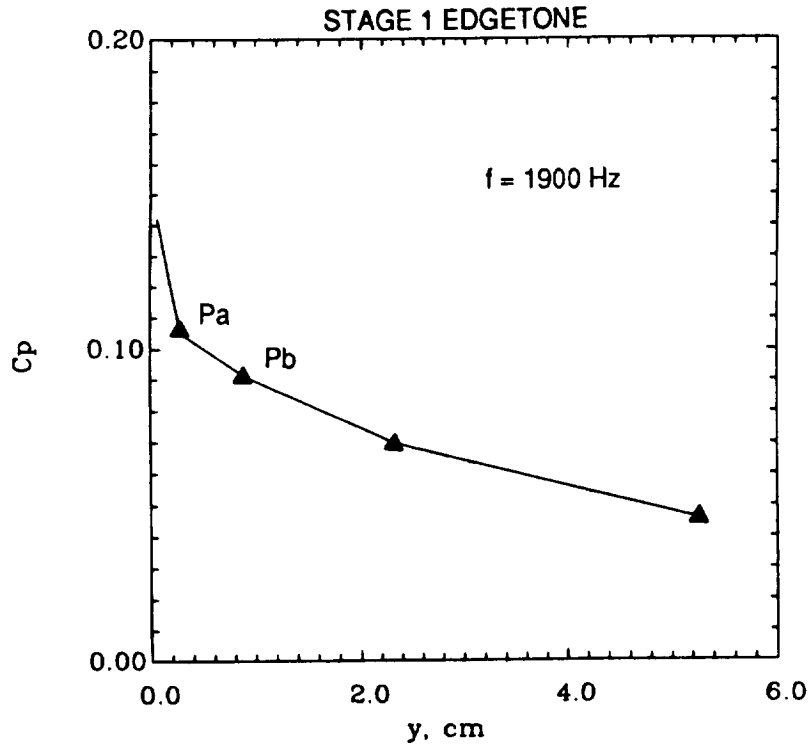


Figure 5-5 Pressure Coefficient versus Distance from Wedge Apex

Pressure Differential Between the Wedge Tip and the Orifice

Figure 5.6 shows the C_p difference across wedge, dashed line, and the C_p difference between orifice lips, solid line, magnified x50 to compare waveform with that at the wedge. The differential pressure pulses at both the wedge and slit have the same frequency but are shifted in phase. The pressure waveforms are from Case 4 for the Stage II edge tone at $h=0.56$ cm and illustrate the fact that the slit pressure is strongly related to the wedge pressure. The alternating pressure extremes at the wedge apex are generated by the acoustic dipole pressure source. As an acoustic point source, the signal originating from the wedge decreases by a factor of 50 at the orifice.

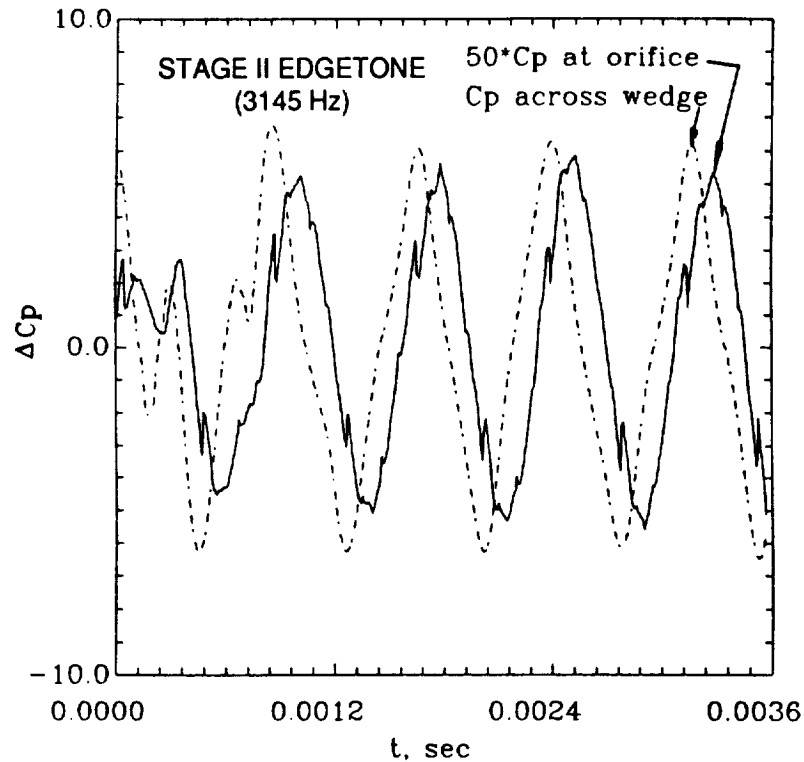


Figure 5.6 Pressure Differentials at the Wedge and Orifice

Formation, Growth, Transport and Dissipation of Vortices

Having reached a steady tone producing state, the change in orifice pressure needed for the formation of a new vortex is propagated from the wedge apex by an acoustic wave. The associated time delay is the time duration required by the sound wave to travel from the wedge apex back to the orifice. The period of the wedge oscillation is therefore the sum of time durations required by a vortex to travel from the orifice to the wedge and by the sound wave to travel from the wedge back to the orifice to trigger the formation of a new vortex.

The formation, growth, transport, and dissipation of vortices can be highlighted through a sequence of streamline plots. Figures 5-7, shows a set of four streamline diagrams for Case 3, the 0.33 cm Stage I edge tone. As shown in the figures, a vortex above the right-bound jet is counter-clockwise (CCW) and one below it is clock-wise (CW) due to their relative locations with respect to the jet. Initially, in Figure 5-7a, the CW vortex under the jet pushes the flow toward the lower side of the wedge apex and the CCW vortex above the wedge pulls the flow away from the upper side of the wedge apex. This jet motion causes the flow to impinge at the lower side of the wedge apex. Consequently, a high pressure center builds up at the lower side of the wedge apex. The sense of the pressure dipole is pointed upwards. An acoustic wave from the pressure dipole has propagated outwards and specifically causes a low pressure center and a new vortex to appear at the upper corner of the orifice.

The vortex-acoustic coupling is further clarified in the following. Initially at $t=0$, the dipole configuration is such that the pressure at the upper side of the wedge apex is at a minimum and the lower side of the wedge apex at a maximum. The acoustic feedback causes the pressure field at the orifice to have the same sense, that is, high at the lower lip and low in the upper lip of the orifice as it lags only slightly in phase. Since the velocity gradients at the lips are high, vortices quickly form at the orifice lips when the pressure distribution changes. The pressure force causes the flow at the upper lip to bend up. Eventually, the resultant roll-up movement develops into a new vortex.

This new CCW vortex gains energy from the jet and moves downstream, initially at approximately 46 percent of the jet speed. At this moment, in Figure 5-7b, a CW vortex rolls under the wedge and causes a high speed and low pressure region at the lower side of the wedge. This changed influence of the pressure differential across the wedge apex will soon be felt at the corners of the orifice. The pressure field at the orifice will be low at the lower corner and high at the upper corner according to the sense of the dipole pressure at the wedge apex.

In Figure 5-7c, a new vortex has just appeared at the lower corner of the orifice. There is approximately 180 degree phase shift between the diagrams 5-7a and 5-7b.

Figure 5-7d shows the approach of the CW vortex, under the jet, to the wedge and the CCW vortex rolling above the wedge. The direction of the pressure dipole now becomes upwards as in the first diagram 5-7a. The pressure wave propagates upstream and causes a low pressure center at the upper corner of the orifice to form. The low pressure center is evident with the initial curl-up of the flow line at the upper corner of the orifice as shown in the last diagram 5-7d. A new vortex will soon emerge, located at the upper corner of the orifice. This completes an edge tone production cycle.

CASE 3, STAGE I EDGE TONE AT $h = 0.33$ cm

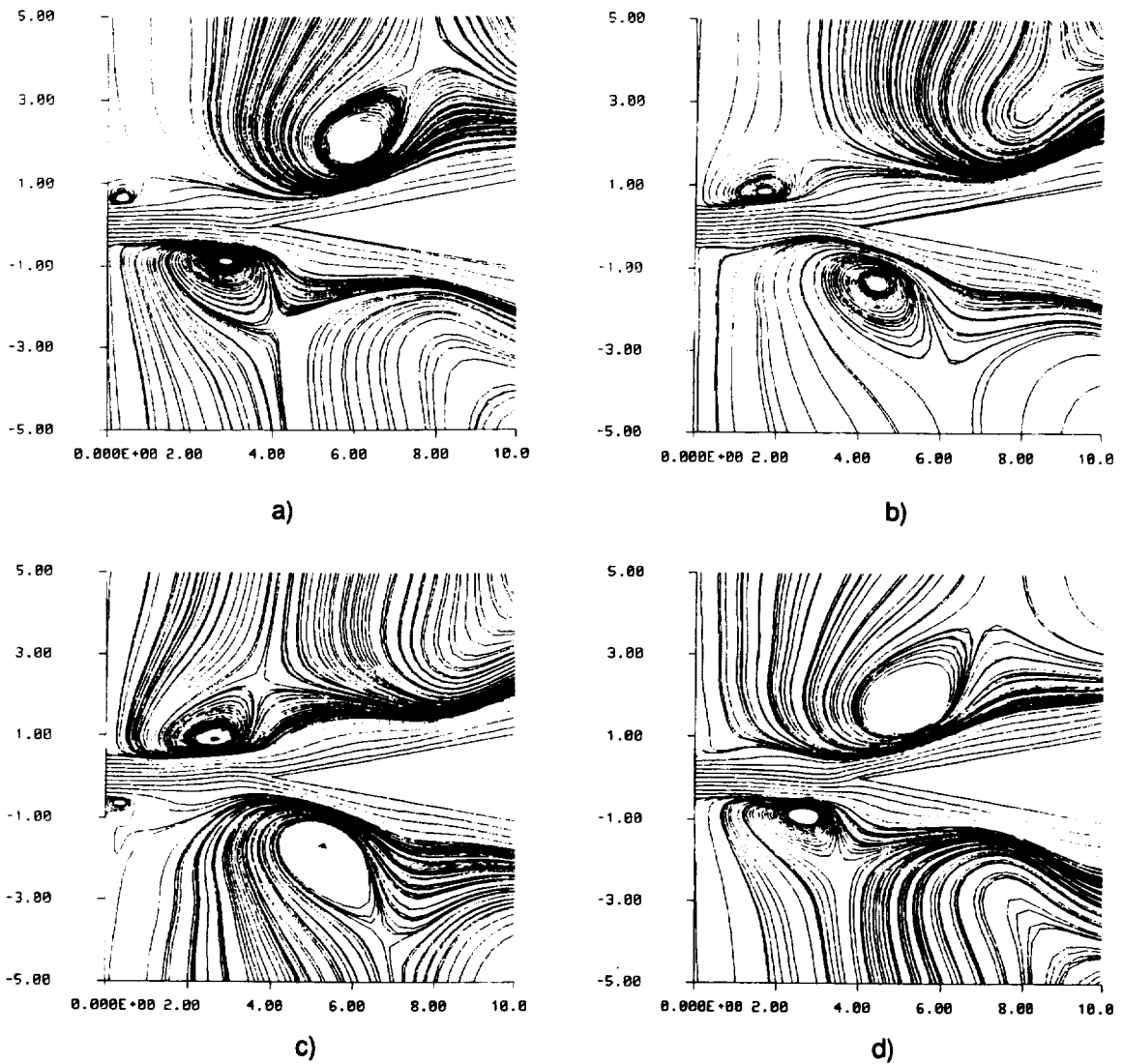


Figure 5-7 Time Sequence of Streamlines showing Vortex Formation for Stage I Edge Tone Growth and Dissipation

Vortex Shedding Flow Patterns

Each stage presents a unique vortex shedding flow pattern as illustrated in the density contours shown in Figures 5-8a through 5-8d. Figures 5-8a through 5-8d, illustrate the strong bending of the jet in the higher stages. The most prominent features of each diagram are the large eddies to either side of the wedge.



Figure 5-8. Vortex Flow Patterns of Edge Tone Stages

Farfield Acoustic Wave Patterns

As each case progressed in time, a farfield acoustic pattern began to emerge. Peaks and valleys in farfield pressure data yielded significant information on the dominant frequency being emitted from the edge tone. Notably, the distance between the compression ridges in the farfield data corresponded to the wavelength expected for each particular stage frequency. In each of the cases, Figures 5-9a through 5-9d, a representative distance between two compression peaks is marked and labeled. For example, the distance measured between the two peaks labeled in the Stage III case, Figure 5-9c, is approximately 10.1 cm. Assuming this is an acoustic phenomenon, a frequency of 3438 Hz is obtained, which is in good agreement with the Case 5 Stage III edge tone frequency obtained from the frequency analysis of the time dependent pressure fluctuations in the jet region.

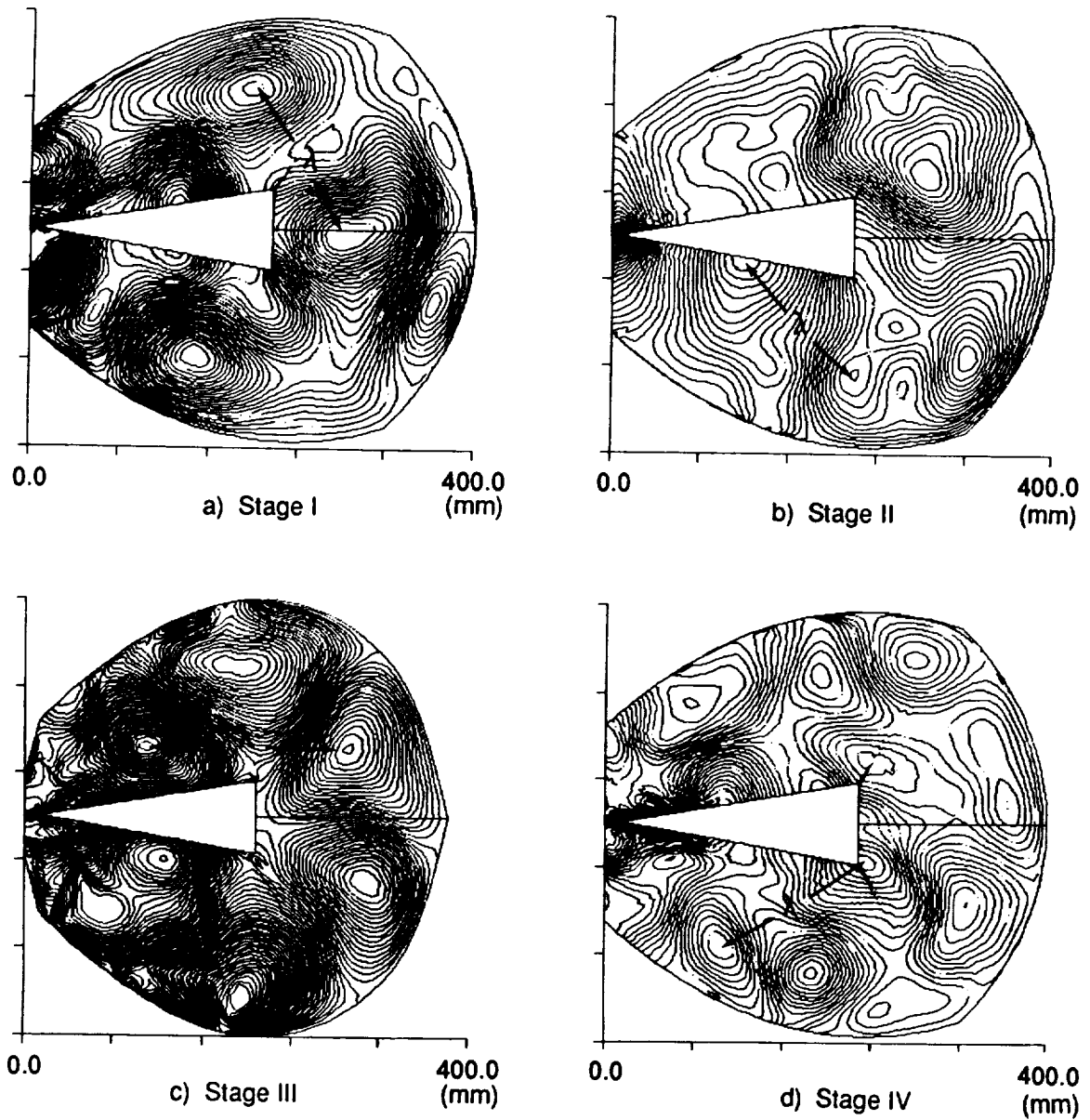


Figure 5-9 Farfield Acoustic Wave Patterns of Edge Tone Stages

Farfield Sound Pressure Levels

An estimate of the sound pressure level at a farfield point, 200.0 cm from the wedge apex, was also obtained for each case, Table 5-1. The sound pressure levels are defined by the relation:

$$SPL = 20.0 \cdot \log_{10} \left(\frac{P_{rms}}{P_{ref}} \right)$$

where $P_{ref} = 2 \times 10^{-5} \text{ N/M}^2$ is the reference sound pressure.

Table 5-1 Maximum Sound Pressure Levels at 200.0 cm from the Wedge Apex

| CASE | - DISTANCE cm | SOUND PRESSURE LEVEL dB (Ref. $2 \times 10^{-5} \text{ N/M}^2$) | PREDOMINANT STAGE |
|------|------------------|---|----------------------|
| 2 | 0.33 | 96.59 | I |
| 3 | 0.40 | 80.81 | I |
| 4 | 0.56 | 100.60 | I |
| 5* | 0.82 | 112.00 | III |
| 7 | 1.60 | 89.32 | III |

* SMALL WEDGE VIBRATION INDUCED AT STAGE III FREQUENCY

Density Pulsations in the Channel to the Orifice

It was also noted that the disturbances in the flow are evident in density plots of the jet. Of the more interesting features of the flow observed were the low density regions traveling downstream in the channel leading to the orifice. These were evident before visible signs of vorticity were present. Brown also noted the alternate freeing and checking of the stream causes a pulsation in the air supply. In the density contour plot, Figure 5-10, pulsations, in the channel leading to the orifice, corresponding to these disturbances observed by Brown are evident.

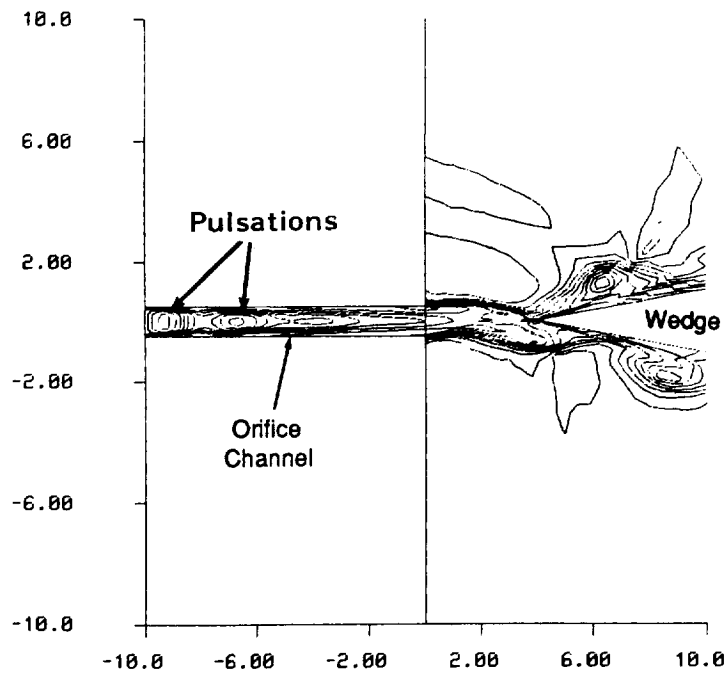


Figure 5-10 Density Pulsations in the Channel to the Orifice

Appendix A - Acoustic Point Sources²⁷

Monopoles

For monopoles, the pressure measurement at a point of distance, r , from the source at time t in a homogeneous fluid of density, ρ , is calculated by:

$$p_{\text{monopole}}(t) = -i k^2 S_{\omega} \left(\frac{\rho c_s}{4\pi r} \right) \cos\theta \left(1 + \frac{i}{kr} \right) e^{ik(r-c_s t)}$$

where $k = \frac{\omega}{c_s} = \frac{2\pi}{\lambda}$, ω is the angular velocity measured in radians per unit time, λ is the wavelength, c_s is the speed of sound in the medium, and r the radius vector to the point of measurement.

The intensity of radiation at the point of distance r from the source is given by:

$$I_{\text{monopole}} = \rho c_s \left(\frac{1}{2\lambda r} \right) |S_{\omega}|^2 = \left| \frac{p}{\rho c_s} \right|^2$$

and the total radiated power:

$$\Pi_{\text{monopole}} = \frac{\rho \omega^2}{4\pi c_s} |S_{\omega}|^2.$$

Dipoles

Dipole sources are highly directional in the near field due to the direction and separation of the two opposing sources. The strength of the dipole source is distributed between the two sources, one element of the dipole strength is at d^+ and the other at d^- , where D_{ω} , the vector dipole strength, is the sum of the source strengths of each element times the vector distance between them. For dipoles, the pressure measurement at a point r from the source at time t in a homogeneous fluid of density, ρ , is calculated by:

$$p_{\text{dipole}}(t) = -k^2 D_{\omega} \left(\frac{\rho c_s}{4\pi r} \right) \cos\theta \left(1 + \frac{i}{kr} \right) e^{ikr - i\omega t}$$

where $k = \frac{\omega}{c_s} = \frac{2\pi}{\lambda}$, ω is the angular velocity measured in radians per unit time, λ is the wavelength, θ is the angle to the acoustic source axis, c_s is the speed of sound in the medium, and, r is the radius vector to the point of measurement.

The intensity of radiation at the point of distance r from the source is given by:

$$I_{\text{dipole}} = \rho c_s \left(\frac{k^2 |D_{\omega}|^2}{4\pi r} \right) \cos^2\theta,$$

and the total radiated power:

$$\Pi_{\text{dipole}} = \frac{\rho \omega^4}{12\pi c_s^3} |D_{\omega}|^2.$$

References

1. Brown, G. B., "*The Vortex Motion Causing Edge Tones*," Proc. Physical Society (London), vol. 49, pp. 493-507, 1937.
2. Beranek, Leo L., "*Noise and Vibration Control*," Institute of Noise Control Engineering (Washington, DC), 1988.
3. Chanaud, R. C., "*Aerodynamic Whistles*," Scientific American, pp. 40-46, June 1970.
4. Sondhaus, C., Ann Physik (Leipzig), Vol. 91, p. 216, 1854.
5. Curle, N., "*The Mechanics of Edge-Tones*," Proc. Roy. Soc. (London), A216, 412, 1953.
6. Nyborg, W. L., "*Self- Maintained Oscillations of the Jet in the Jet-Edge System*," J. Acoust. Soc. Am., vol 26, p 174, 1954.
7. Powell, A., "*On the Edge Tone*," J. Acoust. Soc. Am., vol 33, p. 395, 1961.
8. Brown, G. B., "*On Vortex Motion in Gaseous Jets and the Origin of Their Sensitivity to Sound*," Proc. Physical Society (London), vol. 47, pp. 703-732, 1935.
9. Karamcheti, K., and Bauer, A., "*Edge-Tone Generation*," SUDAER Report 162, Department of Aeronautics and Astronautics, Stanford University, 1963.
10. Shield, W. L. and Karamcheti, K., "*An Experimental Investigation of the Edge Tone Flow Field*," SUDAAR Report No. 304, Stanford University, Feb. 1967.
11. Stegen, G. R. and Karamcheti, K., "*On the Structure of an Edge Tone Flow Field*," SUDAAR Report No. 303, Stanford University, Feb. 1967.
12. Lighthill, M. J., "*On Sound Generated Aerodynamically*," Proc. R. Soc. London Ser. A 211, 564, 1952 .
13. Holger, D. K., Wilson, T. A. and Beavers, G. S., "*Fluid Mechanics of the Edge Tone*," J. Acoust. Soc. Am., 62, 1116, 1977
14. Holger, D. K., Wilson, T. A. and Beavers, G. S., "*The Amplitude of Edge Tone Sound*," J. Acoust. Soc. Am., 67, 1507, 1980 .
15. Rockwell, D., Knisely, C. and Ziada, S., "*Methods for Simultaneous Visualization of Vortex Impingement and Pressure/Force Measurement*," in Merzkirch, W. (editor), Flow Visualization II, Proc. 2nd International Symp. on Flow Visualization, Bochum, West Germany, pp. 349-353, Sept. 9-12, 1980 .
16. Rockwell, D. and Naudascher, E., "*Self-Sustaining Oscillations of Impinging Free Shear Layers*," Ann. Rev. of Fluid Mech., Vol. 11 , 67-94, 1979 .
17. Rockwell, D. and Knisely, C., "*The Organized Nature of Flow Impingement upon a Corner*," J. Fluid Mech., Vol. 93, No. 3, 413-432, 1979 .
18. Rockwell, D. and Knisely, C., "*Vortex-Edge Interaction: Mechanisms for Generating Low Frequency Components*," Physics of Fluids, Vol. 23, No. 2, 239-240, 1980 .
19. Ohring, S., "*Calculations Pertaining to the Dipole Nature of the Edge Tone*," J. Acoust. Soc. Am. Vol. 83, No. 6, pp. 2074-2085, 1988 .

20. Ohring, S., "*Calculations of Self-Excited Impinging Jet Flow*," J. Fluid Mechanics, Vol.163, 69-98, 1986.
21. Brown, G. B., "*The Mechanism of Edge Tone Production*," Vol. 49-5, pp. 508-521, 1937.
22. Brown, G. B., "*Organ Pipes and Edge Tones*," Nature, Vol. 141, pp. 11-13, 1938.
23. Staubli, T and Rockwell, D., "*Interaction of an Unstable Planar Jet with an Oscillating Leading Edge*," J. Fluid Mech., vol. 176, pp. 135-167, 1987 .
24. Chakravarthy, S. R., Szema, K.-Y., Goldberg, U. C., Gorski, J. J., and Osher, S., "*Application of a New Class of High Accuracy TVD Schemes to the Navier-Stokes Equations*," AIAA Paper No. 85-0165, January 1985.
25. Dougherty, N. S., Holt, J. B., Liu, B. L., and O'Farrell, J. M., "*Time-Accurate Navier-Stokes Computations of Unsteady Flows: the Karman Vortex Street*," AIAA Paper No. 89-0144, presented at the AIAA 27th Aerospace Sciences Meeting, Reno, Nevada, January 9-12, 1989.
26. Dougherty, N. S., Holt, J. B. , Nesman, T. E., and Farr, R. A., "*Time-Accurate Navier-Stokes Computations of Self-Excited Two-Dimensional Unsteady Cavity Flows*," AIAA Paper No. 90-0691, presented at the AIAA 28th Aerospace Sciences Meeting, Reno, Nevada, January 8-11, 1990.
27. Morse, P. M. and Ingard, K. U., Theoretical Acoustics, McGraw-Hill, 1968

REPORT DOCUMENTATION PAGE

Form Approved
OMB No. 0704-0188

Public reporting burden for this collection of information is estimated to average 1 hour per response, including the time for reviewing instructions, searching existing data sources, gathering and maintaining the data needed, and completing and reviewing the collection of information. Send comments regarding this burden estimate or any other aspect of this collection of information, including suggestions for reducing this burden, to Washington Headquarters Services, Directorate for Information Operations and Reports, 1215 Jefferson Davis Highway, Suite 1204, Arlington, VA 22202-4302, and to the Office of Management and Budget, Paperwork Reduction Project (0704-0188), Washington, DC 20503.

| | | | | |
|---|---|--|---|--|
| 1. AGENCY USE ONLY (Leave blank) | | 2. REPORT DATE February 1994 | 3. REPORT TYPE AND DATES COVERED Contractor Report (Final) | |
| 4. TITLE AND SUBTITLE Numerical Simulation of the Edge Tone Phenomenon | | | 5. FUNDING NUMBERS NAS8-38550 | |
| 6. AUTHOR(S) N.S. Dougherty, B.L. Liu, and J.M. O'Farrell | | | | |
| 7. PERFORMING ORGANIZATION NAME(S) AND ADDRESS(ES) Rockwell International Space Systems Division, Huntsville Operations 555 Discovery Drive Huntsville, Alabama 35806 | | | 8. PERFORMING ORGANIZATION REPORT NUMBER M-744 | |
| 9. SPONSORING/MONITORING AGENCY NAME(S) AND ADDRESS(ES) National Aeronautics and Space Administration George C. Marshall Space Flight Center Marshall Space Flight Center, Alabama 35812 | | | 10. SPONSORING/MONITORING AGENCY REPORT NUMBER NASA CR-4581 | |
| 11. SUPPLEMENTARY NOTES Prepared for Structures and Dynamics Laboratory, Science and Engineering Directorate Contract Monitor: Jess H. Jones | | | | |
| 12a. DISTRIBUTION/AVAILABILITY STATEMENT Subject Category: 02 Unclassified-Unlimited | | | 12b. DISTRIBUTION CODE | |
| 13. ABSTRACT (Maximum 200 words) Time Accurate Navier-Stokes computations were performed to study a class II (acoustic) whistle, the edge tone, and to gain knowledge of the vortex-acoustic coupling mechanisms driving production of these tones. Results were obtained by solving the full Navier-Stokes equations for laminar compressible air flow of a two-dimensional jet issuing from a slit interacting with a wedge. Cases considered were determined by varying the distance from the slit to the wedge. Flow speed was kept constant at 1,750 cm/s as was the slit thickness of 0.1 cm, corresponding to conditions in the experiments of Brown (ref. 1). The analytical computations revealed edge tones to be present in four harmonic stages of jet flow instability over the wedge as the jet length was varied from 0.3 to 1.6 cm. Excellent agreement was obtained in all four edge tone stage cases between the present computational results and the experimentally obtained frequencies and flow visualization results of Brown. Specific edge tone generation phenomena and further confirmation of certain theories and empirical formulas concerning these phenomena were brought to light in this analytical simulation of edge tones. | | | | |
| 14. SUBJECT TERMS Vortex Shedding, Edgetones, Free Shear Layer Instability, Unsteady Flow CFD Simulators | | | 15. NUMBER OF PAGES 72 | |
| | | | 16. PRICE CODE A04 | |
| 17. SECURITY CLASSIFICATION OF REPORT Unclassified | 18. SECURITY CLASSIFICATION OF THIS PAGE Unclassified | 19. SECURITY CLASSIFICATION OF ABSTRACT Unclassified | 20. LIMITATION OF ABSTRACT Unlimited | |